



**Effects of stemming and timing on rock fragmentation
and downstream crusher throughput at a selected
quarry in South Africa**

by

Mr Samuel Alpheus Madanda

Student number: 17190754

Submitted in accordance with the requirements for the degree of

Master of Engineering

at the

University of South Africa

Supervisor: Prof Francois Mulenga

November 2024

Declaration

Name: Samuel Alpheus Madanda

Student Number: 17190754


Degree: Master of Engineering in Mining Engineering

Title: Effects of stemming and timing on rock fragmentation and downstream crusher throughput at a selected quarry in South Africa

I declare that the above dissertation is my own work and that all the sources that I have used or quoted have been indicated and acknowledged by means of complete references.

I further declare that I submitted the dissertation to originality checking software and that it falls within the accepted requirements for originality.

I further declare that I have not previously submitted this work, or part of it, for examination at Unisa for another qualification or at any other higher education institution.



Signature

16/01/2025

Date

Abstract

The optimisation of a quarrying operation depends on the effectiveness of rock fragmentation and the resulting throughput of the primary crusher. However, a typical quarry in South Africa is experiencing inconsistent rock fragmentation, with excessive oversize material, known as boulders. As a result, efficiency has decreased due to expensive secondary breaking. This study examines how stemming length and inter-hole delay affect fragmentation and crusher throughput in a granite quarry.

Six controlled blasts were carried out on site for different combination of stemming lengths and inter-hole delays. Blasts #1, #2, and #3 focused on the inter-hole delay timing set at 17, 9, and 6 ms respectively. The remaining blasts #4, #5, and #6 explored the stemming lengths of 2 m, 1.5 m, and 1 m respectively. The resulting fragmentation sizes were analysed using the WipFrag software while crusher performance was measured in terms of throughput. The Kuz-Ram model and the Kuznetsov-Cunningham-Ouchterlony (KCO) model were then used as part of the sense-making exercise. Finally, at the primary crushing plant, the run-of-mine feeds from the six blasts were measured while stoppages and throughput rates were monitored over a period of a month.

The data analysis revealed that the KCO fragmentation model was the best fit for the quarry. Finer fragment sizes and higher crusher throughput were noted for shorter stemming lengths (1 m). On the other hand, fragmentation quality decreased with longer stemming (2 m) producing oversized fragments that impeded throughput. The adequate stemming may therefore be around 1.5 m. With the inter-hole delay timing, larger fragments were produced with shorter (≤ 6 ms) and longer (≥ 9 ms) delays. Optimal delay would therefore be between 6 ms and 9 ms for the granite quarry. Lastly, the crusher throughput improved by 8% (from 277 tph to 300 tph), approaching the required 325 tph with stemming and delay adjustments.

Keywords: Stemming length, inter-hole delay timing, rock fragmentation, crusher throughput, stemming ejection

Dedication

I dedicate this dissertation to my spouse, parents, and siblings in appreciation of their unwavering love, support, and encouragement throughout my academic career. Finally, I would want to thank everyone who helped make this dissertation a success. Your efforts are greatly appreciated.

Acknowledgments

Firstly, I would want to express my sincere appreciation to God Almighty for providing me with the grace, health, strength, knowledge, and understanding I needed to finish my Master's dissertation.

I wish to acknowledge my supervisor Professor Francois Mulenga from the University of South Africa. Your support and advice helped me get through all phases of writing my dissertation. I appreciate your enormous efforts, dedication, and encouragement to my studies.

I wish to extend my deepest gratitude to my wife, Dr Vhutali Carol Madanda, for her unwavering support and countless sacrifices throughout my academic journey. I am equally grateful to my wonderful parents (Mr. Aifheli Alpheus and Mrs. Esther Madanda), as well as my siblings (Mrs. Tshifhiwa Salome Madanda, Mr. Salani Zacharia Madanda, Ms. Dowelani Madanda, Ms Murendeni Madanda, and Mr. Mulalo Madanda), whose love and encouragement have been the cornerstone of my achievements. May the Almighty God bless you all abundantly.

Finally, I would wish to express my appreciation to the quarry management team, including the Quarry Manager, the Blaster, and the Quarry Supervisors. Their practical insights, support, and the opportunity to work directly within the quarry environment were crucial to the success of this research.

Table of Contents

Declaration.....	i
Abstract	ii
Dedication	iii
Acknowledgments.....	iv
Table of Contents	v
List of figures	ix
List of tables.....	xv
List of abbreviations	xvii
List of symbols	xviii
Chapter 1: Introduction	1
1.1. Background	1
1.2. Research problem and purpose of the study	2
1.3. Research objective	3
1.4. Significance of the study	4
1.5. Structure of the dissertation	4
Chapter 2: Literature review.....	6
2.1. Introduction	6
2.2. Controllable factors influencing rock fragmentation	8
2.2.1. Effects of stemming on rock fragmentation	9
2.2.2. Effects of inter-hole delay timing on rock fragmentation.....	13
2.2.3. Environmental impacts of controllable blast variables	17
2.3. Effects of rock fragmentation on downstream operations	21
2.4. Methods for the estimation of rock fragmentation	24
2.4.1. Image analysis of rock fragmentation.....	26

2.4.2. Empirical estimation of rock fragmentation.....	29
2.5. Conclusion.....	39
Chapter 3: Experimental work and data collection	40
3.1. Introduction	40
3.2. Collection of historical blast data	41
3.3. Collection of experimental field data	44
3.3.1. Adherence to the safety procedures on the blasting site.....	46
3.3.2. Assessing the bench and marking drill holes	47
3.3.3. Two-dimensional (2D) face profiling of bench highwalls	49
3.3.4. Blast design setup.....	52
3.3.5. Preparing a primer and priming each blasthole.....	61
3.3.6. Charging of blastholes	62
3.3.7. Stemming of blastholes	65
3.3.8. Connecting and tagging the cables for electronic detonators.....	67
3.3.9. Detonating the charge.....	69
3.3.10. Video recordings	70
3.3.11. Blast vibration monitoring.....	72
3.3.12. Collection of crusher throughput data	74
3.4. Data evaluation.....	77
3.4.1. Rock fragmentation analysis	77
3.4.2. Analysis of the throughput of the crusher.....	79
3.5. Limitations and challenges encountered.....	80
Chapter 4: Effects of stemming length and inter-hole delay on rock fragmentation	82
4.1. Introduction.....	82
4.2. Historical blasting performance.....	83

4.2.1.	Review of historical results.....	83
4.2.2.	Assessment of safety compliance of historical blasts.....	84
4.3.	Field observation and measurement.....	86
4.3.1.	Blast bench face and terrain conditions	86
4.3.2.	Measurements taken during surveys to profile rock faces ...	88
4.4.	Experimental blast results.....	90
4.4.1.	Effects of stemming length on rock fragmentation	92
4.4.2.	Effect of inter-hole delay timing on rock fragmentation	96
4.4.3.	Safety evaluation of the experimental blasts	99
4.5.	Statistical analysis	104
4.5.1.	Relationship between mean fragmentation size and stemming length.....	104
4.5.2.	Relationship between fragmentation size and inter-hole delay timing	106
4.6.	Discussion of the fragmentation results	109
4.6.1.	Contribution of stemming length to rock fragmentation	109
4.6.2.	Contribution of inter-hole delay timing to rock fragmentation	110
4.7.	Empirical modelling of rock fragmentation	111
4.7.1.	Modelling using the Kuz-Ram and KCO models	111
4.7.2.	Performance of the fragmentation models: Kuz-Ram versus KCO.....	119
4.8.	Summarised findings	123
4.9.	Concluding remarks.....	123
Chapter 5: Effects of rock fragmentation on downstream crusher throughput		125
5.1.	Introduction.....	125

5.2. Run-of-mine size distributions to the primary crusher.....	126
5.2.1. Feed size distributions to the primary crusher.....	127
5.2.2. Comparison of muckpile and crusher feed size distributions	129
5.3. Stoppages observed at the primary crusher	132
5.4. Performance of the primary crusher as a function of blasting ...	136
5.5. Effect of rock fragmentation on crusher throughput.....	137
5.6. Significance of the findings	140
5.7. Conclusion.....	141
Chapter 6: Conclusion and recommendations	142
6.1. Introduction.....	142
6.2. Summary of the research findings	142
6.2.1. Relationship between stemming length and rock fragmentation	142
6.2.2. Relationship between inter-hole delay timing and rock fragmentation.....	143
6.2.3. Evaluation of fragmentation models	144
6.2.4. Relationship between rock fragmentation and downstream crusher performance.....	145
6.3. Recommendations for future work	146
List of references	147
Appendices	162

List of figures

Figure 2.1: Factor affecting rock fragmentation (Gebretsadik et al., 2024) ..	7
Figure 2.2. Definition of key blast design parameters classified as controllable factors (Reddy et al., 2020)	9
Figure 2.3. Different types of materials that can be used for stemming: A – Drilling cutting stemming materials; B – Crushed aggregate rock; and C – Clay stemming material (Reddy et al., 2020)	10
Figure 2.4: Relationship between the average fragment size and the inter-hole timing measured from several blasts (Chung and Katsabanis, 2001)	15
Figure 2.5: Criteria for safe level blasting as per the USBM RI 8507 code (Siskind, 1980; Uysal and Cavus, 2013)	19
Figure 2.6: Relationship between blasting costs and downstream operational costs (Kanchibotla, 2003)	21
Figure 2.7: Relationship between operational cost units and blasting costs (after Rosales-Huamani et al., 2020)	22
Figure 2.8: Relationship between rock fragmentation and mining activities (Ozdemir and Kumral, 2019)	24
Figure 2.9: Main prediction and measurement methods of rock fragmentation (after Sudhakar et al., 2005)	25
Figure 2.10: Process flow for the blast image analysis with the WipFrag 4 software (Taiwo et al., 2024)	27
Figure 2.11: Histogram, netting, contouring, and cumulative size curve view of the broken muckpile from the blast block (Singh et al., 2015)	27

Figure 2.12: Size distribution curves estimated with WipFrag and measured from three viewpoints A, B, and C versus the Kuz-Ram model at the FYS granite quarry (Shehu et al., 2022)	33
Figure 3.1: Schematic of experimental design	41
Figure 3.2: Furukawa Drill Rig Model HCR1500 – EDII used on site (Source: Author’s own picture)	46
Figure 3.3: (A) Safety harness worn when working between barrier and crest attached to the safety barricade; and (B) Typical blasting signs (Source: Author’s own picture)	47
Figure 3.4: A typical staked bench ready for drilling at the quarry site (Source: Author’s own picture).....	48
Figure 3.5: (A) Trimble R4s Global Navigation Satellite System; (B) Trimble TSC3 controller; and (C) TSC3 and R4s GNSS mounted on a 2-m antenna (Source: Author’s own picture).....	49
Figure 3.6: Starting a new Job in FaceProfiler	50
Figure 3.7: (A) Samsung device; (B) Reflector flag and (C) Setup used in face profiling surveys (Source: Author’s own picture)	51
Figure 3.8: Illustrating the use of the TruPulse 200 Laser Profiler for bench face profiling	51
Figure 3.9: Starting a new design in I-Blast	52
Figure 3.10: Importing the drill hole patten created from the Trimble TSC3 controller into the I-Blast software.....	53
Figure 3.11: Example of drill hole positions imported into the I-Blast software	54
Figure 3.12: Identification of the drill hole depth	55
Figure 3.13: Design configuration for the front row angle	56

Figure 3.14: (1) – Drill hole design function and (2) – 2D profile dialogue box	57
Figure 3.15: A – Display of the drill hole details and B – Profile of the face of the drilled bench	58
Figure 3.16: Loading of blast hole with explosives.....	59
Figure 3.17: Entering the input data pertaining to the surface delay wiring	59
Figure 3.18: Example of blast holes charged with explosives and their corresponding wired inter-hole delays	60
Figure 3.19: Inter-row delay timing configuration	61
Figure 3.20: Priming of a blast hole – The typical red C-400 booster used in the various blast tests is shown on the top right with the yellow wire holding the AXXIS GII detonator (Source: Author’s own picture)	62
Figure 3.21: An explosive truck with emulsion and blast hole charging (Source: Author’s own picture).....	63
Figure 3.22: Excessive emulsion sucked out of the blastholes using a PVC pipe (Source: Author’s own picture).....	65
Figure 3.23: Weighing of the standard cup of emulsion before and after gassing (Source: Author’s own picture)	66
Figure 3.24: Stemming process – (A) Tamping and stemming; (B) Taking measurements after gassing using a tape measure (Source: Author’s own picture).....	67
Figure 3.25: Procedures followed when attaching detonator cords (Source: Author’s own picture)	68
Figure 3.26: (A) Remote slave box; (B) Blaster verifying the blast connections; and (C) Remote master initiating box (Source: Author’s own picture).....	70

Figure 3.27: Configuration and setting up of the blasting camera (Source: Author's own picture)	71
Figure 3.28: View of the detonation sequence of the production bench (Source: Author's own picture).....	72
Figure 3.29: Location of the two vibrometers used for the blast trials (Source: Picture supplied by the quarry).....	73
Figure 3.30: The two Nomis Mini Supergraph seismographs used on site to monitor ground vibrations and airblast (Source: Author's own picture)....	73
Figure 3.31: Snapshots of the weightometers located in the control room and at the conveyor belt discharge point (Source: Author's own picture)	75
Figure 3.32: Flow diagram of the primary crushing of the aggregate run-of-mine with the closed side setting (CSS) of 127 mm feeding onto the Intermediate Stockpile (ISP)	76
Figure 3.33: Diagram of a jaw crusher with key design and operating parameters – OSS is the open side setting of the crusher while CSS refers to its closed side setting.....	77
Figure 3.34: Procedure followed to analyse fragmentation using the WipFrag software.....	78
Figure 3.35: Image-based monitoring of the truck feed fragmentation at the quarry (Source: Author's own picture)	79
Figure 4.1: Safety limits for ground-born vibrations from historical blasting as established by USBM and OSM.....	85
Figure 4.2: A – Bench terrain for blast #1; B – Bench terrain for blast #3; C – Bench terrain for blast #2; D – Bench terrain for blast #4; and E – Bench terrain for blast #5.....	87
Figure 4.3: Observed features of the bench face for blast #2 with key geological characteristics.....	88

Figure 4.4: Drilling pattern with hole depths and angles for blast #2.....	89
Figure 4.5: Surveyed face profiling showing excessive burden on holes 68, 69, 57 and 71 for blast #2	90
Figure 4.6: Muckpile produced from blast #4 with a safety hardhat used as a 290 mm wide reference point.....	92
Figure 4.7: Fragmentation analysis report for blast #4 generated with the WipFrag software.....	93
Figure 4.8: Particle size distributions plotted for blasts #4, #5 and #6	95
Figure 4.9: Design for blast #3 incorporating an inter-hole delay timing of 6 ms and an inter-row delay timing of 23 ms	97
Figure 4.10: Particle size distributions plotted for blasts #1, #2, and #3 ..	99
Figure 4.11: A – Detonation with a minimal stemming ejection for blast #1; B – Blast #4 with four blast hole stemming ejection; C – Stemming ejection in blast #5; and D – Stemming ejection in blast #6	100
Figure 4.12: Map of the peak particle velocities and frequencies for the ground vibrations generated during all the blasts to verify compliance with USBM standards.....	102
Figure 4.13: Airblast levels below the safety threshold as measured for the six blast trials at the quarry viewpoint and the primary crusher.....	104
Figure 4.14: Relationship between mean fragmentation size and stemming length	105
Figure 4.15: Relationship between mean fragmentation size and inter-hole delay timing with error bars representing the 95% confidence interval ..	107
Figure 4.16: Muckpile size distribution predicted for blast #1	112
Figure 4.17: Estimated muckpile size distribution for blast #2	113
Figure 4.18: Muckpile size distribution predicted for blast #3.....	114
Figure 4.19: Muckpile size distribution predicted for blast # 4.....	116

Figure 4.20: Muckpile size distribution predicted for blast #5.....	117
Figure 4.21: Muckpile size distribution predicted for blast #6.....	118
Figure 4.22: Overall correlation between the KCO and Kuz-Ram models	122
Figure 5.1: Fragmentation analysis report of the crusher feed from blast #1	127
Figure 5.2: Size characteristics of the crusher feeds from the six blasts	129
Figure 5.3: Comparison between the size distributions at the crusher feed and the muckpile for blast #1	130
Figure 5.4: Comparison between the size distributions at the crusher feed and the muckpile for blast #2	131
Figure 5.5: Comprehensive analysis of stoppages at the primary crusher fed with the muckpile produced from blast #1	134
Figure 5.6: Detailed examination of stoppages at the primary crusher fed with the muckpile produced from blast #2.....	135
Figure 5.7: Performance of the primary crushing plant across the six blasts	136
Figure 5.8: Relationship between ROM feed size and crusher throughput	137

List of tables

Table 2.1: Rock factor parameters and ratings (after Gheibie et al., 2010)	31
Table 3.1: Summarised information extracted from blast reports between 2022 and 2023	43
Table 3.2: An overview of blast design parameters for blasts #1 and #4	45
Table 3.3: Sheet used during the emulsion pumping of some of the blast holes prepared for blast #1	64
Table 3.4: Overview of the structure of the blast vibration monitoring data (peak particle velocity and frequency ranges) collected	74
Table 4.1: Overview of historical blast reports showing various parameters	83
Table 4.2: Historical seismographic results taken from the quarry viewpoint and the primary crusher	84
Table 4.3: Summary of blast design parameters for the experimental study	91
Table 4.4: Characteristics of the muckpile size distributions corresponding to blasts #4, #5, and #6	94
Table 4.5: Cumulative particle size distributions for blasts #4, #5 and #6	94
Table 4.6: Characteristics of the muckpile size distributions corresponding to blasts #1, #2, and #3	97
Table 4.7: Statistics relating the measurement of the mean fragmentation size at 95% confidence	108
Table 4.8: Predicted fragmentation for blast #1	111
Table 4.9: Predicted fragmentation for blast #2	112

Table 4.10: Predicted fragmentation for blast #3	114
Table 4.11: Summary of the predicted mean sizes for blasts #1, #2, and #3	115
Table 4.12: Predicted fragmentation for blast #4	115
Table 4.13: Predicted fragmentation for blast #5	116
Table 4.14: Predicted fragmentation for blast #6	117
Table 4.15: Summary of mean sizes expected from blasts #4, #5, and #6	118
Table 4.16: Calculated error values for model prediction for all experimental blasts	121
Table 5.1: Summary of the cumulative mass fractions of the six ROM feeds	128
Table 5.2: Summary of particle size distributions at the quarry muckpile and crusher feed for blast #1	130
Table 5.3: Summary of particle size distributions at the quarry muckpile and crusher feed for blast #2	131
Table 5.4: Performance results of the primary crusher plant recorded for each blast over a month worth of production	133
Table 5.5: Statistics associated with the regression analysis of the fragmentation-throughput correlation.....	139

List of abbreviations

Abbreviation	Description
ADT	Articulated Dump Truck
CSS	Closed Side Setting
EDs	Electronic detonators
EDP	Edge Detection Parameters
GNSS	Global Navigation Satellite System
GPS	Global Positioning System
ISP	Intermediate Stockpile
KCO	Kuznetsov-Cunningham-Ouchterlony
MEA	Mean Absolute Error
MHSA	Mine Health and Safety Act
MSE	Mean Square Error
PPE	Personal Protective Equipment
PSD	Particle Size Distribution
R^2	Pearson coefficient of determination
RMSE	Root Mean Squared Error
ROM	Run-of-mine
RWS	Relative weight strength
USBM	United States Bureau of Mines
VOD	Velocity of detonation

List of symbols

Symbol	Description	Unit
A	Mass factor	Dimensionless
B	Burden	m
b	Curve undulation parameter	m
d	Blast-hole diameter	m
D10	10-percentile	mm
D50	50 percentile size	mm
D80	80-percentile	mm
D90	90-percentile	mm
E	Young's modulus	GPa
E_{PI}	Explosive performance index	Dimensionless
E_R	Explosive charge	Dimensionless
H	Bench height	m
HF	Hardness factor	Dimensionless
JA	Joint Plane Angle	Dimensionless
JF	Joint Factor	Dimensionless
JS	Vertical Joint Spacing	Dimensionless
K	Stiffness of the rock mass	Dimensionless
K_P	Powder factor or specific charge	kg/m ³
L	Total length of drilled hole	m
L_b	Length of the bottom charge	m

L_c	Length of column charge	m
n	Uniformity exponent of the distribution	Dimensionless
PPV	Peak Particle Velocity	mm/s
Q	Mass of explosive per blast hole	kg
RD	Rock Density	t/m ³
RDI	Rock Density Influence	t/m ³
R_{EE}	Relative effective energy of the explosive	MJ/kg
RMD	Rock mass description	Dimensionless
R_p	Percentage of material that passes through a screen	%
S	Spacing	m
S_{ANFO}	Weight strength of explosive relative to ANFO	%
SD	Standard deviation of drilling accuracy	m
T	Stemming length	m
T_{min}	Minimum response time	ms
UCS	Uniaxial Compressive Strength	MPa
W	Standard deviation of drilling accuracy	m
X	Specific screen size	cm
x_c	Rosin-Rammler size	mm
X_{max}	Maximum allowable fragment size in a distribution	m
X_{50}	Mean size	mm
Y	Young's modulus	GPa
\varnothing_h	Drill-hole diameter	m
σ_c	Compressive strength	MPa

Chapter 1: Introduction

1.1. Background

Most of the quarries employ drilling and blasting as the principal method for rock breaking. This method is adopted primarily because it is recognised as the most cost-effective method of breaking rock in-situ (Silva et al., 2018). The effectiveness of this method considerably impacts downstream operations such as loading, hauling and crushing. It is therefore critical that blast design is optimised not only for rock fragmentation but also for downstream processes.

Rock fragmentation can be regarded as a quantitative evaluation describing the size distribution of a muckpile after blasting (Cho and Kaneko, 2004). Optimal fragmentation alludes to the achievement of a uniform rock size distribution in the blast. It is acknowledged that achieving an optimal fragment size mitigates the energy required to subsequently crush the material. This means that optimal fragmentation leads to increased throughput downstream.

Several investigations have been conducted on the improvement of blast fragmentation (Singh et al., 1991; Jhanwar et al., 2000; Amiel, 2008). They concur that there are several variables that affect a blast quality that should be considered. These factors can be divided into controllable and uncontrollable parameters (Hudaverdi et al., 2012). Controllable parameters can be regulated and modified on site. On the other hand, uncontrollable parameters are inherent to the properties of the in-situ rock, the nature of the rock mass, and geological discontinuities within the rock mass (Phamotse and Nhleko, 2019).

This research study mainly focuses on two controllable parameters: the stemming and the timing of a blast. As a controllable parameter, stemming should be carefully chosen because of its great effect on the cost of blasting and on the resulting fragment size (Reddy et al., 2020). In contrast, timing

is one good blast design parameter commonly used to optimise blast fragmentation and muckpile profile (Katsabanis et al., 2006). Experimental fieldwork was therefore conducted on the effects of stemming and delay timing on rock fragmentation and downstream crusher throughput. Other controllable blasting factors were kept unchanged for all experimental tests considered. In addition to this, historical blast designs from the mine were analysed to fully assess the combined effect of stemming and timing.

1.2. Research problem and purpose of the study

The overall economics of opencast mining operations is directly affected by blasting (Singh et al., 2015). This is because rock fragmentation size distribution has a strong influence on downstream operations including loading, hauling, and crushing. In essence, better fragmentation leads to reduced energy and costs expended downstream.

A quarry in South Africa is experiencing inconsistent rock fragmentation, with approximately 40% of blasts producing excessive oversize material, resulting in significant boulders. For this reason, the quarry has been resorting to secondary breaking to deal with boulders. Secondary breaking refers to the reduction of boulders down to an acceptable size as per site-specific requirements by means of a hydraulic hammer or by secondary blasting (Adeyemi et al., 2019). Secondary blasting is generally considered when huge boulders in the muckpile cannot be fragmented by a hydraulic hammer. In any case, the quarry incurs additional operational costs to support secondary breakage. Adeyemi et al. (2019) suggested that secondary breakage is possibly the largest additional cost incurred as a result of poor fragmentation. Kazem and Bahareh (2006) further suggested that introducing secondary blasting increases the total operational costs by 30% to 50%. To this end, the quarry aims to reduce secondary blasting costs by optimising rock fragmentation. Stemming and timing are adjusted for the purpose while their impact is ascertained for improved downstream throughput at the crushing stage.

1.3. Research objective

Stemming length and delay timing are crucial factors for effective rock blasting and fragmentation. These two parameters significantly influence the outcomes of rock fragmentation depending on the specific conditions of the site and the blast design (Amiel, 2008).

Improved rock fragmentation for efficient downstream processes is something that mines and quarries aspired to. As such, understanding the connection between blast design parameters, rock fragmentation, and crusher throughput is an ideal worth pursuing. The current study attempts to contribute to the endeavour by investigating the effects of stemming length and delay timing on rock fragmentation in a South African quarry. By varying these two blast design parameters, a better understanding of the underlying correlations is expected to ensue while providing valuable insights into the quarry-to-crusher production chain.

It has also been argued that the precise control of stemming and timing is not always feasible (Silva et al., 2018 & 2019; Mpofu et al., 2021). However, the present study aims to demonstrate the potential benefits of such optimisation in enhancing the overall blasting and crushing performance.

In line with the above, the following research objectives are set for the study to:

- investigate the effects of stemming and delay timing on rock fragmentation;
- determine ground vibration and air-blast at the selected quarry;
- determine how rock fragmentation affects the downstream crushing process; and
- identify a suitable empirical rock fragmentation model that captures the effects of stemming and delay for application in the selected quarry.

1.4. Significance of the study

Understanding the effects of stemming and timing on rock fragmentation can help optimize blasting practices. By determining the most effective combination of these variables, mining operations can improve their overall blast performance (Cevizci and Ozkahraman, 2012; Shi et al., 2023). This improved fragmentation, in turn, enhances crusher efficiency, reduces energy consumption, decreases wear on the equipment, and leads to cost savings and increased productivity (Singh et al., 2015; Beyglou et al., 2017). This research study has therefore the potential to promote more cost-effective operations.

Next, better fragmentation reduces the need for secondary blasting and cuts down on the resources required for rock handling and run-of-mine processing (Adeyemi et al., 2019). Furthermore, improved fragmentation benefits the environment by reducing ground vibration, airblast, and flyrock (Bleakney III, 1984; Taji et al., 2012). Optimal blast design and the associated fragmentation also improve crusher throughput and lowers energy consumption in line with more sustainable mining practices.

Lastly, this study aims to enhance blast design and rock fragmentation by offering a better understanding of the variables affecting rock breakage and the resulting outcome of the blast itself.

1.5. Structure of the dissertation

This dissertation is structured in six chapters. Chapter one introduces the dissertation. It also highlights the significance of the study and the anticipated contribution to the existing knowledge for the benefit of the mining industry.

Chapter two presents a detailed review of past literature relating to rock fragmentation, stemming, and delay timing associated with blast operations. Relevant theories around key empirical rock fragmentation models are also

reviewed. The chapter finally identifies gaps in knowledge around the effects of stemming and timing on rock fragmentation.

Chapter three describes the research methodology followed as part of the experimental work conducted on site. It also details the experimental setup and the research design used to support the test work. Furthermore, the chapter presents the instruments and techniques employed in collecting and analysing the data.

Chapter four presents the tools used to analyse the data collected from the experimental work done in Chapter 3. A qualitative assessment is made on how varying stemming lengths and delay timings influence rock fragmentation. The chapter also appraises the usability of two classical fragmentation models in describing the experimental results: the Kuz-Ram model and the Kuznetsov-Cunningham-Ouchterlony model.

In Chapter five, the findings from Chapter 4 are analysed and discussed within the framework of existing scholarly work. The chapter specifically explores the implications of the research findings on blasting practices in the context of rock fragmentation. Attention is also paid towards highlighting the benefits of improved blasting on the performance of crushing as the next step of the value chain.

The final chapter (Chapter 6) summarizes the main findings in terms of the benefits of optimised stemming and delay timing along the mine value chain. It offers recommendations for future research and practical applications in the field of mining and quarrying. The chapter also addresses the potential limitations of the study and suggests areas for further scientific research.

Chapter 2: Literature review

This chapter is a review of publications on the relationship between rock fragmentation and downstream crusher throughput. It starts off by focusing on factors that influence rock fragmentation and specifically explores two controllable blast design variables; namely, stemming length and inter-hole delay timing. Additionally, the chapter investigates how these two variables contribute to blast safety. This is to enhance our understanding of what to monitor when adjusting stemming and timing in order to maintain safety in a mining operation. Finally, the chapter reviews the application of two prominent fragmentation models: the Kuz-Ram model and the Kuznetsov-Cunningham-Ouchterlony (KCO) model. This is to ascertain their respective scope of work and limitations as far as describing rock fragmentation goes.

2.1. Introduction

The concept of rock fragmentation is one of the foundational principles widely studied in mining, quarrying and construction. Rock fragmentation refers to the process of breaking large rocks into smaller fragments to facilitate handling and processing (Cho and Kaneko, 2015). Therefore, achieving good fragmentation enhances the efficiency of downstream operations such as loading, hauling, and crushing (Singh et al., 2015; Gomes-Sebastiao and de Graaf, 2017; Reddy et al., 2020; Roy et al., 2016).

Blasting is the primary stage of breaking the in-situ rock in most quarries around the world and specifically in South Africa. Blasting with chemical energy, also referred to as explosive blasting, is widely considered as more efficient and cheaper compared to mechanical rock breaking (Singh, 2012; Esen, 2017; Silva et al., 2019; Wang et al., 2023).

Several research studies have explored various factors that influence the quality of rock fragmentation. Gebretsadik et al. (2024) classified these factors as controllable and uncontrollable. Figure 2.1 provides a graphical

summary of these two categories of factors where controllable factors are further subdivided into design parameters and explosive properties.

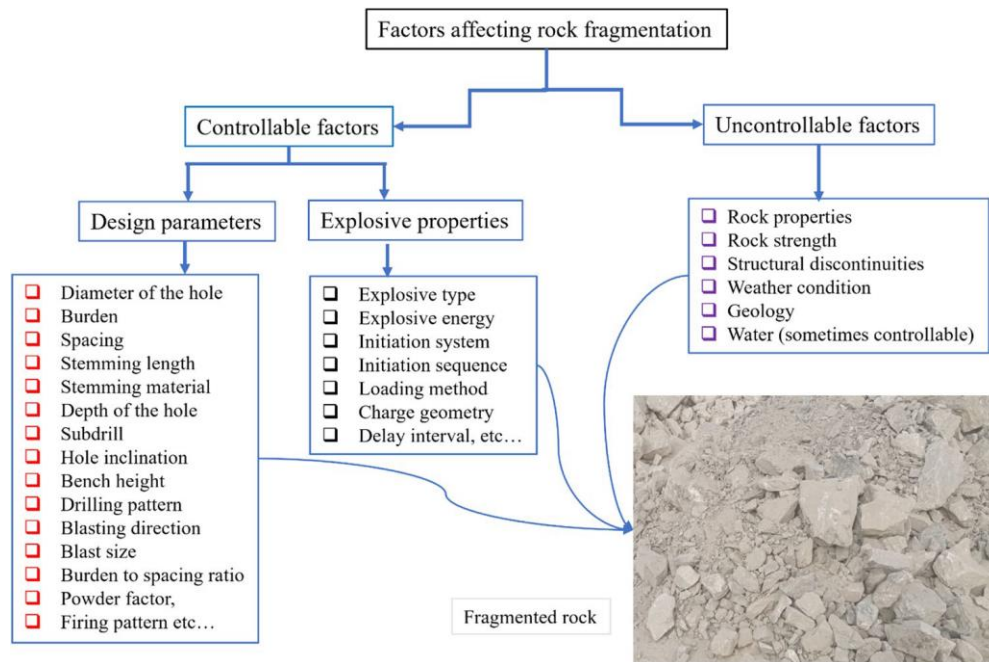


Figure 2.1: Factor affecting rock fragmentation (Gebretsadik et al., 2024)

In terms of research enquiry, it can be argued that controllable factors have been extensively explored. For example, Singh et al. (2015), Reddy et al. (2020), and Oates and Spiteri (2021) specifically looked at stemming as a design parameter. They all observed that stemming material and length significantly influence rock fragmentation. Note that stemming refers to the inert material placed at the top of the explosive charge in a blast hole to contain the energy generated during detonation (Tobin, 2013). According to Reddy et al. (2020), stemming material plays a critical role in ensuring the efficient utilisation of blasting energy and in improving rock fragmentation.

Other researchers such as Singh et al. (2015) and Otterness et al. (1991) focused their effort on inter-hole delay timing. They investigated the impacts of the timing of detonation on the efficiency of the blast. Their studies demonstrated that optimal delay timing can produce more uniform fragment sizes. Stagg (1987) earlier suggested that the optimal timing for fragmentation occurs within a window period. And outside this window, he observed oversized materials. Similar findings were reported by Otterness

et al. (1991), Chung and Katsabanis (2001), and Singh et al. (2015). The selected studies highlight the importance of precise timing in rock blasting.

Proper management of design parameters not only improves fragmentation efficiency but also ensures safety during blasting operations. Close monitoring of ground vibration and airblast is also essential, as these factors are sensitive to changes in blast design. Nguyen et al. (2019) stated that blasting leads to serious environmental impacts such as ground vibration and airblast. They further explained that of the two phenomena, ground vibration is considered as the most dangerous. And in another study conducted by Wang et al. (2020), it was highlighted that the hole-by-hole delay time of a blast have great influence on ground vibration. This is indicative of the fact that optimising delay interval is critical for increased efficiency and productivity of blasting operations. When delay intervals are properly established, rock fragmentation can be improved while ground vibration can be substantially reduced. It is therefore clear that stemming and timing are critical in the optimisation of rock fragmentation, considering both safety and efficiency. The subsequent sections present a detailed review of how the design of stemming and delay timing can help mining operations achieve the desired fragmentation. The review also considers the impact rock fragmentation on the downstream crushing process.

2.2. Controllable factors influencing rock fragmentation

Rock fragmentation is a crucial aspect of mining and quarrying operations that has a great bearing on both their efficiency and safety. Effective rock fragmentation can significantly contain operational costs and improve productivity in the mining value chain (Roy et al., 2016). Controllable factors summarised in Figure 2.1 can be used to contribute to better fragmentation while Figure 2.2 provides a graphical definition of key blast design parameters. These include burden, spacing, and stemming amongst others. Additionally, the size and pattern of drill holes, the type and quantity of explosives, and the timing of the detonations are important contributors to

fragmentation (Oates and Spiteri, 2021; Cunningham, 2005). Numerous studies have also investigated the effects of uncontrollable factors on rock fragmentation. For instance, La Rosa et al. (2015) and Gebretsadik et al. (2024) looked at rock mass and blastability characteristics. Their findings indicated that the generation of fine fragments is dependent on the type of explosives used and the rock strength. Therefore, understanding the effects of geological conditions (i.e., rock type, density, and pre-existing fractures) can lead to better blast design and execution.

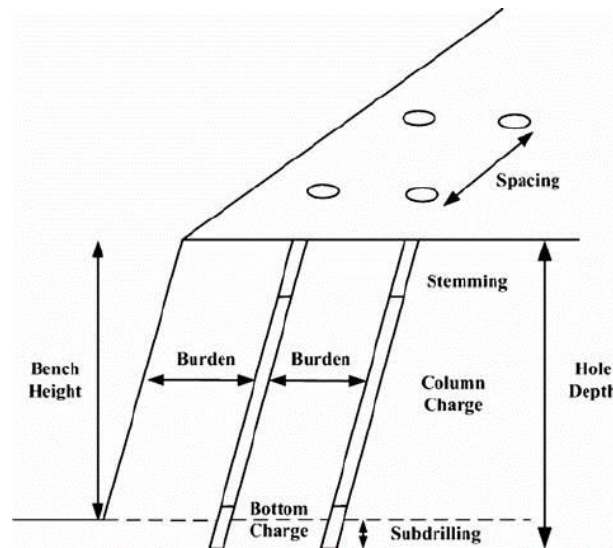


Figure 2.2. Definition of key blast design parameters classified as controllable factors (Reddy et al., 2020)

In terms of the review, the impact of controllable factors on rock fragmentation is examined in detail. The discussion specifically focuses on the effects of stemming and timing on rock fragmentation.

2.2.1. Effects of stemming on rock fragmentation

Stemming is the process of filling a charged blast hole with inert material (Sazid, 2014). Stemming material is generally injected or poured inside the blast hole. The purpose of stemming is to hold gases long enough so as to effectively break the rock. Insufficient stemming can result in the premature escape of explosive gases into the atmosphere known as venting thereby producing oversize fragments or boulders (Sharma and Rai, 2015).

Furthermore, poor stemming can lead to a high rate of air blast and dangerous fly rock (Rajpot, 2009; Oates and Spiteri, 2021). On the other hand, optimal stemming length results in good fragmentation, low degree of air blast, and low level of ground vibrations (Shi et al., 2023).

Stemming generally refers to the material used for stemming as well as the length of material charged for stemming. Both the material and length of stemming are critical to blast design. The choice of stemming material affects how well the explosive gases are confined while stemming length determines the duration for which these gases are held within. Both factors are vital to the efficiency of the blast as they ensure the optimal utilisation of the explosive energy for rock fragmentation (Oates and Spiteri, 2021).

Reddy et al. (2020) investigated the effects of stemming material in a stone quarry situated in Malkapur village, India. In their case study, three stemming materials were tested: drilling cutting, crushed aggregates, and clay (see Figure 2.3). Crushed aggregate rock is a commonly used stemming material because it is readily accessible to most quarries. It is also found to be effective as it forms a plug in the hole that then confines well the gas pressure within the hole. However, Reddy et al. (2020) found clay to be the most effective stemming material (Figure 2.3C). Clay particles are smaller in size compared to drill cuttings and crushed aggregates. As such, clay confines explosive gases better, acts like a tighter plug, and leads to more efficient blasts. The second-best stemming material was found to be the drilling cuttings shown Figure 2.3A.



Figure 2.3. Different types of materials that can be used for stemming: A – Drilling cutting stemming materials; B – Crushed aggregate rock; and C – Clay stemming material (Reddy et al., 2020)

In a recent study, Shi et al. (2023) compared a mixture of water and clay stemming with sand and clay stemming. Like with Reddy et al. (2020), their findings indicated that clay stemming is more effective in directing explosive energy to act on the blast thereby resulting in better fragmentation. In a different study, Zhang et al. (2021) conducted a series of laboratory tests on the effects of sand stemming and partial steel stemming on blasting under a constant specific charge. The specific charge refers here to the mass of explosives used per unit volume of rock to be blasted (Salehi et al., 2024). This stayed constant to ensure uniformity in energy distribution throughout the trials. With this configuration, the researchers were able to precisely compare partial steel stemming and sand stemming. They then highlighted the fact that sand stemming yielded better fragmentation compared to partial steel stemming. The reason why the performance of sand stemming was superior to that of partial steel stemming is that its granular structure made the blast hole seal tighter thereby containing better the explosive gases. Better confinement also allowed sufficient energy to be transferred effectively to the rock, contributing to a better fragmentation. On the other hand, partial steel stemming sealed less tightly than sand. More gas could therefore escape from the hole because of their looser seal. In the end, less explosive energy was transferred to the rock.

The effectiveness of stemming not only depends on the choice of material but also on the stemming length used in blasting operations. However, when it comes to the selection of stemming material, this is guided by the availability and cost of the intended material. Furthermore, according to Sharma and Rai (2015), the stemming length is the column of a blast hole filled with stemming material. Stemming length is important to blast design and its strategic application has been experimentally found to increase energy usage (Shi et al., 2023). When properly applied, stemming retains more of the blast energy and shock waves inside the blast hole for a longer time. Oates and Spiteri (2021) showed that stemming length directly affects blast effectiveness, flyrock, and ground vibration. The two researchers also argued that there exists no generic way of determining the appropriate

stemming length for optimum fragmentation. However, there are guidelines available for its estimation.

Different researchers have linked stemming length to factors such as burden, blast hole diameter, rock strength, and detonation velocity. Sazid et al. (2014) for example suggested that the appropriate stemming length should be determined as a function of the burden. Konya and Davis (1978), on the other hand, recommended a stemming-to-burden ratio ranging from half to one. This contrasts with Rustan (1998) who narrowed the range of stemming-to-burden ratio down to between 0.5 and 0.85. In addition, the length of stemming can also be determined as a function of blast hole diameter rather than just burden. This has been expressed in the most widely used empirical formulations for the stemming length below (Sazid et al., 2014; Mpofu et al., 2021):

$$T = 20 D \quad (2.1)$$

$$T = 0.7 B \text{ to } 1.2 B \quad (2.2)$$

Where T stands for stemming length (m)

D represents blast-hole diameter (m)

B signifies the blast design burden (m).

A useful recommendation by Mpofu et al. (2021) is that the ideal stemming length should fall within the range given by Equation (2.2). By attempting to ensure effective energy confinement during blasting, this guideline seeks to improve fragmentation and manage blast results. Mpofu et al. (2021) also stressed that a stemming length less than the value obtained from Equation (2.1) raises the probability of unfavourable results because the insufficient stemming is unable to adequately contain the explosive energy. However, it is essential to note that the specific risks associated with inadequate stemming, such as airblast, flyrock, and overbreak, were reported by AEL (2014) and not by Mpofu et al. (2021). Indeed, AEL (2014) highlighted that these hazards result from insufficient confinement of the explosive force,

which underscores the importance of adhering to recommended stemming practices.

In order to sum up, regardless of the starting formula used in the estimation of the stemming length, longer stemming produce coarser fragments while shorter stemming leads to high noise, airblast, and venting amongst others (Cevizci and Ozkahraman, 2012). These opposing outcomes therefore highlighted the need for optimal stemming. Numerous studies present comprehensive ways of identifying the optimal stemming practices, including those by Cevizci (2013) and Octova et al. (2022).

2.2.2. Effects of inter-hole delay timing on rock fragmentation

In surface mining, timing can be defined as a process of controlling delay between detonations of individual charges in a blast sequence (Tang et al., 2023). This inter-hole delay is measured in milliseconds (ms) and precisely designed to maximise rock displacement and breakage (Liu and Katsabanis, 1997, Saadatmand Hashemi and Katsabanis, 2020). Studies conducted years back suggest that too short time in hard rock mining may not be effective (Cho and Kaneko, 2004; Katsabanis et al., 2006). The reason for this is that too short a delay can contribute to overlapping stress waves from nearby blast holes. This overlap lowers the blast efficiency by limiting the amount of time needed for cracks to spread through the rock. When there is insufficient delay, the stress waves clash, preventing complete fracture formation and resulting in bigger and less manageable rock fragments (Zhou et al., 2024). Similarly, longer delays in operation can also hinder the propagation of fractures from the initial charge before the subsequent charge detonates leading to poor fragmentation.

Stagg (1987) investigated the influence of blast delay time on rock fragmentation with the intention of optimising blasting practice. The experiment was carried out at a location in Rolla, United States of America (USA), with a geological setting characterised by a great occurrence of dolomite. Eighteen single-row blasts were carried out using a combination

of burdens of 15 inches (0.381 m) and spacings of 21 and 30 inches (0.5334 and 0.762 m) while the range of the delay intervals was between 3 and 55 milliseconds per metre (ms/m) of burden. The finest fragmentation was noted to occur between 3 ms/m and 55 ms/m of burden. Additionally, coarse fragmentation was recorded both at the short delays (<3 ms/m) and long delays (>55 ms/m) tested. It is believed that this happened because explosive charges acted independently at these extreme delay values.

Otterness et al. (1991) carried out another study at the United States Bureau of Mines (USBM). The experimental mine set at the University of Missouri-Rolla was used to thoroughly test the connection between blast design parameters and the results of rock fragmentation. A total of 29 scaled-down blasts were considered with bench sizes between 40 and 80 inches (i.e., 1.016 and 2.032 m). Each blast had 3 to 4 blastholes fired with delay intervals ranging from 3.3 to 13 ms/m of burden. The results showed that fragmentation could be improved by 12 – 20% over single-hole shots or simultaneous firing which agrees with the work by Stagg (1987).

In the same vein, Chung and Katsabanis (2001) showed that average fragment size and delay time are related. To determine this relationship, several small-scale experiments that simulate multi-hole blasts were conducted. The trial blasts were performed in a granodiorite block cut from stone prepared by dimensional stone quarry operations. This enabled the two researchers to ascertain the manner in which the timing of detonations affects rock fragmentation. Based on their experimental results, Chung and Katsabanis (2001) were able to show the marked relationship between average fragment size and timing illustrated in Figure 2.4. It is evident that as time increases, both predicted and measured fragment sizes decrease, with larger fragment sizes being seen at shorter times.

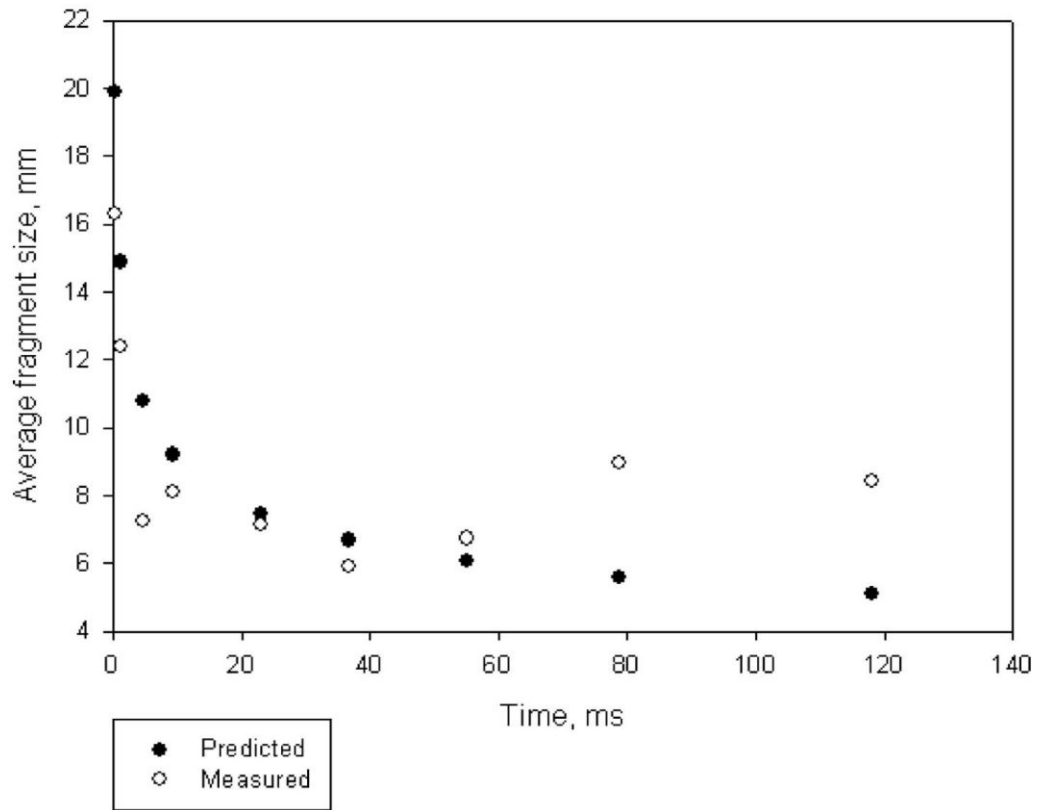


Figure 2.4: Relationship between the average fragment size and the inter-hole timing measured from several blasts (Chung and Katsabanis, 2001)

The design and estimation of delay timing is site-specific and is dependent on a variety of distinct factors like rock type, geological conditions, and blast geometry (e.g., burden and spacing). Onederra and Esen (2003) used a trial of 19 blasts to examine the relationship between measured minimum response (T_{min}) values and different parameters. The distance between the drilled hole and the rock face, or burden, was the first of these parameters to be investigated. The distance between adjacent holes in the blast pattern known as spacing and the size of the holes drilled for explosives or blasthole diameter were also investigated. Onederra and Esen (2003) suggested that delay timing should be designed such that it relates to burden. For example, they recommended a delay timing of 5 – 7 ms/m of burden for blasts with holes of diameter 38 to 311 mm. The following model was developed based on this study to describe the minimum response time (Onederra, 2007):

$$T_{min} = E_R \left[2.0408 \left(\frac{B}{d_{ER}} \right)^{1.465} \right] \quad (2.3)$$

Where T_{min} is the time interval between the detonation of an explosive and the subsequent movement of the rock mass (ms)

B denotes the burden (m)

d refers to blasthole diameter (m)

E_R is a critical parameter used in blasting operations to assess the interaction between the explosive charge and the surrounding rock mass.

The explosive rock mass interaction index E_R in Equation (2.4) is defined as follows (Onederra, 2007):

$$E_R = K E_{PI} \quad (2.4)$$

Where K is a dimensionless metric used to categorize the stiffness of the rock mass in relation to its capacity to absorb energy during blasting operations.

E_{PI} is a unitless indicator known as the explosive performance index. It is a crucial measure of how well an explosive charge works in relation to the rock mass it interacts with.

It can be seen from the literature review done so far that timing has an effect to fragmentation (Preece and Thorne, 1996; Chung and Katsabanis, 2001; Yi et al., 2013; Gkikizas-Lampropoulos, 2016; Tang et al., 2023). It is therefore essential to consider this parameter when optimising blast fragmentation. Furthermore, it is clear from the literature that the timing of a blast should neither be too longer nor too short (Saadatmand Hashemi and Katsabanis, 2020; Liu et al., 2024). As such, it is vital for each mining operation to find the optimal range of timing suitable for their site.

Another important aspect of blasting is to understand the wider effects of various parameters on the environment. By examining the relevant controllable variables, one can learn more about how each affects the overall effectiveness and safety of a blast. The next section discusses the environmental impacts of controllable variables.

2.2.3. Environmental impacts of controllable blast variables

Poor fragmentation is a common issue to be avoided in blasting operations; however, it is not the only concern. Other issues include ground vibration, airblast and flyrock (Kuzu and Ergin, 2005; Hasanipanah et al., 2016; Mohamad et al., 2016; Marto et al., 2014). That is why monitoring is conducted in various mines as a control for the negative impact of blast-induced ground vibrations on surrounding structures and humans (Bleakney III, 1984). Ground vibration monitoring involves measuring and recording ground movements using seismography. As vibrations originate from the blast centre, seismic waves propagate and cause soil and rock particles to move at a certain speed. This oscillating movement is known as particle velocity. Vibration monitoring stations measure the Peak Particle Velocity (PPV), which represents the highest speed at which particles oscillate around an equilibrium point due to seismic waves (Sayed-Ahmed and Naji, 2013). By assessing PPV, blasters can predict the potential risk of damage to nearby structures. Furthermore, monitoring stations track the airblast generated by the blast. Indeed, airblast, also referred to as air overpressure, has the potential to disturb both humans and wildlife, thus contributing to noise pollution (Bleakney III, 1984).

Regulatory limits have been imposed by several legal authorities on blast-induced ground vibrations and airblast to safeguard the environment. These regulations are designed to minimize the adverse effects of blasting activities on nearby buildings, local communities, and wildlife habitats. The International Standards ISO 4866-1990 lay out relevant regulations for controlling the impacts of ground vibrations on different types of buildings (Sayed-Ahmed and Naji, 2013). This is because several studies (e.g., Duvall and Fogelson, 1962; Wiss, 1968; Bleakney III, 1984; AEL, 2014) have consistently argued that structural damage is closely linked to the PPV of ground vibrations.

The USBM was amongst the first to conduct extensive studies on blast-induced ground vibrations. The decade-long research ended with the establishment of the widely accepted safety criterion for vibration limits

(Strebig and Reese, 1975, Siskind, 1980). This criterion was designed to prevent structural and threshold damage to buildings from blasting-induced ground vibrations (Siskind et al., 1980; Bleakney III, 1984). The PPV is the primary criterion for vibration limits. To prevent structural damage, regulatory bodies frequently establish certain PPV thresholds that must not be exceeded. In addition to PPV, vibration frequency is another crucial factor. The way that different structures react to different frequencies varies. Both the velocity and frequency of ground vibrations must be properly monitored and managed. Uysal and Cavus (2013), for example, reported that a decrease in frequency may have negative effects while a decrease in PPV is beneficial.

The USBM generated the graph for the description of the correlation between particle velocity and frequency of ground vibrations shown in Figure 2.5 (Siskind, 1980). This curve is a tool frequently used in the mining industry to evaluate the possible harm that blast-induced ground vibrations could have on buildings and people's health. The line chart aids in defining safe and unsafe domains of the plot area based on the regulatory PPV limits that have been set. Note from Figure 2.5 that areas above the recommended PPV limits are classified as unsafe as they can potentially cause structural damage to existing buildings in the vicinity of the blast centre. On the other hand, areas that fall below the limits are deemed safe. There are also multiple lines on Figure 2.5 that correspond to different critical parameters of ground vibrations associated with blasting. The solid black line refers to the safe vibration limits for industrial facilities at 50.8 mm/s and for drywalls at 19 mm/s. In contrast, the dashed lines indicated that the fact that plaster may sustain damage from vibrations if the particle velocity exceeds 12.7 mm/s. This threshold is in place to guard against possible vibration-related damage to residences and comparable structures.

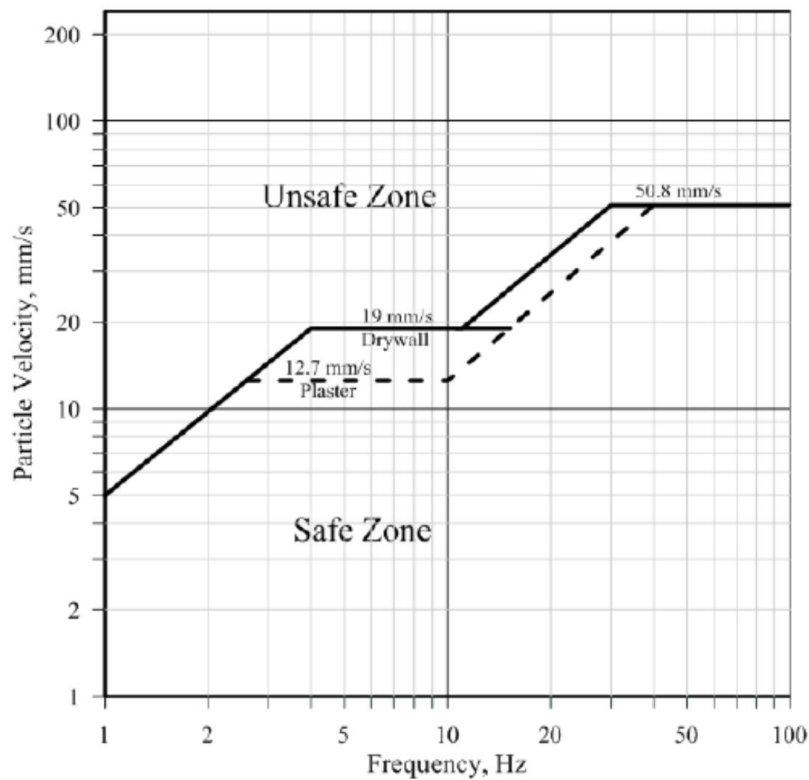


Figure 2.5: Criteria for safe level blasting as per the USBM RI 8507 code (Siskind, 1980; Uysal and Cavus, 2013)

Siskind et al. (1980) stressed the need of implementing these PPV constraints to guarantee that blasting activities are conducted responsibly and sustainably. This enforcement is critical to balancing between the needs of resource exploitation and environmental as well as public health concerns. Adherence to these laws helps maintain the integrity of both natural ecosystems and developed environments in areas affected by blasting activities.

Several factors can be considered in the quest for a balance between rock fragmentation and environment. Chief among them include the inter-hole delay timing and the magnitude of explosive energy expended. The impact of blasting on the surrounding areas can be reduced by coordinating the explosive detonations through proper blast timing design (Saadatmand Hashemi and Katsabanis, 2020). This way, the possibility of excessive ground vibrations and noise can be mitigated against. Furthermore, minimising negative effects while attaining the intended rock fragmentation

requires careful control of explosive energy. Blasters can ensure that the energy released is sufficient to break up the rock without creating excessive noise or vibration by adjusting the type and quantity of explosives used (Dotto and Pourrahimian, 2024).

In terms of ground vibrations, it should be noted that the mass of explosives used within a blast is directly proportional to the level of ground vibrations (Hosseini et al., 2023). Numerous studies have shown that greater explosive loads cause higher ground vibrations (Khandelwal and Singh, 2006; Elevli and Arpaz, 2010; Park et al., 2021). This association occurs because larger charges produce more energy when detonated. This, in turn, results in greater seismic waves that propagate across the surrounding rock mass.

The mass of explosives can also be influenced by the length of stemming. The connection between the mass of explosives utilised and the length of stemming is critical for minimised ground vibrations. This is because the role of stemming is to disperse the explosive energy across the rock mass. Indeed, when the stemming length is properly matched to the explosive charge, this helps contain the energy within the borehole. The explosive energy is then directed more efficiently toward rock fragmentation. As a result, the energy discharged into the surrounding earth is reduced.

If the stemming length is too short relative to the volume of the explosive charge, the energy from the explosion may not be fully utilised for rock fragmentation. Instead, this poorly restricted energy can escape into the surrounding rock. As a result, additional ground vibrations are generated, which can impact nearby structures. On the other hand, longer stemming length can help retain more of the explosive energy within the blast bench. This retention allows for a more controlled release of energy, reducing the risk of excessive ground vibrations. According to Sayed-Ahmed and Naji (2013), stated that striking this balance is essential to improving blast effectiveness while minimizing harm to surrounding structures and ecosystems.

2.3. Effects of rock fragmentation on downstream operations

The central purpose of blast design is to break the in-situ rock and prepare it for subsequent loading and hauling. It is therefore the goal of every mine to produce optimum rock fragments that are suited to the capacity of equipment available on site. The fleet of equipment includes trucks loaders, hydraulic shovels, dump trucks and crushers.

Rock fragmentation is commonly accepted to affect the performance of downstream processes. Oraee and Asi (2006) explained that good rock blast fragmentation leads to efficient loading, hauling, and crushing. Good fragmentation also enhances the economic health of a mine by cutting down the costs associated with secondary blasting. Furthermore, good rock fragmentation reduces the energy required for loading and crushing (Lawal, 2021).

Kanchibotla (2003) argued that a blast is deemed optimal when good digging and loading are experienced. It is for this reason that Figure 2.6 is often used to estimate the optimum blast. A direct link between optimum blast and downstream operational costs is apparent. As the blasting effort increases, both the digging and hauling costs decrease. A compromise can therefore be reached where blasting costs can justify downstream digging and hauling costs.

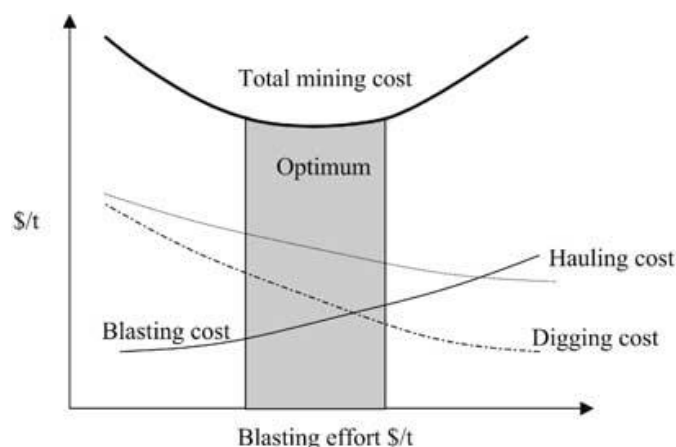


Figure 2.6: Relationship between blasting costs and downstream operational costs (Kanchibotla, 2003)

Rosales-Huamani et al. (2020) highlighted that understanding the interplay between operating costs and blasting costs is important for mining companies. For instance, blasting costs can increase due to inefficient blasting practices and lead to greater mine operating costs. Consequently, downstream processing costs may in turn increase. As can be seen in Figure 2.7, higher blasting costs may result in lower crushing costs because better rock sizes are produced by using more explosive charges. This means that the slight increase in explosive consumables yields great return downstream. Conversely, poor rock fragmentation may result in higher crushing costs. An ideal blasting method should therefore aim to establish optimal rock fragment sizes and curtail subsequent operational costs associated with crushing and hauling. In other words, effective rock fragmentation is about carefully managing blasting in view to minimise downstream energy and costs. Indeed, excessive blasting expenditures may raise the total mine operating costs even if they lead to lower costs elsewhere. This means that blasting costs should not be capped when seeking to produce optimal fragments for easier downstream handling. This balance maximises efficiency throughout the entire value chain while ensuring that overall operating costs are kept as low as possible.

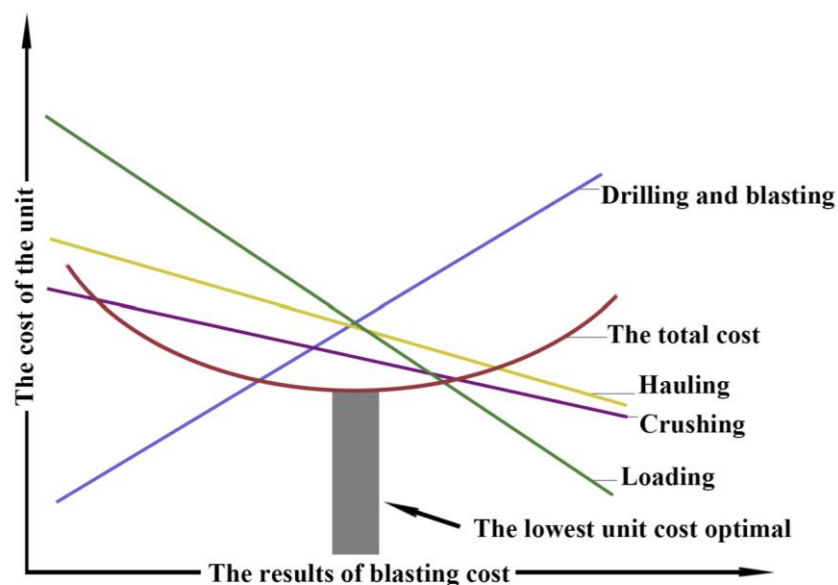


Figure 2.7: Relationship between operational cost units and blasting costs
(after Rosales-Huamani et al., 2020)

Kim (2010) was able to argue that optimal fragmentation can lead to cost-effective crushing. Indeed, the researcher examined experimentally the effect of powder factor on fragmentation. Note here that the powder factor, which is commonly expressed in kg/m^3 , can be defined as the quantity of explosives used per unit volume of rock (Sanchidrián et al., 2022). Kim (2010) then found that rock fragmentation is directly influenced by powder factor. This means that the ideal rock breakage can be achieved with a well-calibrated powder factor that can produce smaller and easier-to-handle pieces. On the other hand, an improper powder factor may result in either too much or too little explosive breakage.

Ozdemir and Kumral (2019) further illustrated the relationship between mining activities and rock fragmentation. Here, mining activities refer to drill and blast, loading, hauling, and crushing. Figure 2.8 shows how the unit costs of the four aforementioned mining operations (on the y-axis) relate to rock fragmentation (on the x-axis). Since fragmentation quantifies the extent to which rock is broken during blasting, a rise in fragmentation along the x-axis typically indicates smaller fragments. A lower degree of fragmentation produces coarser rock fragments, whereas smaller fragments indicate finer breakage. As shown in Figure 2.8, the upward trend of the plot shows that the combined drilling and blasting costs increase with rock fragmentation. This happens because it takes more explosive energy, greater drilling accuracy, and higher drill density to achieve finer rock fragmentation, all of which contribute to rising costs. When comparing loading costs and rock fragmentation, the declining trend shows that increasing fragmentation lowers loading costs. Compared to larger and irregular blocks, smaller fragments are easier to handle and load onto haul trucks and conveyors. Smaller fragments therefore require less time and energy. In the same manner, hauling costs tend to decrease as rock fragmentation increases. Because they are more manageable and portable, smaller pieces increase haulage efficiency and lessen equipment wear and tear. Additionally, as rock fragmentation increases relative to the crushing unit, the corresponding plot displays a decline in crushing costs. This is because the crusher needs

less effort and therefore less energy to break down material that is already closer to the desired size.

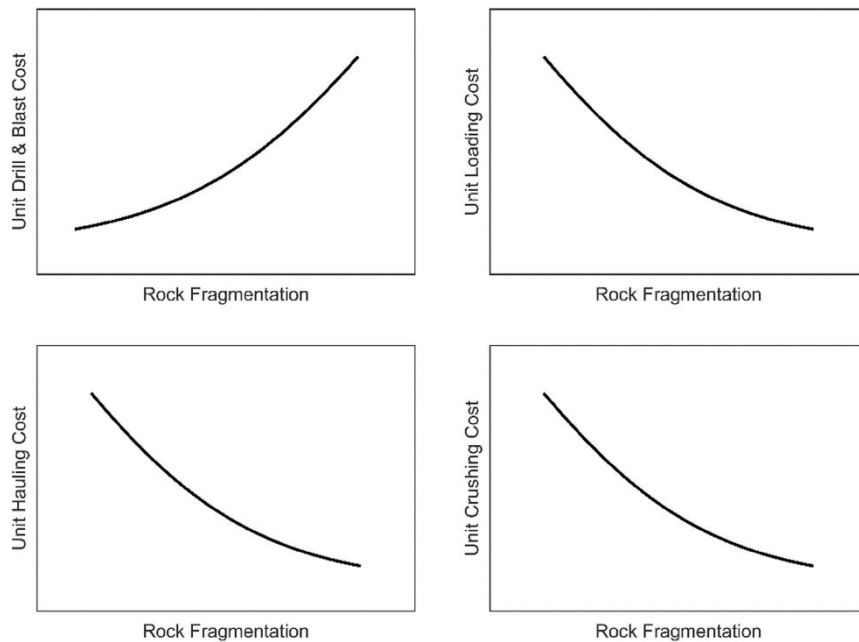


Figure 2.8: Relationship between rock fragmentation and mining activities
(Ozdemir and Kumral, 2019)

Choudhary et al. (2017) argued that mining operations must balance productivity and costs to achieve optimal performance. They emphasized that both factors need careful management to ensure efficiency and profitability. In order to effectively control and manage these factors, one needs to be able to measure rock fragmentation. The next section discusses how this can be done.

2.4. Methods for the estimation of rock fragmentation

Rock fragmentation analysis or the ability to evaluate the size distribution of rock fragments produced by blasting is critical to mining operations. Indeed, measuring fragmentation provides information useful for the optimisation of downstream operations. And optimised fragmentation can increase overall productivity, decrease energy consumption in crushers, and lessen wear on equipment. In order to achieve effective fragmentation, a balanced range of rock sizes with limited fines and boulders must be produced. This is to

ensure a seamless operation as excessive fines and boulders tend to significantly hinder on the performance of equipment.

Several analysis methods have been developed to measure rock fragmentation. They can be classified into direct and indirect approaches as shown in Figure 2.9. In direct methods, fragmentation is measured physically on a muckpile using a set of large vibrating screens. Although this can produce a true reflection of the muckpile size distribution, direct methods are costly and time consuming (Sudhakar et al., 2005; Babaeian et al., 2019). It is for these reasons that indirect methods have been gaining popularity in the mining industry (Sereshki et al., 2016; Tavakol Elahi and Hosseini, 2017; Babaeian et al., 2019; Kumar and Shaik, 2020; Nanda and Pal, 2020).

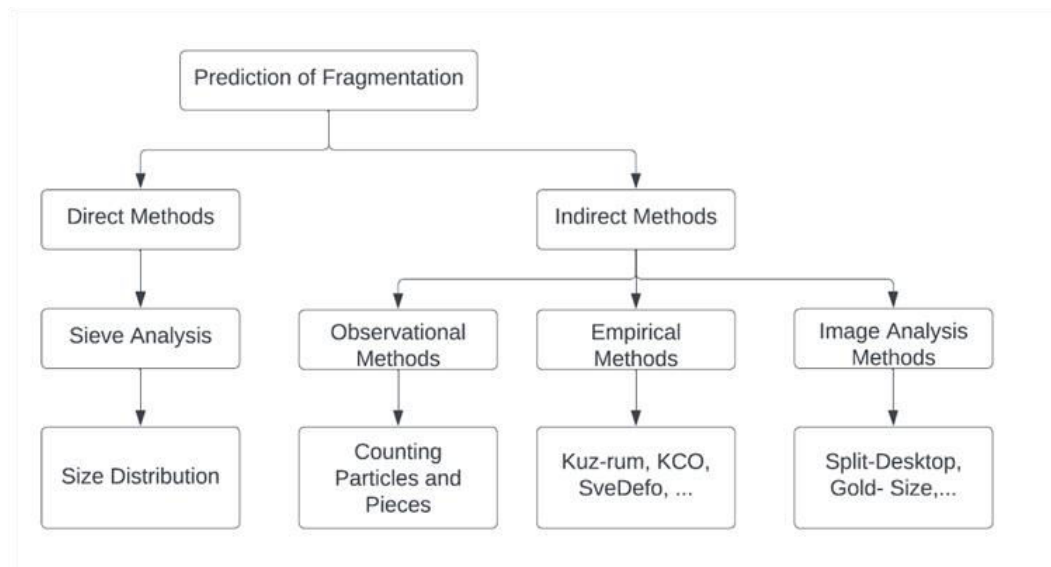


Figure 2.9: Main prediction and measurement methods of rock fragmentation (after Sudhakar et al., 2005)

Indirect methods enjoy a good balance between accuracy and efficiency. They are regarded as less time-consuming and cost-effective (Hettinger, 2015). This is why indirect analysis methods, such as visual inspection, empirical studies, and image analysis are widely used. This section focuses on indirect analysis techniques. The review specifically looks at image analysis and empirical estimation models of rock fragmentation.

2.4.1. Image analysis of rock fragmentation

Kumar and Shaik (2020) define image analysis as a system that uses advanced techniques such as segmentation and computer-aided detection to help evaluate the quality of the fragment size distribution in a muckpile. Image analysis typically entails the use of high-resolution cameras to capture still photographs of the blasted rock fragments. A specialised software is then used to process these photos and determine the sizes of the rock fragments as well as their distribution. The information gathered aids in evaluating the efficacy of the blasting process and inform the design modifications required for the best rock fragmentation.

There exist in the market various software packages and image capturing systems designed to facilitate the digital image analysis of fragmentation sizing. Some of the software packages include WipFrag, Split Desktop, PortaMetrics, GoldSize, Fragscan, and BlastFrag (Hettinger, 2015; Tavakol Elahi and Hosseini, 2017; Hekmat et al., 2019; Babaeian et al., 2019; Taiwo and Adebayo, 2022; Taiwo et al., 2024). In terms of workflow, many of these digital image analysis tools share similar operating principles and usually require a reference scale within the photographic frame for accurate measurements. To illustrate this, Figure 2.10 provides an overview of the WipFrag analysis process. This begins with image acquisition of the muckpile together with a reference scale object. The image must be clear with reduced shading and enhanced contrast so that optimal results can be achieved with the software. As such, high-resolution cameras are used to ensure the best possible outcome. The image is then imported into the WipFrag software while a reference scale is defined to ensure accurate measurements. The software then uses Edge Detection Parameters (EDP) to automatically identify and outline individual rock fragments within the image of the blasted muckpile as seen in Figure 2.11. The user can then manually adjust these outlines using particle edge detection editing tools if needed to improve accuracy. Once the picture has been analysed, the program provides graphs of the fragmentation sizing referred to as Particle Size Distribution (PSD). PSD statistics such as the mean size (i.e., 50-

percentile size or D50) as well as the 10-percentile (D10) size and the 90-percentile (D90) size of the muckpile distribution are also produced (see Figure 2.11).

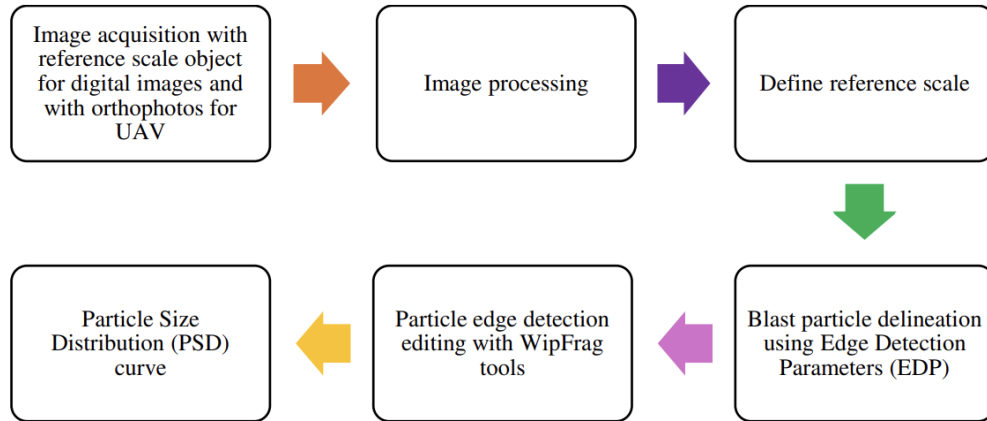


Figure 2.10: Process flow for the blast image analysis with the WipFrag 4 software (Taiwo et al., 2024)

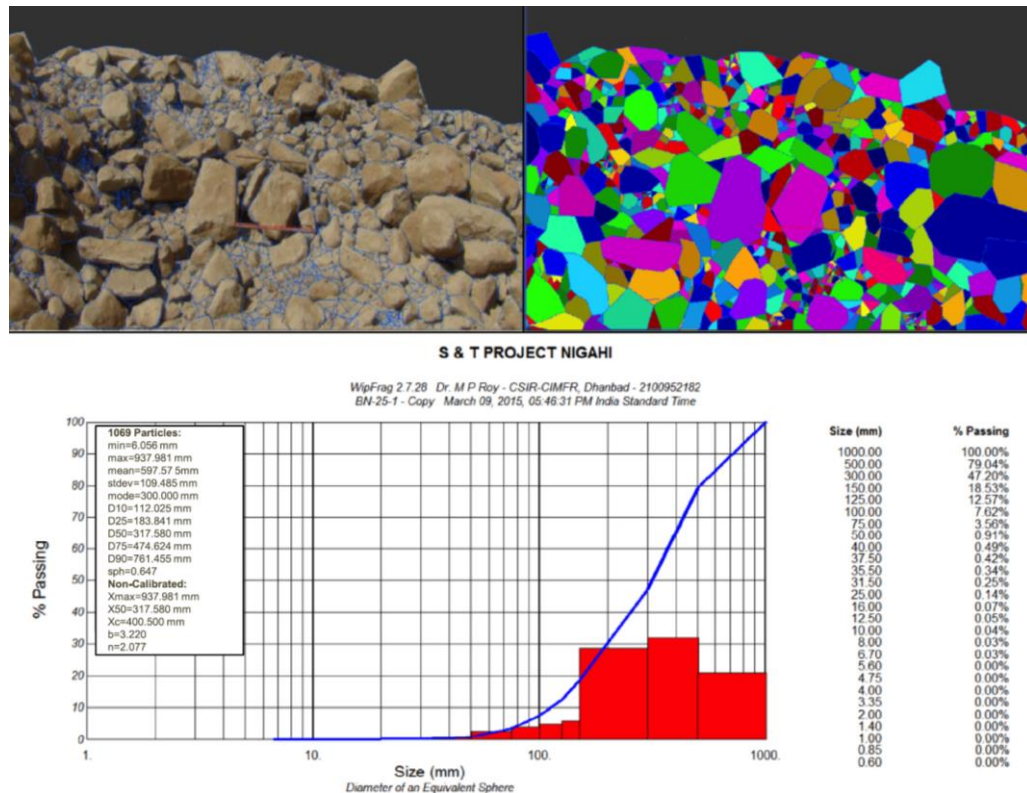


Figure 2.11: Histogram, netting, contouring, and cumulative size curve view of the broken muckpile from the blast block (Singh et al., 2015)

In recent years, researchers have increasingly favoured image analysis techniques over empirical methods (Shehu et al., 2020). This is because they significantly reduce the time for measuring rock fragmentation without interfering with mining operation (see for example Roy et al., 2016; Kumar and Shaik, 2020; Omotehinse and Taiwo, 2023; Shi et al., 2023; Taiwo et al., 2024). However, image analysis methods often have limited accuracy recognizing rock fragments due to factors such as overlapping particles, camera angles, and lighting conditions (Sereshki et al., 2016). This may lead to incorrect size distribution measurements, which can cause large errors in the automated determination of particle boundaries.

Several studies have highlighted prevailing issues around the measurement of the individual dimensions of overlapping rock fragments. For example, Al-Thyabat and Miles (2006) reported that the results of traditional software, such as Split Desktop, frequently deviate greatly from the true values because of errors the separation of objects. According to the two researchers, automated techniques can process images quickly, but they might not always align with real world measurements. This then leads to differences in particle size distributions. They suggested that better results can be obtained by adjusting filter dimensions and thresholds for selected images. Additionally, more study is required to create algorithms that can adapt to various camera settings and positions.

In 2020, Shehu and co-workers effectively conducted a study using the WipFrag software. While highlighting its user-friendly interface, the group of researchers reported that the WipFrag software offered superior analysis than the Split Desktop software tested by Al-Thyabat and Miles (2006). Moreover, Shehu et al. (2020) indicated that the efficiency of blasting procedures could be greatly increased by incorporating WipFrag image analysis into quarry operations. These encouraging findings mean that real-time visualization and quantification of rock fragmentation can inexpensively result in increased safety and lower operating costs.

2.4.2. Empirical estimation of rock fragmentation

In the field of fragmentation analysis, empirical models are essential tools that provide a quick, practical and efficient way of predicting the size distribution of fragmented rocks. These models approximate rock fragmentation based primarily on blast design parameters and empirical data. According to Thornton et al. (2001) and Babaeian et al. (2019), empirical estimation methods cannot directly determine the characteristics and geometries of the rock mass. But the underlying models are still among the most effective and fastest way to estimate rock mass fragmentation.

Empirical models have been widely adopted in mining and quarrying operations due to their simplicity and ease of application. They provide valuable insights into the relationship between the resulting fragmentation size distribution and key blasting parameters such as explosive type, charge weight, and blast geometry (Adebola et al., 2016; Alipour et al., 2018; Ouchterlony and Sanchidrian, 2019). This capability allows for the optimisation of blasting practices which then leads to improved efficiency and reduced operational costs.

In this section, two commonly accepted empirical fragmentation models are reviewed. These are the widely recognized Kuznetsov-Rammler (Kuz-Ram) model as well as its modified version known as the Kuznetsov-Cunningham-Ouchterlony (KCO) model. The objective is to provide a comprehensive understanding of how empirical methods contribute to fragmentation analysis and blast optimisation while highlighting their limitations.

2.4.2.1. Kuz-Ram fragmentation model

According to Hekmat et al. (2019), the Kuznetsov-Rammler model is one of the most widely used empirical models of blast fragmentation. The model describes the fragment size distribution of the resulting muckpile in relation to the explosives used, the rock mass, and blast design parameters (Ouchterlony and Sanchidrian, 2019).

Cunningham (1987) presented the model as a fusion of the empirical model by Kuznetsov (1973) and the Rosin-Rammler distribution. Hence, the name Kuznetsov-Rammler model or Kuz-Ram for short.

The Kuz-Ram model is a three-parameter equation expressing the relation between the mean size (X_{50}) of blasted fragments and the powder factor. It can be expressed as follows (Cunningham, 1987):

$$X_{50} = A \frac{Q^{1/6}}{K_P^{0.8}} \left(\frac{115}{R_{EE}} \right)^{0.633} \quad (2.5)$$

Where A is the rock mass factor

Q is the explosive mass per blast hole (kg)

K_P represents the powder factor or specific charge (kg/m³)

R_{EE} represents the explosive relative effective (MJ/kg). This represents the required energy to effectively blast a rock.

The rock mass factor (A) in Equation (2.5) considers the density, mechanical strength, elastic properties, and fractures of the rock mass. It can be defined as follows (Cunningham, 1987; Adebola et al., 2016):

$$A = 0.06 \times (RMD + JF + RDI + HF) \quad (2.6)$$

Where RMD denotes the mass description

JF represents the joint factor

RDI stands for the rock density influence

HF represents the hardness factor.

To better quantify the rock factor (A) in Equation (2.6), the Kuz-Ram model uses the Blastability Index proposed by Lilly (1986). This index, which considers various geomechanical parameters of the rock, provides a more precise measurement of rock blastability. Blastability, here, refers to the ability of a rock mass to be efficiently broken up by blasting (Bhatawdekar et al., 2022). By integrating the Blastability Index, the Kuz-Ram model enhances its ability to predict fragmentation outcomes. Parameters characteristic of the Blastability Index entering into the definition of the rock factor (A) are summarised in Table 2.1. They describe how easy it is to blast

a rock mass using measurable variables like rock hardness, joint spacing, and joint condition.

Table 2.1: Rock factor parameters and ratings (after Gheibie et al., 2010)

<i>RMD</i>		Rock Mass Description
Powdery/friable		10
Vertically jointed		JF^*
Massive		50
<i>JS</i>		Vertical Joint Spacing
< 0.1 m		10
0.1 m to 1m		20
Wide (m)*		50
<i>JA</i>		Joint Plane Angle
Dip out of face		20
Strike perpendicular to face		30
Dip into face		40
<i>RDI</i>		Rock Density Influence
$RDI = 25 RD^* - 50$		RD ; Rock Density (t/m^3)
<i>HF</i>		Hardness Factor
$Y/3$		If $Y < 50$ GPa
$UCS^*/5$		If $Y > 50$ GPa
	Meaning	Unit
Y	Young's modulus	GPa
UCS	Uniaxial Compressive Strength	MPa
$JF = JS + JA$		

The Kuz-Ram model adopts the Rosin-Rammler distribution to describe the muckpile size distribution. This distribution is more conveniently expressed as the mass fraction passing a specific screen size X . This is because broken rock has been shown to obey the Rosin-Rammler distribution (Delagrammatikas and Tsimas, 2004; Faramarzi et al., 2013; Alderliesten, 2013; Tosun et al., 2014). It is in this light that the Kuz-Ram model

representing the percentage of material passing the screen mesh of size X can be defined as follows (Cunningham, 1987 & 2005):

$$R_p = 1 - \exp \left[-0.693 \left(\frac{X}{X_{50}} \right)^n \right] \quad (2.7)$$

Where R_p represents the percentage of material that passes through a screen with a specific mesh size X (in cm)

X_{50} represents the 50% passing size of the entire muckpile size distribution given by Equation (2.5)

n represents the uniformity exponent of the resulting size distribution.

The uniformity index (n) accounts for the effect of blast design parameters such as hole diameter, burden, spacing, hole length, and drilling accuracy amongst others (Cunningham, 1987 & 2005):

$$n = \left[2.2 - 14 \left(\frac{B}{d} \right) \right] \left[0.5 \left(1 + \frac{S}{B} \right) \right]^{0.5} \left[1 - \frac{W}{B} \right] \left[\frac{L}{H} \right] \quad (2.8)$$

Where B is the burden or the distance between two successive rows of blastholes (m)

S is the blast design spacing (m)

D is the hole diameter (mm)

W is the drilling accuracy standard deviation (m)

L is the total length of the drilled hole (m)

H is the bench height (m).

In essence, the Kuz-Ram model provided in Equation (2.7) stands as a significant tool in the field of rock fragmentation analysis. It offers a comprehensive method for predicting the size distribution of fragmented rock resulting from surface mine blasting operations. Two of the three parameters making up the Kuz-Ram model are given by Equations (2.5) and (2.8) while the third is the selected fragment size X .

It is important to highlight that the Kuz-Ram model has been applied extensively. However, it has several limitations which has prompted to the development of alternative models such as the KCO model. Shehu et al.

(2022) compared WipFrag measurements against the Kuz-Ram model. Three trial blasts were conducted to demonstrate that the Kuz-Ram model overestimated the muckpile size distribution as evidenced in Figure 2.12.

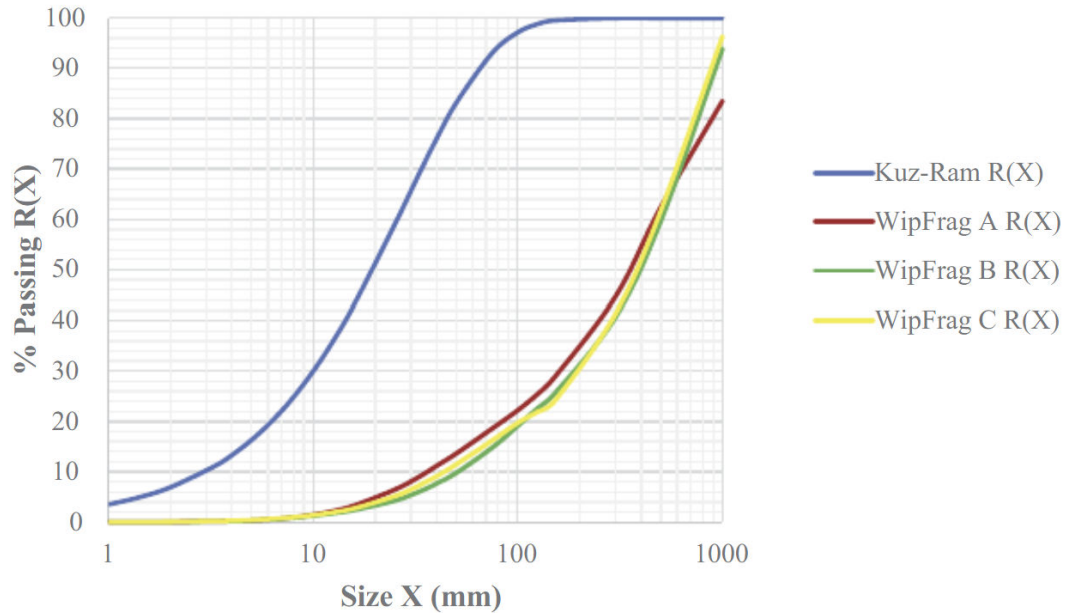


Figure 2.12: Size distribution curves estimated with WipFrag and measured from three viewpoints A, B, and C versus the Kuz-Ram model at the FYS granite quarry (Shehu et al., 2022)

According to Adebola et al. (2016), the overestimation can be attributed to the inability of the Kuz-Ram model to sufficiently account for variations in rock characteristics including density and strength. The generic approach of the model might not adequately account for the fact that different rock types react differently to blasting. This could then cause the model to overestimate corresponding fragment sizes. The KCO model, covered next, considers additional factors to increase prediction precision and flexibility.

2.4.2.2. Kuznetsov-Cunningham-Ouchterlony fragmentation model

Ouchterlony (2005) was the first to propose and implement the Kuznetsov-Cunningham-Ouchterlony (KCO) model. Ouchterlony and Sanchidrián (2019) then presented this model as an improved version of the Kuz-Ram model. The KCO model has subsequently been found to be helpful in

surface mining and quarrying operations. This is because it is able to closely estimate the fragment sizes of the blasted rock which allows for the seamless optimisation of the loading, hauling, and crushing processes.

One of the newly incorporated variables in the KCO model is the Swebrec® function. This is a mathematical function that describes the size distribution of rock fragments as shown below (Ouchterlony, 2005):

$$P(x) = \frac{1}{\left\{ 1 + \left[\frac{\ln\left(\frac{X_{max}}{x}\right)}{\ln\left(\frac{X_{max}}{x_{50}}\right)} \right]^b \right\}} \quad (2.9)$$

Where $P(x)$ denotes the percentage fraction of fragments passing through a sieve size X while the term X_{max} refers to the maximum allowable fragment size in each distribution. The latter is defined by considering in situ block size, burden or spacing as shown in Equation (2.10):

$$X_{max} = \max(\text{in situ block size}, S \text{ or } B) \quad (2.10)$$

Furthermore, the term b in Equation (2.9) denotes the curve undulation parameter which is given by (Ouchterlony, 2005):

$$b = \left[2 \ln 2 \cdot \ln \left(\frac{X_{max}}{x_{50}} \right) \right] \cdot N \quad (2.11)$$

Another set of equations that forms the core of the KCO model is presented in Equations. These equations are crucial for the functionality and greater accuracy of the model (Ouchterlony, 2005):

$$x_{50} = A Q^{1/6} \left(\frac{115}{S_{ANFO}} \right)^{19/20} g(N) \quad (2.12)$$

$$g(N) = \frac{\ln 2^{\frac{1}{N}}}{\Gamma\left(1 + \frac{1}{N}\right)} \quad (2.13)$$

$$N = \left(2.2 - \frac{0.014B}{d} \right) \left(1 - \frac{SD}{B} \right) \sqrt{\frac{1+SD}{B}} \left[\frac{|L_b - L_c|}{L_{tot}} + 0.1 \right]^{0.1} \left(\frac{L_{tot}}{H} \right) \quad (2.14)$$

where x_{50} represents the average passing particle size of the entire distribution

Q is the charge weight per hole (kg)

q is the specific charge (kg.m^{-3})

B is the burden (m)

S is the spacing (m)

S_{ANFO} is the explosive's weight strength relative to ANFO (%)

L_b is the length of the bottom charge of explosives (m)

L_c is the length of the column charge of explosives (m)

SD is the standard deviation of drilling accuracy (m).

Additionally, the KCO model relies on readily available parameters defining the properties of the rock mass. Specifically, the rock mass factor A is defined as follows (Ouchterlony, 2005):

$$A = 0.06 (RMD + RDI + HF) \quad (2.15)$$

Where RMD is used to describe the density of the rock mass, which has a big impact on how the rock responds to stress including blasting. It is an important factor that affects the energy needed for fragmentation. RMD is rated according to the description in Table 2.1. However, when rock joints are vertical RMD reduces to JF which is the joint factor represented by the following equation (Mutinda et al., 2021):

$$JF = JPS + JPA \quad (2.16)$$

with JF being the joint factor while JPS is the joint plane spacing and JPA is the joint plane angle.

The term RDI in Equation (2.15) is the rock density index, a measurement that helps in determining the density of rock material and may have an impact on rock fractures during blasting. It is dependent on the rock density ρ as follows (Ouchterlony, 2005):

$$RDI = [0.025 \cdot \rho] - 50 \quad (2.17)$$

Finally, the term HF in Equation (2.15) represents hardness factor. It is given by (Ouchterlony, 2005):

$$HF = \begin{cases} \frac{E}{3} & \text{if } E < 50 \\ \frac{\sigma_c}{5} & \text{if } E > 50 \end{cases} \quad (2.18)$$

Where HF is the hardness factor which considers compressive strength σ_c (MPa) and Young's modulus E (GPa).

Shortcomings inherent to the Kuz-Ram model are generally addressed by the KCO model, especially when it comes to predicting fragment size distributions in the finer range and the upper limit of block sizes. This was accomplished by using the Swebrec© function, which offers a more realistic depiction of the fragmentation process. A study by Mutinda et al. (2021) focused on two quarries in Kenya; namely, the Bisil and Simba quarries. Each quarry witnessed a total of six blasts the fragment size distributions were all measured by WipFrag image analysis. The study demonstrated that the KCO fragmentation model offered a better prediction of the fine and coarse fractions of the muckpile compared to the Kuz-Ram model. Notwithstanding this, the KCO model was noted to yield contrasting results for boulders. Indeed, the model overestimated the mass fraction of boulders produced at the Simba quarry while underestimating that produced at the Bisil quarry. The different rock mass properties at the two locations were cited as the cause of this disparity. But across all blast rounds under study, the model typically predicted boulders with an error of less than 10%.

Another study by Lawal (2021) also demonstrated the effectiveness of the KCO model in practical applications by showing a closer match to the actual measured fragment sizes. The KCO model achieved an overall error of about 3.5% compared to over 60% for the original Kuz-Ram model. Furthermore, Lawal (2021) indicated that the KCO model adapts to different rock types and blasting conditions which makes it a useful tool for various mining scenarios. Compared to the widely used Kuz-Ram model, which might not function well in different situations, this flexibility is a major benefit. However, Lawal (2021) also underscored the limitations of the KCO model one of which being that the model do not fully account for the diverse

geological conditions encountered in various environments. Rock types and structures may also vary and result in inconsistent fragmentation behaviour that the model may not be able to capture well. To increase the model accuracy and wider applicability in mining operations, these limitations must be addressed.

2.4.2.3. *Extended Kuz-Ram fragmentation model*

The extended Kuz-Ram model was developed to address particularly the low prediction of the fraction of fines generally observed with the Kuz-Ram model (Cunningham, 2005). It incorporates the initiation timing and delay as new blast parameters that were not considered in the original Kuz-Ram model. This allows for a more accurate prediction of fragment sizes under varying blasting conditions. One of the main features of the extended Kuz-Ram model is its ability to include calibration factors that adapt the model to specific blasting sites. This means that the model can be fine-tuned based on the unique characteristics of the rock being blasted to obtain better predictions of rock fragment sizes.

Mathematically speaking, the extended Kuz-Ram model continues to use Equation (2.7). However, the mean size X_{50} and the uniformity index n differ from the original Kuz-Ram model as follows (Cunningham, 2005):

$$X_{50} = A_t A \left[\frac{Q^{1/6}}{K_p^{0.8}} \left(\frac{115}{R_{EE}} \right)^{0.633} \right] C(A) \text{ with } 0.5 < C(A) < 2 \quad (2.19)$$

$$n_{ext.} = n_s \sqrt{\left(2 - \frac{30B}{d} \right)} \sqrt{\frac{1+\frac{S}{B}}{2}} \left(1 - \frac{W}{B} \right) \left(\frac{L}{H} \right)^{0.3} \left(\frac{A}{6} \right)^{0.3} C(n) \quad (2.20)$$

Ouchterlony and Sanchidrián (2019) were able to show that the fundamental components of Equations (2.5) and (2.8) remained unchanged. However, the two multiplicative factors $C(A)$ and $C(n)$ are the new factors added to Equations (2.19) and (2.20). They are used for calibration to site-specific conditions. An additional element is the timing factor A_t defined below (Cunningham, 2005):

$$A_t = \begin{cases} 0.66 \tau^3 - 0.13 \tau^2 - 1.58 \tau + 2.1 & \text{if } \tau \leq 1 \\ 0.9 + 0.1 (\tau - 1) & \text{if } \tau \geq 1 \end{cases} \quad (2.21)$$

Where $\tau = \Delta T / T_{max}$ with ΔT representing the (nominal) in-row delay (ms) and $T_{max} = 15.6B / C_p$ with C_p being the P-wave velocity (m/ms).

In addition, the term n_s in Equation (2.20) is descriptive of the scatter or standard deviation s_t of the in-row delay time ΔT which, in turn, is represented by the scatter ratio R_s (Cunningham, 2005):

$$n_s = 0.206 + \left(1 - \frac{R_s}{4}\right)^{0.8} \text{ with } R_s = 6 \frac{s_t}{\Delta T} \quad (2.22)$$

The other change to the extended Kuz-Ram model was made around the rock factor A . The joint factor JF was now excluded from Equation (2.6) to basically reduce the rock factor to Equation (2.15).

The extended Kuz-Ram model has made it possible to account for the use of electronic delay detonators instead of pyrotechnic delay ones. Cunningham (2005) noted that employing 9-ms electronic delays or 25-ms pyrotechnic delays improved the uniformity index. These detonators also eliminated material of size over 1 m and decreased fragment size distributions, making them appealing for test blasting. Further test blasting was done by Ouchterlony and Paley (2013) at the Red Dog Mine. The two researchers considered the products discharged by the crusher processing the muckpile from bench blasts under different patterns and delay combinations. Digital image analysis was done for 17-ms pyrotechnic detonators and for electronic detonators with delays of 8 ms and 25 ms across 26 stockpiles each holding 200 000 t. While there was no minimum in the 8 – 25 ms delay range, results showed a decrease in X_{50} with shorter delay times. In contrast to predictions from the extended Kuz-Ram model, a steeper fragmentation size distribution (i.e., smaller X_{75}/X_{25} ratio) was observed for both the 8-ms electronic and 17-ms pyrotechnic detonators.

Lastly, Ouchterlony and Sanchidrián (2019) stated that the range of blasting conditions, including drilling accuracy and rock mass characteristics, has

made it difficult to systematically test the capability of the extended Kuz-ram model. As such, extensive testing over many rounds is necessary, but this is frequently obscured by geological variations.

2.5. Conclusion

The literature study covered in this chapter has identified blast design parameters, stemming length, and explosive charge mass as controllable variables that affect rock fragmentation. It has therefore become evident that attaining good rock fragmentation requires optimizing all these parameters. Based on the review, greater explosive charge and suitably modified stemming length have been found to have a substantial effect on fragmentation. This ultimately leads to increased throughput from downstream crushers. Efficient fragmentation has also been demonstrated to increase throughput while lowering processing costs. Reduced fragment size in turn enhances the efficiency of the crushing process.

In terms of rock fragmentation modelling, three prominent empirical models were reviewed: the Kuz-Ram model, the KCO model, and the extended Kuz-Ram model. Their respective limitations highlighted the need for empirical validation and refinement. Their inability to fully capture variations caused by blast timing delays and in-situ rock properties represents another notable limitation. Furthermore, it is still unclear how well the KCO model, purported to be the most flexible and accurate, predicts fragmentation in various geological settings. Finally, despite a large body of research available on rock fragmentation, there is a substantial knowledge gap in quantifying the compromise between stemming length and inter-hole delay and their combined effects on downstream crushing. Contemporary research has frequently discussed these elements separately without offering a thorough framework that unifies them into a single optimisation approach.

Chapter 3: Experimental work and data collection

The primary goal of this research is to assess the impact of stemming and timing on rock fragmentation and downstream crushing processes. In order to achieve this, a specific and systematic approach to data collection was adopted. The approach entailed collecting historical and on-site experimental data for analysis.

This chapter outlines the experimental methodology employed for the research. The chapter specifically delves on the protocols used to collect and evaluate experimental data. It also highlights the various environmental and safety considerations that were implemented throughout the study. These precautions were crucial for maintaining adherence to regulations and reducing the possible effects of blasting. Details of the scientific endeavour are presented in the subsequent sections of the chapter.

3.1. Introduction

The approaches used in this research comprised of historical data collection, field observation, and data evaluation as shown in Figure 3.1.

Firstly, historical data was reviewed from the blasting reports of the quarry. The main interest in these internal reports was stemming length and timing. The data pertaining to these two blast design parameters was used to establish the baseline performance of subsequent blasts. The data was also used to build a simulation model of the blast performance as a function of historical stemming and timing.

Secondly, field experimental work was conducted at the production benches. During the field experiments, the stemming length and the timing delay were systematically varied to meet the objectives set for the research. The remaining blast parameters such as burden, spacing, types of explosives, and stemming material were kept constant. This exercise was

performed to monitor the effects of stemming length and timing on blast fragmentation.

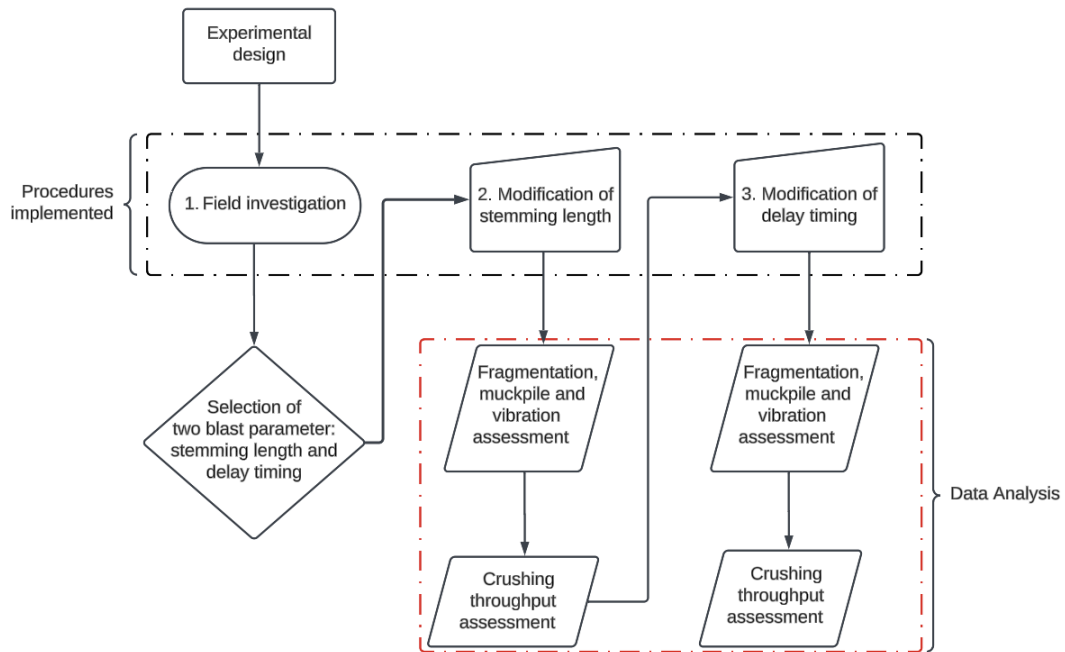


Figure 3.1: Schematic of experimental design (Source: Author's own design)

Lastly, the blast fragmentation data from the field work was evaluated using the WipFrag software. This specialised software package is an image processing program capable of accurately estimating muckpile size distribution as discussed earlier in Section 2.4.1. In addition to this, the crusher throughput on the plant processing the muckpile was examined as a way of gauging downstream performance resulting from a specific rock fragmentation.

The above steps summarised in Figure 3.1 are covered in detail in the sections below.

3.2. Collection of historical blast data

Mines are known for commonly archiving records of production data in the form of blast reports. The quarry that this study is based on is no different. This is in line with Section 4.16 of the South African Mine Health and Safety

Act (MHSA) about Explosives Regulations (MHSA, 2018) that requires for all blast reports to be kept for a minimum of five years. As such, the stored blast data was examined for rock fragmentation, instances of flyrock, and degrees of ground and air vibrations.

The examination of past blast reports followed a structure sequence of processes. Initially, relevant data was retrieved from the stored records of historical blasts of quarrying operations. The information extracted from these records included stemming length, tamping material, blast timing design, as well as burden and spacing for each blast. Subsequently, the shortlisted historical data was evaluated in terms of the influence of stemming length and initiation design on rock fragmentation, ground vibration and flyrock. The aim of reviewing the previous blast reports was to establish a performance benchmark for comparison against recent field data collected in Section 3.3.

In terms of reviewing the historical data, ten reports were initially scrutinised from January 2022 until February 2023 (Internal Quarry Document, 2022 – 2023). These 10 reports produced quarterly included crucial information such as blast patterns, types and quantities of explosives used, stemming lengths, delay timings, and fragmentation results. Each blast report was carefully reviewed and summarised into a comprehensive spreadsheet in Microsoft® Excel®. The information is not explicitly presented here for confidentiality reasons. This involved extracting key details and metrics from each report to create a structured and standardised dataset as shown in Table 3.1 along with their respective units. One key focus of Table 3.1 was to track changes in stemming and timing over the years and their impact on ground vibration, airblast, flyrock occurrence, and the fraction of boulders produced. This information helped filter some of the reports and provided guidance on which parameters to begin the research and analysis with.

Table 3.1: Summarised information extracted from blast reports between 2022 and 2023

Blasting parameters	Blast No.	Blast No.
Type of explosives	Emulsion	Emulsion
Burden	(m)	(m)
Spacing	(m)	(m)
Bench height	(m)	(m)
Average hole depth	(m)	(m)
Hole diameter	mm	mm
Inter-hole delay timing	(ms)	(ms)
Inter-row delay timing	(ms)	(ms)
Blast pattern	Staggered	Staggered
Final stemming length	(m)	(m)
Size of stemming material	10 mm	10 mm
Mass fraction of boulders produced (visual estimation)	%	%
Airblast	(dB)	(dB)
PPV	(mm/s)	(mm/s)
Flyrock within the blast radius?	Yes/No	Yes/No

The summarised data in Table 3.1 were then filtered specifically based on stemming length and blast timing. Three of the ten reports that were examined showed notable differences in terms of the two parameters; they were shortlisted for additional examination. A 20% or greater deviation from the baseline values was considered significant for this study because it was thought to have a significant effect on the results under investigation. Due to the lack of consistency in parameter measurements and possible inconsistencies in data collection techniques, reports older than 2022 were not taken into consideration.

The quarterly reports from January 2022 to January 2023 did not use the WipFrag software. WipFrag was introduced in February 2023 and before then fragmentation was estimated using a manual technique. The software

was added to the analysis in 2023 with the goal of improving the quality (i.e., accuracy and consistency) of the fragmentation analysis.

Finally, once the relevant historical data pertaining to blasting and crushing throughput was consolidated, their relationship was established using statistical techniques covered in Chapter 4. A performance baseline was also defined from the timeseries analysis against which current production data was compared for optimisation purposes. This systematic approach allowed for a better understanding of the blasting dynamics of the quarry and their implications on crushing throughput.

3.3. Collection of experimental field data

A systematic procedure was followed in collecting field experimental data to ensure accuracy and reliability. The experimental design was carried out in three phases based on the set research objectives. The stages included conducting trials in the field and making modification to the stemming length and the inter-hole delay timing. This was to investigate the influence of stemming length and inter-hole delay timing on blast results.

Six blast experiments were performed with three of them concentrating on stemming length while the remaining three looked at inter-hole delay timing. The number of blasts was chosen because the quarry could only afford six test blasts without experiencing significant disruptions to production. The three tests were labelled blasts #4, #5, and #6 for a stemming length of 2 m, 1.5 m and 1 m respectively. The other three blasts focused on inter-hole delay timing, that is, blasts #1, #2, and #3 with an inter-hole delay timing of 17 ms, 9 ms and 6 ms respectively. It is important to note that throughout the study, the inter-row delay timing remained fixed at 23 ms.

In each of the six blasts considered for testing, the type and size of stemming material, burden and spacing, type of explosives, and hole diameter remained constant. For illustration purposes, Table 3.2 provides a summary of the blast design parameters used for blasts #1 and #4

respectively. This strategy was to isolate any observed differences in rock fragmentation that would then be attributed to changes in stemming length and inter-hole delay timing respectively.

Table 3.2: An overview of blast design parameters for blasts #1 and #4

Blast design parameters	Blast #1	Blast #4
Date	15-Jun-2023	15-Jun-2023
Type of explosives	Emulsion	Emulsion
Burden (m)	2.5	2.5
Spacing (m)	2.8	2.8
Bench height (m)	14.5	14
Average hole depth (m)	15	14.5
Hole diameter (mm)	102	102
Number of holes	69	57
Inter-hole delay timing (ms)	17	6
Inter-row delay timing (ms)	23	23
Blast pattern	Staggered	Staggered
Final stemming length (m)	2.5	2
Powder factor (kg/m ³)	1.15	1.29
Size of stemming material (mm)	10	10

Prior to each test, the quarry manager and blaster had to approve the blast design. For example, the initial inter-hole delay timing was 17 ms in blast #1, then adjusted to 9 ms in blast #2. Additionally, the initial stemming was 2 m in blast #4 which was then modified to 1.5 m in blast #5. These changes required agreement between the manager and the blaster, as they carry legal appointments. Indeed, these appointments with the South African Department of Mineral Resources and Energy make them accountable for anything that happens on site.

The drilling operations were conducted using the Furukawa drill rig model HCR1500 – EDII shown in Figure 3.2. The rig was used to execute staggered drilling patterns with a hole diameter of 102 mm as per blasting

plans signed off by the quarry manager and the blaster. The subsequent sections detail the steps taken to prepare the blast.



Figure 3.2: Furukawa Drill Rig Model HCR1500 – EDII used on site
(Source: Author's own picture)

3.3.1. Adherence to the safety procedures on the blasting site

Before any blasting operation, strict safety protocols were followed for personnel safety and task efficiency. These protocols included the careful use of Personal Protective Equipment (PPE) and the placement of safety barriers and anchor points. Safety barriers and anchor points were strategically positioned, as depicted in Figure 3.3(A). Additionally, when working between barriers and at crest points, a safety harness was worn for added protection. Finally, blasting notices were erected at the main entrance to the production bench (Figure 3.3B). This was done to prevent unauthorized individuals from entering the charged bench area.

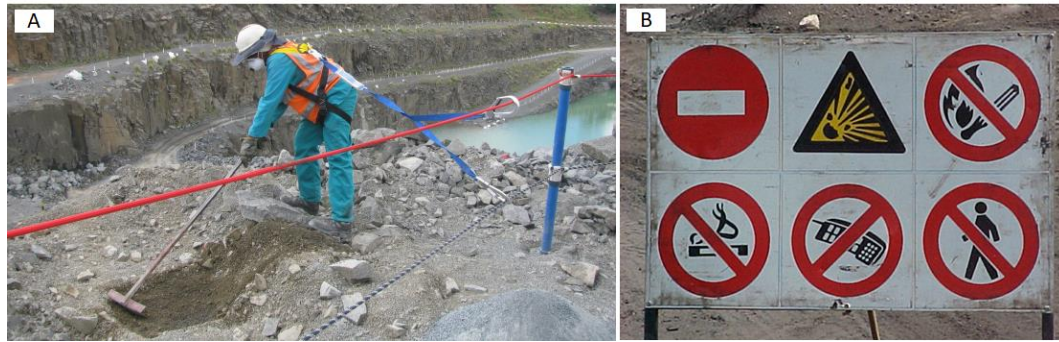


Figure 3.3: (A) Safety harness worn when working between barrier and crest attached to the safety barricade; and (B) Typical blasting signs (Source: Author's own picture)

3.3.2. Assessing the bench and marking drill holes

The blaster and the assistant first ensured that the bench area for blast was clean before proceeding with marking the bench. This step is crucial as a way of managing potential fly rocks.

To start the drill hole marking process, the initial step was to mark the burden of the front holes from the crest. Marking the front hole first was to ensure that there is sufficient burden. Indeed, too short a burden would increase the risk of flyrock; and in contrast, too long a burden may result in the formation of unwanted boulders. The burden and spacing were maintained at 2.5 m and 2.8 m respectively with all measurements taken using a tape measure.

After marking the front holes, the second row was next followed by the next up to the last row while maintaining the same burden and spacing pattern as seen in Figure 3.4. To indicate the location of drill holes on the bench, rocks were sprayed in red to show where the drill rig operation should place the drill cutting head. The pattern used in all experimental blasts followed a staggered schematic layout for marking the drill holes on the bench.



Figure 3.4: A typical staked bench ready for drilling at the quarry site
(Source: Author's own picture)

After marking the drill holes, a Trimble TSC3 controller and R4s Global Navigation Satellite System (GNSS) receiver in Figure 3.5 were used to generate the coordinates and depths of the holes. The two devices were paired together using Bluetooth® connection thereby enabling smooth communication. Once the connection was established, Trimble Controller was opened, and the General Survey module was selected in the controller device (Figure 3.5B). In this module, a new job was created and WG29 template was selected as it includes the relevant data for the Gauteng area. Based in Gauteng, South Africa, WG29 is a survey reference point that is a component of the countries geodetic control system. A consistent framework for surveying, mapping, and engineering projects in the area is provided by the accurate measurement and maintenance of these points.



Figure 3.5: (A) Trimble R4s Global Navigation Satellite System; (B) Trimble TSC3 controller; and (C) TSC3 and R4s GNSS mounted on a 2-m antenna (Source: Author's own picture)

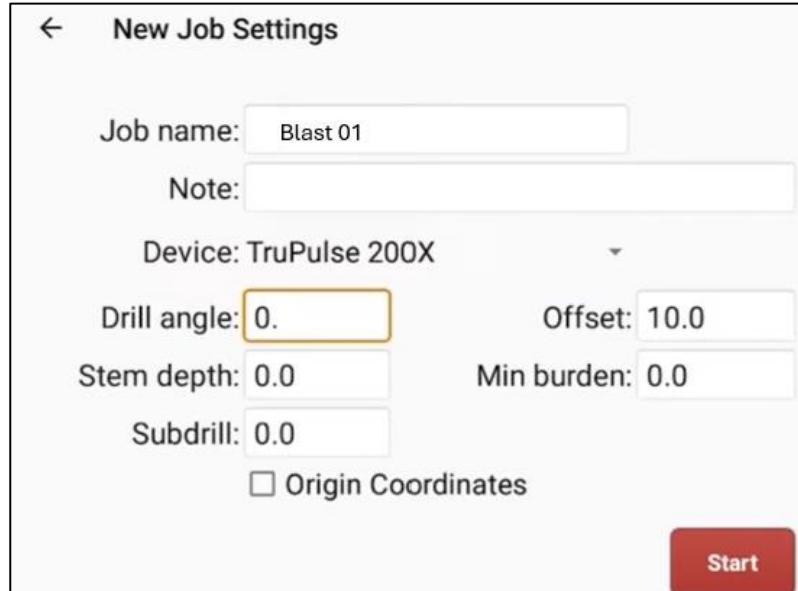
Following this, the measuring point option was used to identify the closest topographical base. During the drill hole survey, the antenna mount height was adjusted to 2 m to guarantee precise elevation readings (Figure 3.5C). For additional analysis, the data gathered around the locations of blastholes was saved in CSV format and then imported into the I-Blast program later covered in Section 3.3.4.

The next step of the design was to conduct a face profile as outlined in Section 3.3.3.

3.3.3. Two-dimensional (2D) face profiling of bench highwalls

Bench face profiling was conducted using a TruPluse 200 laser and a Samsung Galaxy Tab A 7.0 (2016) 8GB White Android 4G LTE Wi-Fi Tablet SM-T285 Model. The system was set up by pairing the TruPluse 200 laser, shown in Figure 3.7, with the Android tablet which had the FaceProfiler laser software installed on it. The FaceProfiler software was launched on the tablet, and thereafter a new job was created and named Blast 01 specifically for profiling the face corresponding to blast #1. The laser device was

recognized by the software, and both the drill angle and subdrill were set to zero as indicated in Figure 3.6. Face profiling started as soon as the devices were connected, and the task configuration was completed.



← New Job Settings

Job name: Blast 01

Note:

Device: TruPulse 200X

Drill angle: 0. Offset: 10.0

Stem depth: 0.0 Min burden: 0.0

Subdrill: 0.0

☐ Origin Coordinates

Start

Figure 3.6: Starting a new Job in FaceProfiler

To do face profiling, a reflector flag was utilised as part of the equipment along with a tripod-mounted TruPulse 200 laser rangefinder as shown in Figure 3.7 (B) and (C). The TruPulse 200 laser rangefinder was set at 10 m from the rock face of the blast to ensure a clear view, with the reflector flag placed at the first row of the drill holes. Subsequently, the laser was pointed and shot in the direction of the crest where the reflector flag point was placed while a second point was taken at the toe of the bench to determine the bench height. This was followed by a scaled plot of the face on the FaceProfiler, which showed the profile details. Afterwards, meticulous shots were taken at regular intervals to capture the changes in the bench face while working from the crest down to the toe of the bench.

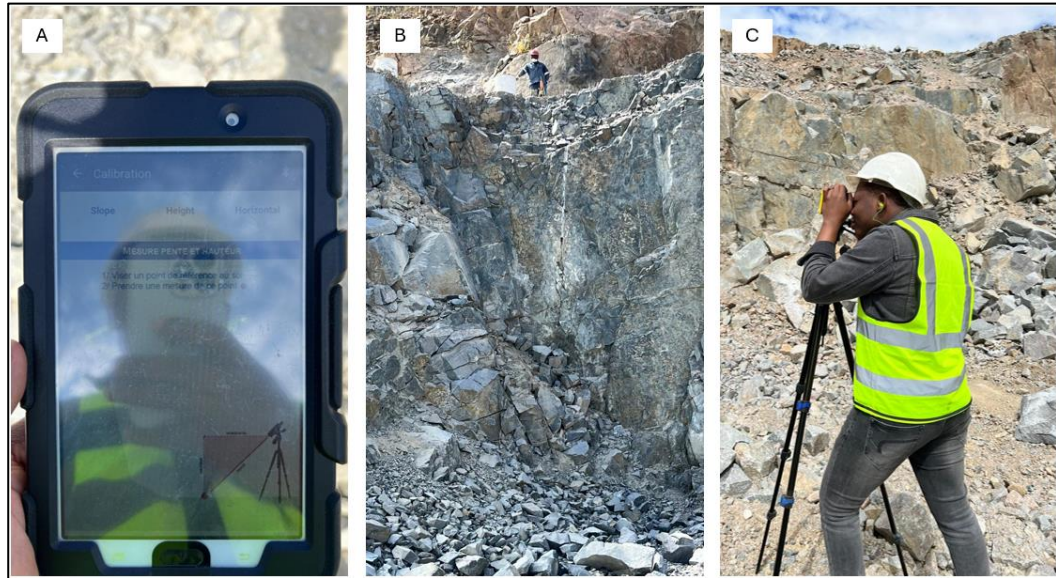


Figure 3.7: (A) Samsung device; (B) Reflector flag and (C) Setup used in face profiling surveys (Source: Author's own picture)

To create a thorough profile, around 12 measurements were needed at various points on the bench face as shown in Figure 3.8. This procedure was repeated for each of the front drill holes in a bench. The program captured the data and created a CSV file, which was then utilised by the I-Blast program to determine the appropriate angle of the drill holes in areas where that was required.

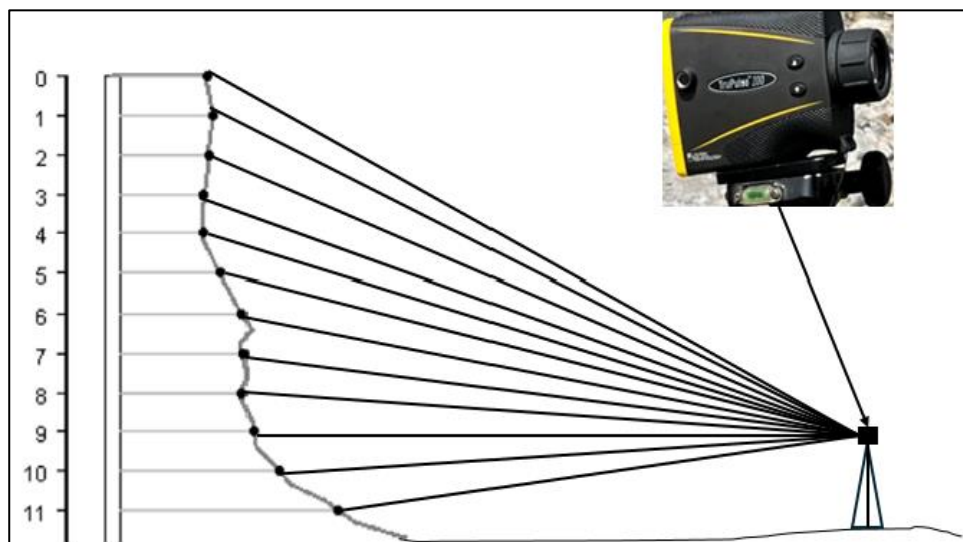


Figure 3.8: Illustrating the use of the TruPulse 200 Laser Profiler for bench face profiling

In some cases, especially in regions with irregular geology, angled blastholes were necessary to maximize fragmentation, reduce backbreak, and improve breakage efficiency. Angled holes at 5° were used in some holes for blasts #2, #4, and #5. These modifications were made in accordance with site-specific conditions, ensuring controlled muck pile displacement and optimal energy distribution.

3.3.4. Blast design setup

Effective blast design should ensure both safety and operational efficiency. During the design process, the I-Blast 8.2 software was used to create the required front row drill angles and delay timing sequences. These parameters are both critical for attaining the necessary fragmentation while reducing ground vibration, flyrock, and boulders.

The blast design process began with the creation of a new project within the I-Blast 8.2 program (see Figure 3.9). This initial phase provided a structured framework within which all subsequent design activities could be organized and executed.

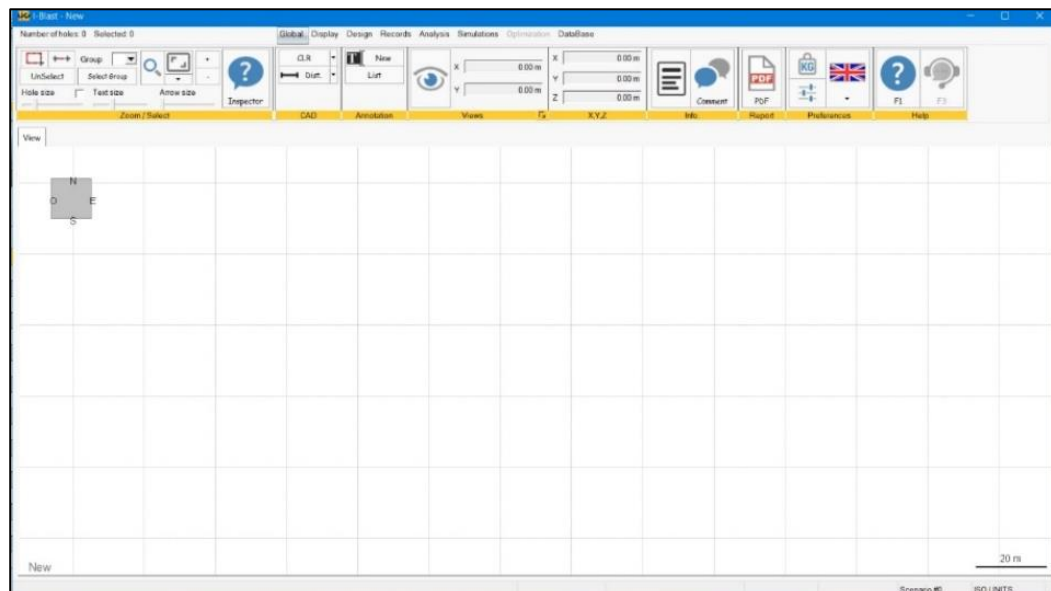


Figure 3.9: Starting a new design in I-Blast

To work efficiently with the data, the CSV file created in Section 3.3.2, which contained the exact locations of drill holes, was loaded into the program. Figure 3.10 depicts how the CSV file was imported into the I-Blast environment. The transaction then enabled the exact placing of drill holes inside the blast design (see Figure 3.11). This configuration formed the basis for the subsequent design work, which allowed for the exact control over the blast settings selected for each test.

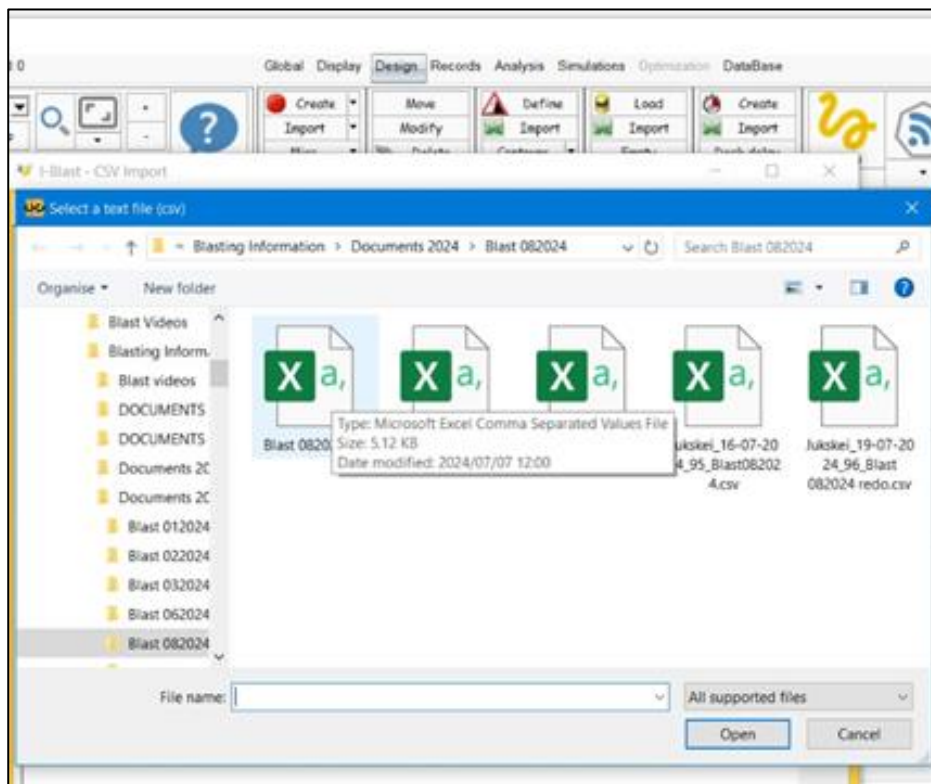


Figure 3.10: Importing the drill hole pattern created from the Trimble TSC3 controller into the I-Blast software

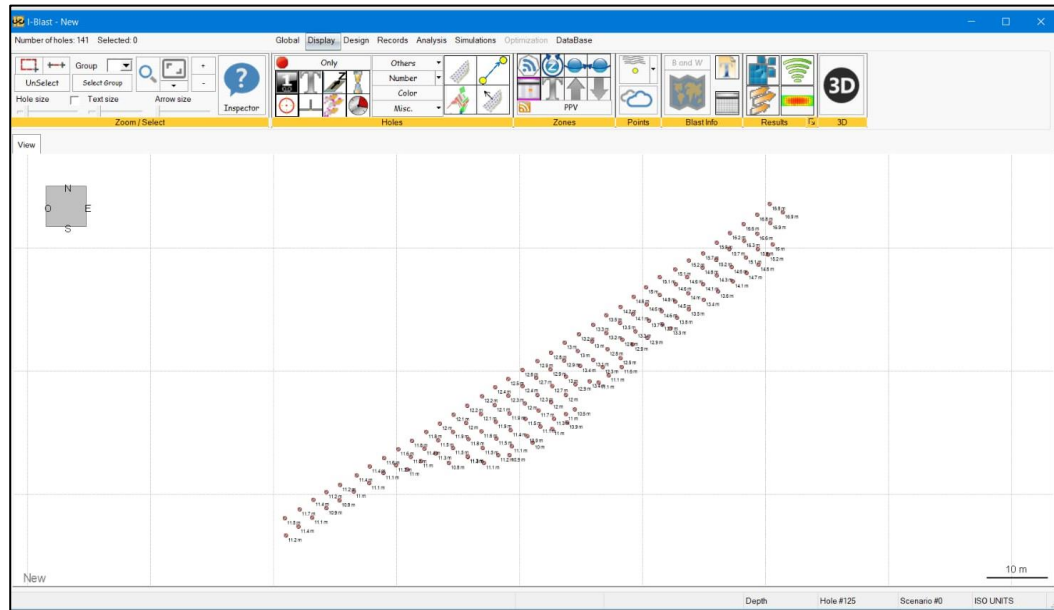


Figure 3.11: Example of drill hole positions imported into the I-Blast software

3.3.4.1. Creating a drilling depth pattern

After importing the drill hole positions, the next step was to establish the drilling depth pattern for all drilling holes. While creating a drilling pattern using I-Blast may appear simple, obtaining accuracy necessitates close attention to detail and input parameters. This was done by going to the analysis section of the I-Blast program. Once there, the drilling pattern module was accessed which enabled input parameters such as 1 442.00 m grade elevation level and subdrill depth 0.5 m to be entered as shown in Figure 3.12. These parameters were critical because they directly affect the accuracy of the drill hole depths over the entire blast pattern.

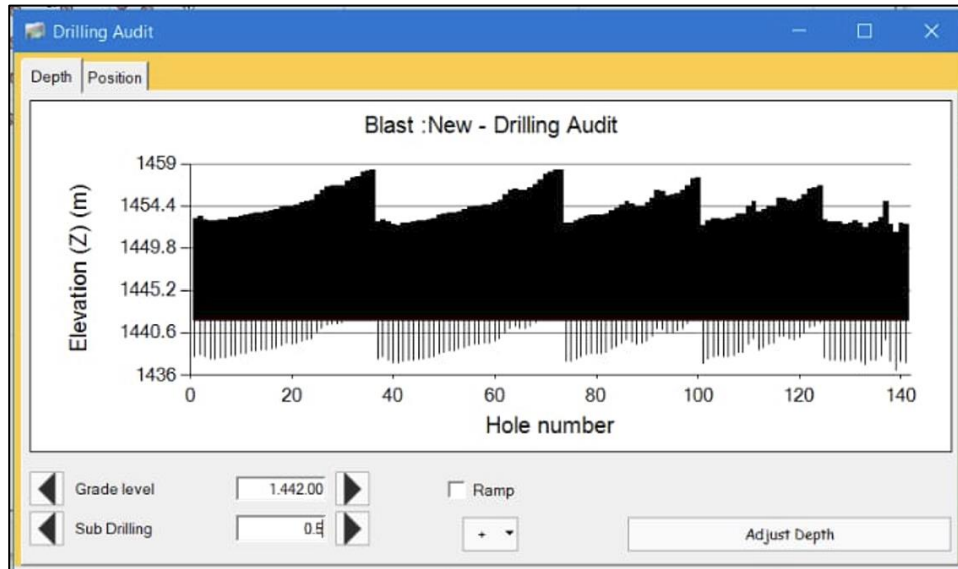


Figure 3.12: Identification of the drill hole depth

After entering these parameters (i.e., grade level and subdrilling length), the drill hole depth was adjusted throughout the pattern. The system subsequently generated the exact drill depths for the entire pattern thereby maintaining consistency and accuracy across the designed bench. The ability of the I-Blast software to compute and adjust drilling depths based on the provided parameters ensured that the blast design aligned with the specific requirements of the site.

Following this, the next process covered in Section 3.3.4.2, was to design the drill hole angles using the data obtained earlier in Section 3.3.3.

3.3.4.2. *Design angles for the front row drills*

The design process adopted for the front row drill angles begins with the selection of the front holes based on the firing sequence. As shown in Figure 3.13, this is to ensure that the relevant information is assigned to the appropriate drill holes. Figure 3.13 shows the selection of drill holes that required an appropriately designed angle. The entire front row, which runs diagonally from bottom left to top right, is meant to be the focus of adjustments. The red-highlighted holes, on the other hand, are those chosen for analysis at this point. The process of assigning the correct design

was still in progress, which is why only a few holes are highlighted. When finished, the complete design will incorporate every hole in the front row.

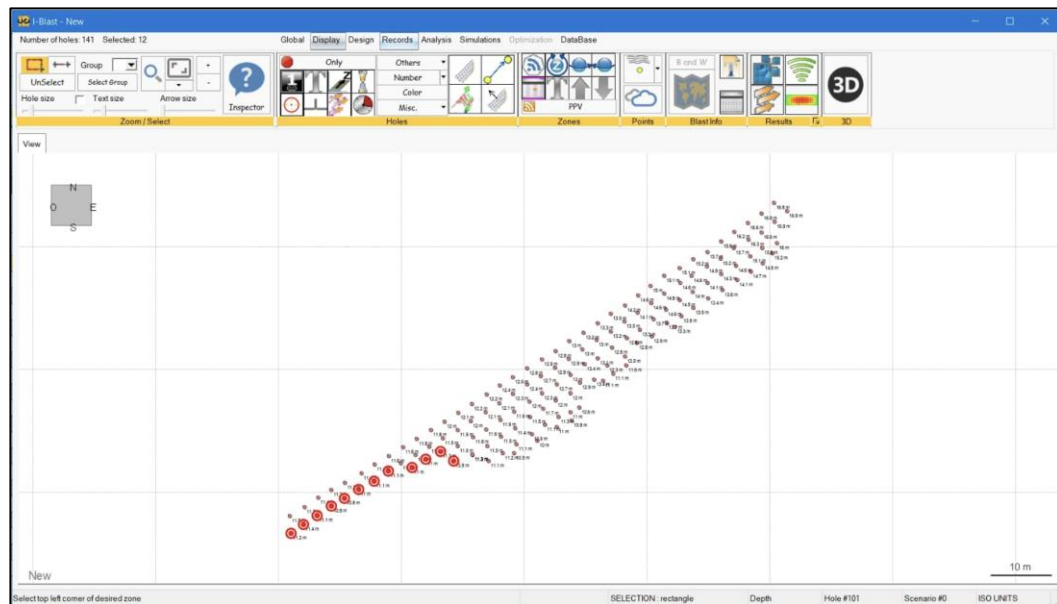


Figure 3.13: Design configuration for the front row angle

Once the holes were selected, the “records” button of the program was launched, and the 2D profile function was selected as displayed in Figure 3.14(1). Within the 2D profile interface, the LYNX face profile type was selected, allowing one to load the survey data from Section 3.3.3 into each designated drill hole as exemplified in Figure 3.14(2).

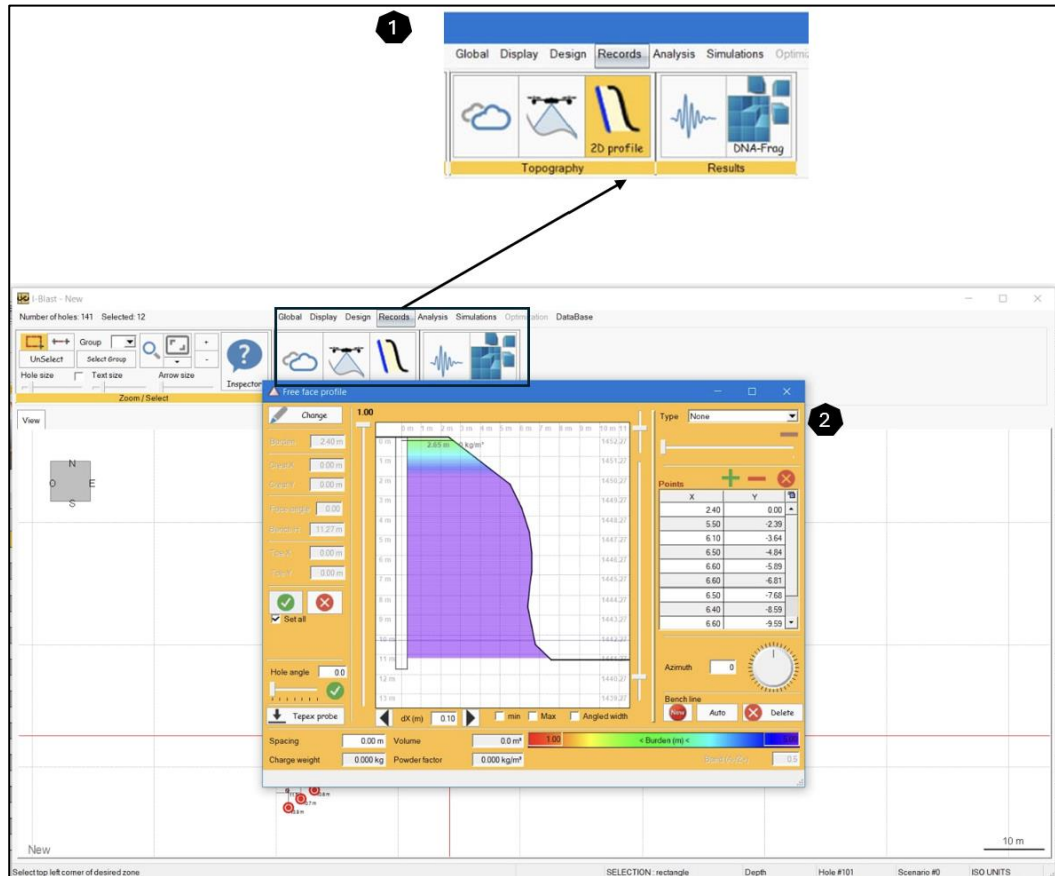


Figure 3.14: (1) – Drill hole design function and (2) – 2D profile dialogue box

After loading the profiles, the next step was to use the inspector tool and select the bench function. This then displayed the profiles of the bench face for confirmation as shown in Figure 3.15B. Based on the face profile view, any changes in connection with the drill hole angle was made under the details function of the inspector interface view as shown in Figure 3.15A.

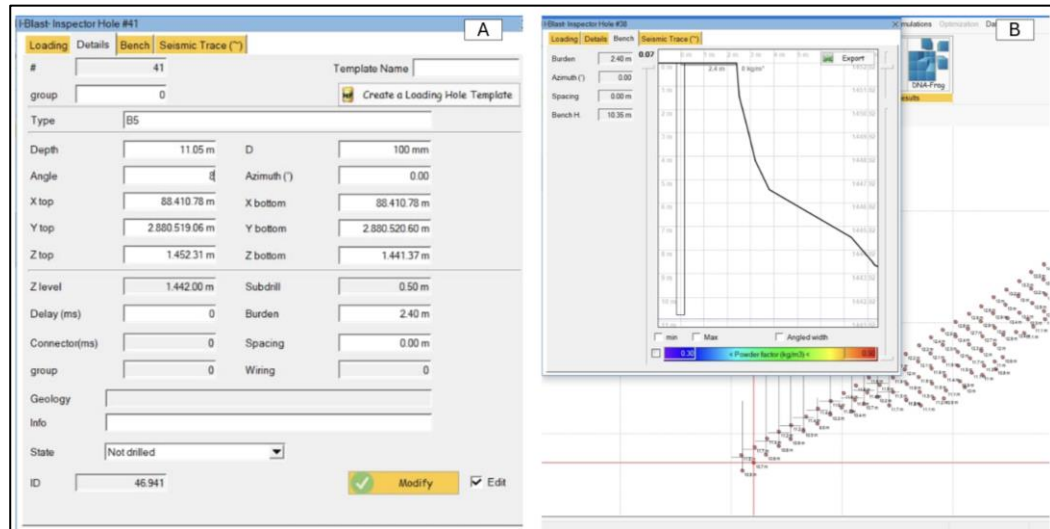


Figure 3.15: A – Display of the drill hole details and B – Profile of the face of the drilled bench

3.3.4.3. Design of the delay timing intervals

Designing delay timings in I-Blast software involves a structured approach to ensure precise control over the blast sequence. The process commenced with loading the blast holes with explosives. The load function was activated through the design menu icon where the load option was selected to determine the proper loading settings. Note that S200 eco AEL was chosen as the proper explosive material before the blast holes could be charged. Figure 3.16 displays the loading dialogue window where the precise explosive material was selected based on the blasting requirements and design characteristics.

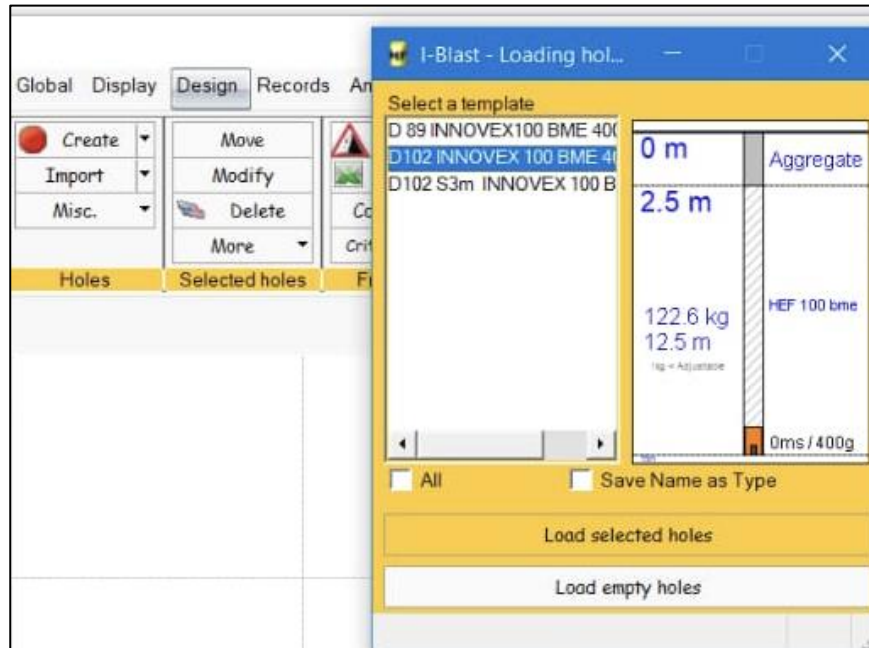


Figure 3.16: Loading of blast hole with explosives

After successfully loading the explosives into the blast holes, the delay time setup followed. The step started with selecting the appropriate type of surface delay element and the wiring method that were used. This was accomplished by using the design menu item to access the surface delay wiring dialogue shown in Figure 3.17. Upon selecting the surface delay function, the inter-hole delays for the experimental blasts #1, #2, and #3 were inputted as 17 ms, 9 ms, and 6 ms respectively (see Figure 3.17).

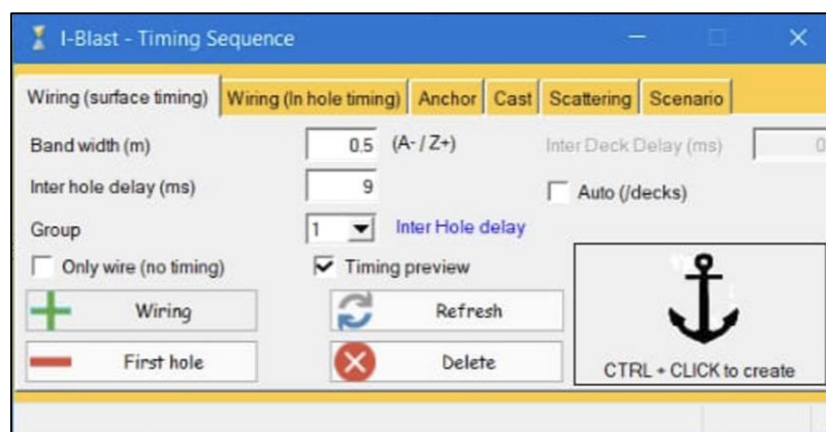


Figure 3.17: Entering the input data pertaining to the surface delay wiring

After entering the inter-hole delay parameters, the blast holes were then wired. This was achieved by selecting each blast hole and connecting it to

the adjacent hole as illustrated by the blue lines in Figure 3.18. The wiring process began at the free face with careful attention to the fact that the face had to be wired first. The inter-row timing connections were then established, proceeding systematically from one hole to the next. This sequential approach was maintained until the entire blast layout was fully wired for a coherent and efficient detonation sequence across the entire blast area.

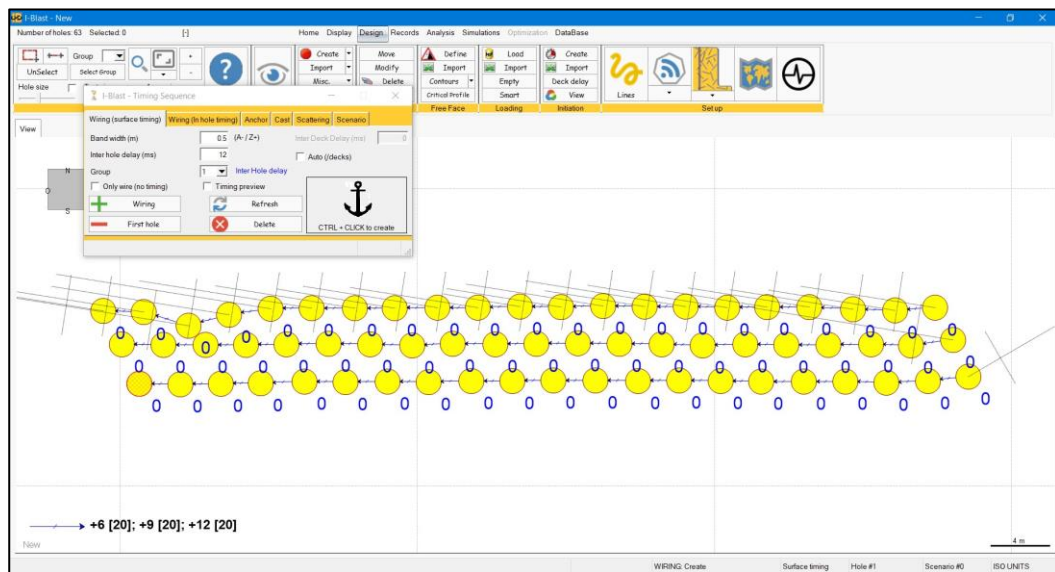


Figure 3.18: Example of blast holes charged with explosives and their corresponding wired inter-hole delays

Lastly, the timing sequence window depicted in Figure 3.19 was used to set the inter-row delays. In this window, the Group value was set to 2, allowing the inter-row delay timing to be configured. The next step was to set the inter-row delay field for this group to 23 ms, a value that was used consistently for all experimental blasts. After this configuration, the wiring process moved forward by connecting the blast holes sequentially beginning at the first point of initiation and ending at the last blast hole.

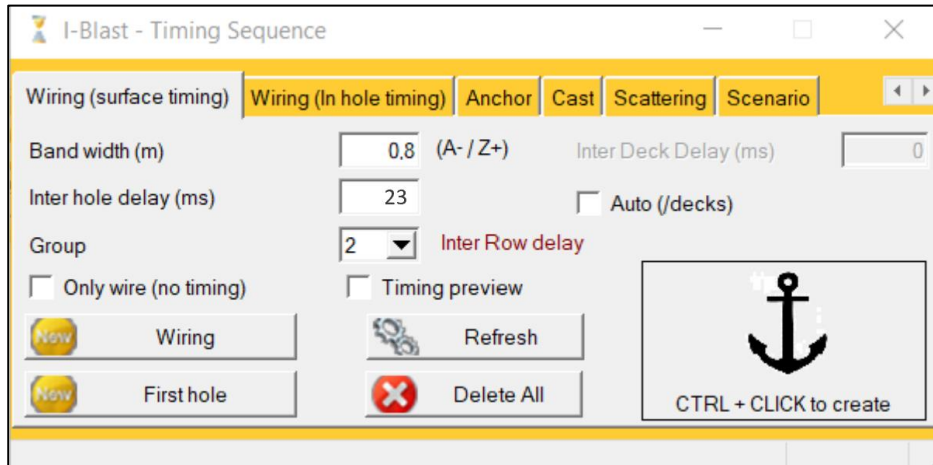


Figure 3.19: Inter-row delay timing configuration

The entire Section 3.3.4 was conducted using computational methods due to the complexity and precision required in analysing the data. Large datasets could be processed quickly and effectively with the use of a computer thereby ensuring accuracy and consistency in the output. This method was required to take into consideration variables that were not suitable for manual measurement or effective control. Computational tools also made it possible to simulate different scenarios and forecast possible outcomes, which strengthened the analysis.

In the following section, the focus returns to on-site events where actual measurements and observations were made in practice.

3.3.5. Preparing a primer and priming each blasthole

Blasthole priming is the process of preparing the blasthole for detonation. This process involves inserting an explosive cartridge, usually referred to as a primer, into the blasthole. The specific model used in this instance was the AXXIS GII designed with advanced electronic timing features. Manufactured by BME company, the AXXIS GII detonator is renowned for its precision, reliability, and ability to ensure safe and accurate blasting. Its properties also include enhanced resistance to electrostatic discharge and high induced ground currents which ensure greater safety across diverse mining environments.

The detonator is connected to a C-400 booster (400 g) to form a unit referred to as a primer. The C-400 booster is characterised by its red and conical shape. It is specifically designed to provide cost-effective initiation in large diameter holes exceeding 150 mm. Each primer was carefully lowered into the blastholes until it reached the proper depth as illustrated in Figure 3.20.



Figure 3.20: Priming of a blast hole – The typical red C-400 booster used in the various blast tests is shown on the top right with the yellow wire holding the AXXIS GII detonator (Source: Author's own picture)

Following this priming step is the charging of the blastholes, which is detailed in the subsequent subsection.

3.3.6. Charging of blastholes

Explosives were used to charge the blastholes. The type of explosives used was the INNOVEX 100 emulsion which is standard for this quarry. The INNOVEX 100 emulsion is also manufactured and supplied by BME, a South African based company specialising in blasting consumables, accessories and instruments.

The INNOVEX 100 emulsion features a minimum initiation requirement of a 150 g booster when sensitized for holes with a diameter of 127 mm or less. It also has a variable velocity of detonation (VOD) ranging from 3 500 m/s

to 5 500 m/s depending on the hole and the rock characteristics. Additionally, the INNOVEX 100 emulsion has a relative weight strength (RWS) of 84%, making it a robust choice for various blasting applications (BME, 2023).

Figure 3.21 illustrates the emulsion-containing truck connected to a charging pipe used to pump emulsion into blastholes. Pumping was done until the desired mass of explosives was reached to allow clearance for stemming.



Figure 3.21: An explosive truck with emulsion and blast hole charging
(Source: Author's own picture)

Table 3.3 presents the charging sheet used to load the first row of blastholes for blast #1 with emulsion. The amount of emulsion pumped was determined based on the 102 mm hole diameter, the blast hole length, the stemming length required, and the emulsion density of 1.5 g/cm³.

Table 3.3: Sheet used during the emulsion pumping of some of the blast holes prepared for blast #1

Hole number	metres	Planned kg	Actual kg
A1	15.8	163	166
A2	15.3	157	160
A3	14.5	147	160
A4	15.6	161	165
A5	15.3	157	160
A6	15.2	156	165
A7	15.0	153	160
A8	15.0	153	165
A9	14.8	151	165
A10	15.8	163	165
A11	14.9	152	160
A12	14.9	152	165

The weightometer installed on the explosive truck was used to determine the precise volume of explosives to be charged into the hole. The blasthole was not fully charged to the top; a column was left below the collar for stemming. Stemming length was then measured with a tape and referred to as first stemming. This is because gassing had not occurred yet. When measuring the first stemming, any excess emulsion found was sucked from the blast hole using a PVC pipe until the required column was obtained (see Figure 3.22).



Figure 3.22: Excessive emulsion sucked out of the blastholes using a PVC pipe (Source: Author's own picture)

3.3.7. Stemming of blastholes

Hand shovels and buckets were used during the stemming process. Each hole was left open for a period of time before stemming could commence. This was done to allow emulsion to expand as part of the gassing process. Gassing is necessary to bring the emulsion density down into the explosible range. Explosible range refers to the specific conditions under which an explosive material can effectively detonate and produce the desired effects (Fan et al., 2016).

In order to monitor whether gassing was taking place, 150 ml cups were pumped with emulsion during the charging of the drilled holes as illustrated in Figure 3.23. The cup density which is the density of the explosive pumped into the cup is measured. This was done during the pumping of explosives thereby allowing one to monitor gassing while charging the blast. The minimum gassing time allowed for the whole bench was 30 min, but the actual gassing time varied depending on the temperature of the day. This is because temperature impacts gassing time. Indeed, higher temperatures

accelerate chemical reactions which then reduce the required gassing time. In contrast, lower temperatures slow down these reactions, necessitating a longer gassing period.

Figure 3.23 shows the cup that was used to measure the density of explosives. It weighed 225 g at the standard density of 1.5 g/cm³ before gassing. After gassing, the foamed protruding over the cup was removed and the cup was weighed again at approximately 180 g with a calculated density of 1.2 g/cm³. This showed that the emulsion was mixed properly and was within the explosible range for the blast. This also indicated that gas bubbles were appropriately introduced into the explosive column as an essential feature for sensitizing the emulsion and ensuring effective blasting performance.



Figure 3.23: Weighing of the standard cup of emulsion before and after gassing (Source: Author's own picture)

After confirming the gassing process, the next step was to remeasure the stemming column and ensure that it was within the required length (Figure 3.24B). In cases where the stemming differed slightly from the planned length, excess emulsion was removed from the hole as depicted in Figure

3.22. Equally, when the stemming length was significantly greater than intended, additional emulsion was injected to achieve the planned stemming length which was then referred to as final stemming. The final stemming is what was used as a blast design parameter later in the fragmentation analysis done in Chapter 4.



Figure 3.24: Stemming process – (A) Tamping and stemming; (B) Taking measurements after gassing using a tape measure (Source: Author's own picture)

Afterwards, the process of stemming took place, which was then followed by the tamping of the stemming material. Tamping involved the consolidation of the stemming material within the blast hole to ensure a tight fit as shown in Figure 3.24A.

3.3.8. Connecting and tagging the cables for electronic detonators

The electronic detonators used in this study were AXXIS detonators. These detonators are attached to an intelligent connector (or tag). The purpose of a tag is to programme and assign a firing value to each detonator. Following the steps in Figure 3.25, each blast was connected as follows:

1. Before connecting, each AXXIS detonator cord was visually examined to check whether there was any physical damage.

2. After the visual inspection, the detonator was programmed through a process known as logging. During logging, one hand was used to bring the tag into contact with the AXXIS logger as depicted in Figure 3.25(4). Logging was conducted to obtain a unique identification number (i.e., the PIN number) for programming and subsequently firing the detonator. Failure of the detonator to register on the tagger would indicate potential damage.
3. The electronic tag, which contained a separator, was open as in Figure 3.25(1). The separator was then removed from the tag, and wires were connected to it as shown in Figure 3.25(2).
4. Finally, the tag was closed, ensuring that the wires were securely connected as illustrated in Figure 3.25(3).

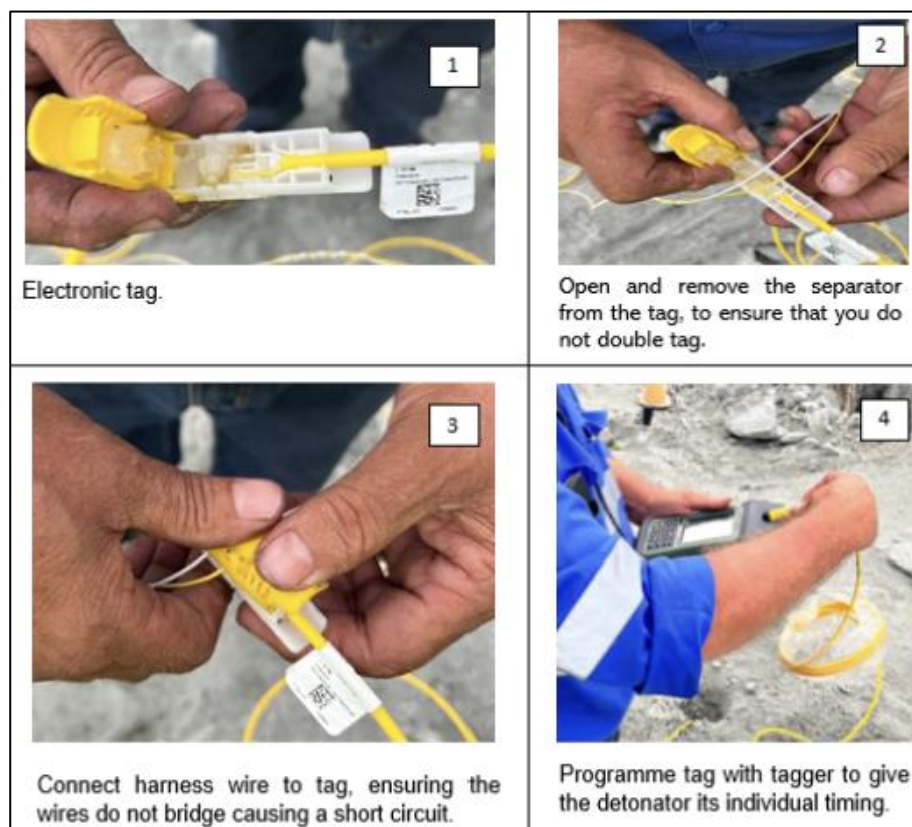


Figure 3.25: Procedures followed when attaching detonator cords (Source: Author's own picture)

In this process, the input data outlined in Section 3.3.4 is essential. In particular, the recorded data was used to program each detonator with the

necessary firing values. This programming ensured optimal sequencing during the blast by precisely allocating timing delays to individual detonators according to the design parameters. Throughout this process, every detonator was tagged and logged in a systematic manner, and detailed records were maintained to ensure accuracy and traceability. This made it possible for the blast to be executed and coordinated precisely. Figure 3.25 highlighted how these programmed values were assigned to guarantee alignment with the overall objectives of the blast.

3.3.9. Detonating the charge

During the investigation, the AXXIS digital initiation system comprising multiple blasting boxes was utilised. In this research study, one box was set as the master blasting box while the another was linked as the slave box (see Figure 3.26). Once the wiring and logging tasks was completed, the data recorded in the tagger containing the unique identification number (i.e., PIN number) and the firing time was transferred to the slave box and later to the master box.

The slave box (i.e., Figure 3.26A) was positioned in the quarry at a distance where it could detect the connected detonators on the production bench and, at the same time, maintain communication with the master box (Figure 3.26C). When properly positioned, the slave box was then linked to the master box located under the blast shelter shown in Figure 3.26C. Thereafter, a system check was conducted to verify communication between the slave box and the master box (see Figure 3.26B). This was done by testing signal transmission between the master and slave boxes to confirm reliable communication and operational readiness.



Figure 3.26: (A) Remote slave box; (B) Blaster verifying the blast connections; and (C) Remote master initiating box (Source: Author's own picture)

Another verification was conducted to ensure that all detonators are recognised and configured correctly within the system. Once all checks and verifications were completed, the blast was ready to be initiated. The blasting siren was activated to alert individuals in the vicinity of the production bench to take necessary safety precautions. Following this, a countdown from 10 ensued until the initiation button was pressed to trigger the blast.

3.3.10. Video recordings

Video recordings of the blasts were captured throughout the investigation using a Nikon COOLPIX B500 camera mounted on a tripod as shown in Figure 3.27. This camera typically records video at 7.4 frames per second (fps) for a maximum resolution of 4 608 x 3 456 pixels. The camera features a BSI-CMOS sensor, a sensor photodetector of 17 megapixels, and various shooting modes suitable for different conditions.

To ensure optimal video quality, the camera was positioned in an area with adequate lighting. By carefully positioning the camera relative to the sun, clear videos were captured. These video recordings served as an important documentation of the complete blasting process. The detailed analysis of such videos is covered later in Chapter 4.



Figure 3.27: Configuration and setting up of the blasting camera (Source: Author's own picture)

The detonation sequence of the production bench is depicted in Figure 3.28. Once the blaster confirmed the status of all detonators, the PIN number generated by the slave box was entered shortly before the designated blasting time. With all necessary checks completed as explained in Section 3.3.9, the blast was initiated by simultaneously pressing the two firing buttons shown in Figure 3.28(1). The projection of the resulting muckpile is depicted in Figure 3.28(3) while Figure 3.28(2) showcases the initial blast position. Before returning to the production bench after the detonation, a waiting period of 30 min was observed to allow for the dissipation of fumes shown in Figure 3.28(4).

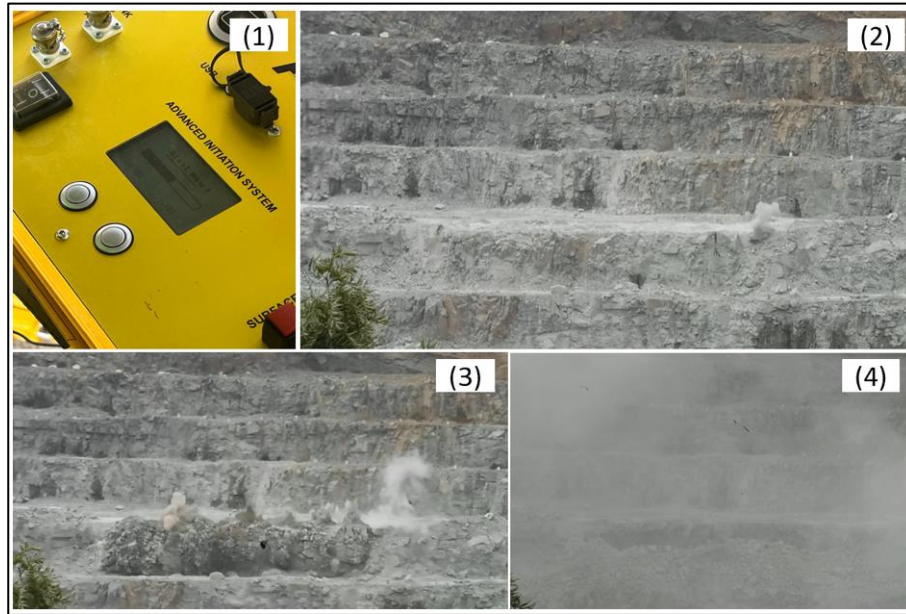


Figure 3.28: View of the detonation sequence of the production bench
(Source: Author's own picture)

It is important to note that each video recording proved to be valuable in the following ways:

- It documented the entire process of blast setup including timing, initiation, and the resulting effects of the blast.
- It provided visual evidence of the safety practices implemented during the blasting operation.
- It facilitated the study and evaluation of the effectiveness of stemming in containing the explosives.

3.3.11. Blast vibration monitoring

Monitoring of ground vibration and airblast were conducted at two specific locations: the quarry lookout points and the primary crusher. The measuring instruments used were categorized based on their placement. The first instrument, named VIBRO 1, was positioned at the quarry viewpoint. The second instrument, labelled VIBRO 2, was placed around the primary crusher as depicted in Figure 3.29. This enabled a clear differentiation between the two locations.



Figure 3.29: Location of the two vibrometers used for the blast trials
(Source: Picture supplied by the quarry)

Given that the quarry is surrounded by residential and industrial infrastructures, it was critical to keep an eye on the vibration levels and make sure they did not result in any form of damage to existing infrastructure. As such, ground vibrations were continuously monitored for each blasting event. The Nomis Mini Supergraph seismograph in Figure 3.30, manufactured by Nomis Seismographs company, was employed for the purpose.



Figure 3.30: The two Nomis Mini Supergraph seismographs used on site to monitor ground vibrations and airblast (Source: Author's own picture)

The Mini Supergraph model is equipped with a tri-axial geophone and an

air overpressure microphone, making it capable of accurately recording both ground vibrations and airblast. It features a 16-bit resolution sensor for enhanced data accuracy and is capable of capturing vibration frequencies ranging from 2 Hz to 400 Hz. The device also has a maximum sampling rate of 1 024 samples per second, ensuring high-resolution data acquisition.

The ground vibration data captured was saved on the Nomis seismograph. After each blast, the raw data was transferred to a computer for safekeeping. The data was later analysed using a specialist software that Nomis Seismographs provides as part of the suite. Primary parameters were derived from the data including the peak particle velocity (PPV) and the frequency of the ground vibration. The magnitude and frequency of the air blast were also computed as is later shown in Chapter 4. Every entry was classified as summarised in Table 3.4 based on the precise blast event, the recording time, and the entry point in relation to the blast site.

Table 3.4: Overview of the structure of the blast vibration monitoring data (peak particle velocity and frequency ranges) collected

Vibro location	Blast no.	Particle velocity			Frequency		
		Radial	Transverse	Vertical	Radial	Transverse	Vertical
Primary Crusher	n.	(mm/s)	(mm/s)	(mm/s)	(Hz)	(Hz)	(Hz)
Quarry viewpoint	n.	(mm/s)	(mm/s)	(mm/s)	(Hz)	(Hz)	(Hz)

Standardized measurement units are specified in Table 3.4 as a clear point of reference for data interpretation. This structured format made it easier to evaluate ground vibrations as later reported in Chapter 4.

3.3.12. Collection of crusher throughput data

The final data collected as part of this research study was about the throughput of the primary crusher. The main objective of gathering this data was to examine the connection between rock fragmentation and crusher

throughput. For this reason, real-time data that included feed size distribution and throughput rates was gathered on the operation of the crusher. The weightometers shown in Figure 3.31 and installed below the crusher as well as associated conveyor systems were used to collect this data. These weightometers specifically recorded the feed rate to and the discharge rate from the crusher.



Figure 3.31: Snapshots of the weightometers located in the control room and at the conveyor belt discharge point (Source: Author's own picture)

The material entering the crusher was digitally photographed in order to record the feed size distribution. The particle size distribution of the feed material was then established by analysing these pictures using the WipFrag software available on site. An iPhone 13 Pro served as the camera with high-resolution digital devices strategically placed near the crusher feed area to record images of truckloads emptying material into the crusher. The throughput data from the weightometers and this photographic information were combined to evaluate the connection between feed size distribution and crusher performance.

Figure 3.32 provides an overview of the aggregate crushing process with the primary crusher in open circuit discharging onto the intermediate stockpile (ISP). The quarry is focused on meeting a daily production target of 3 000 t at the jaw crusher within a single eight-hour shift.

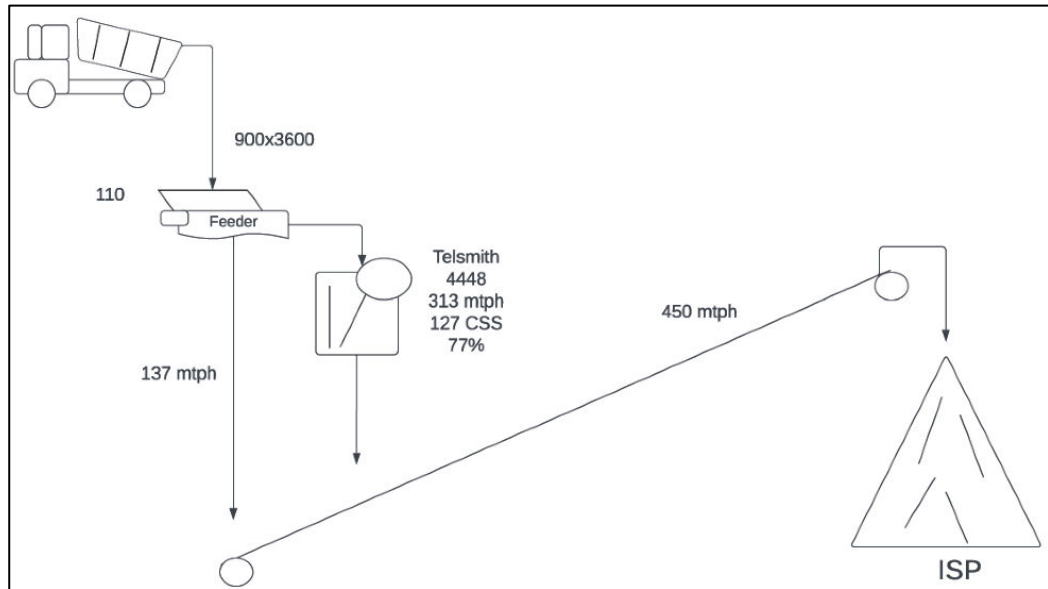


Figure 3.32: Flow diagram of the primary crushing of the aggregate run-of-mine with the closed side setting (CSS) of 127 mm feeding onto the Intermediate Stockpile (ISP)

The quarry uses a Pegson Telsmith D type 44 x 48 jaw crusher, which has a capacity of between 272 and 758 tons per hour (tph). But it is currently set to operate at 350 tph. This jaw crusher is designed to have a closed side setting (CSS) between 125 mm and 300 mm, with a maximum feed size of 1 100 mm. However, the quarry has adjusted the acceptable feed size to 450 mm. Figure 3.33 illustrates the CSS of a crusher alongside the real-life image of the primary jaw crusher on site. The CSS was kept at 127 mm to guarantee the collection of meaningful and high-quality material at the crusher. This was done to control the quality of the data even though high throughput can be achieved by increasing CSS (Rosario, 2003).

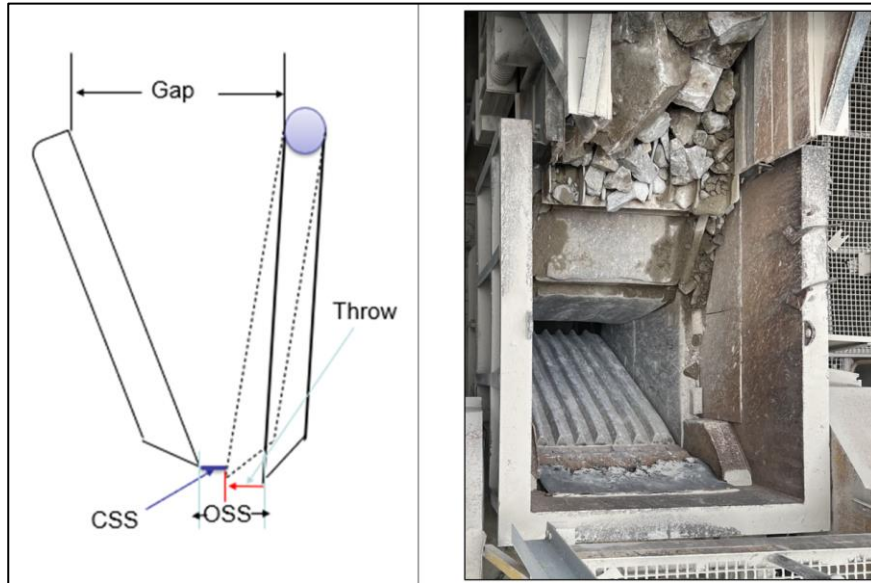


Figure 3.33: Diagram of a jaw crusher with key design and operating parameters – OSS is the open side setting of the crusher while CSS refers to its closed side setting

Finally, it should be noted that prior to each production shift, the CSS measurements were taken to ensure uniformity for each blast test. The required modifications were then made using these measurements to preserve the intended CCS of 127 mm.

3.4. Data evaluation

In this section, the impact of the changes made to the blast design was assessed by data assessment, rock fragmentation, and crusher throughput study. This approach provided a full understanding of the blast design impact on rock fragmentation and crusher performance. The specific details of this approach are outlined in the following subsections.

3.4.1. Rock fragmentation analysis

The primary goal of blasting is to break the rock to the required fragment size. However, it is difficult to evaluate the degree of fragmentation. In terms of this research study, image analysis techniques were employed for the

purpose.

After each blast, still photographs of the muckpile were processed by image analysis using the WipFrag software. WipFrag can produce an automated image-based granulometry from the digital image of a muckpile (Maerz et al., 1996). The utilisation of the WipFrag software involved several steps. Initially, relevant images were imported from a laptop into the WipFrag software as shown in Figure 3.34(a). After the images were uploaded, a hardhat measuring 290 mm in length was positioned on the muckpile to serve as a scale reference, see Figure 3.34(f). On the other hand, the width measured across the tailgate of the feed truck served as another reference point as indicated in Figure 3.34(b).

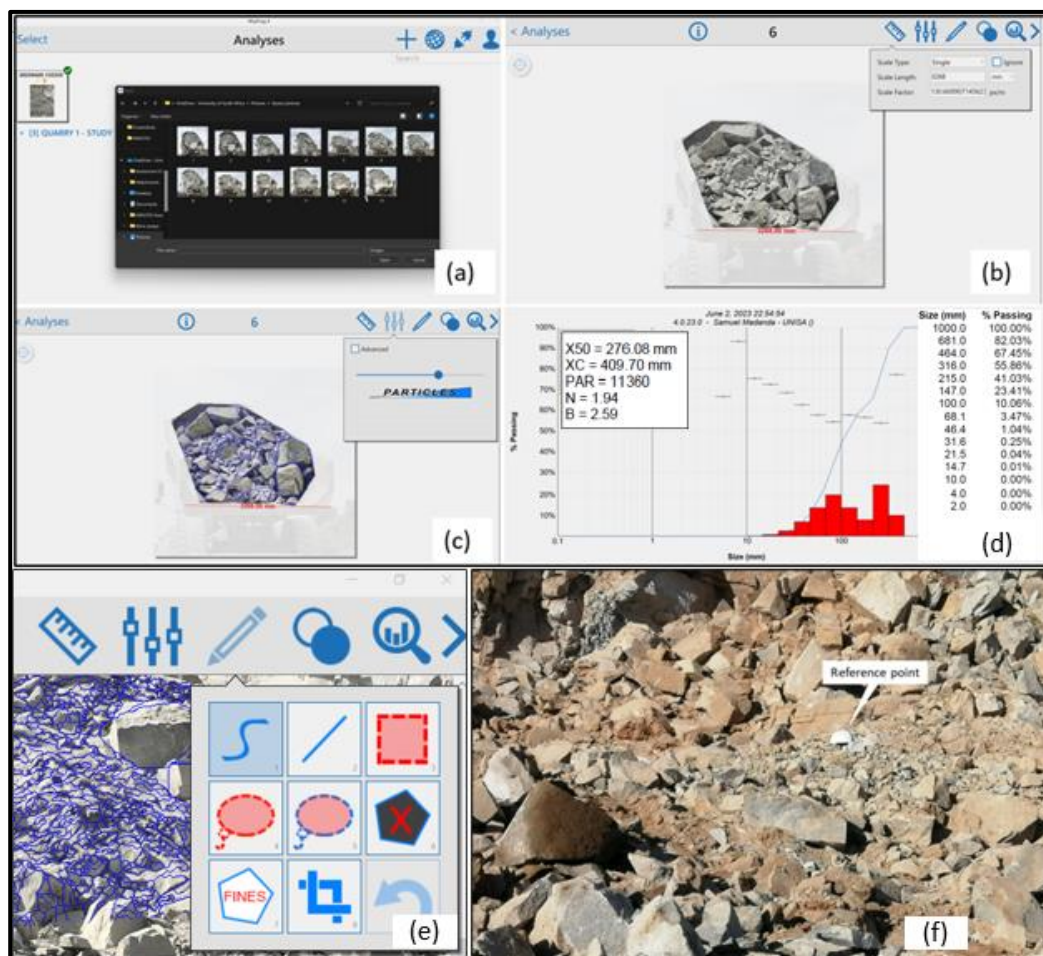


Figure 3.34: Procedure followed to analyse fragmentation using the WipFrag software

Subsequent steps included applying edge detection parameters to automatically outline and delineate fragments within the image. The edge detection parameters were adjusted by means of the advance particle slider in Figure 3.34(c). To refine the edge detection accuracy, manual editing was employed using specific tools that allowed adjustments to the blue net as illustrated in Figure 3.34(e). The final step in the process was the preparation of the size distribution output for reporting. This was done to produce the graphical representation and the chart statistics of the muckpile size distribution as depicted in Figure 3.34(d).

3.4.2. Analysis of the throughput of the crusher

The analysis of crusher throughput was carried out using a systematic methodology that closely resembles the process used to measure rock fragmentation on the muckpile (refer to Section 3.4.1 above). The analysis began by taking photographs of the feed material from the truck before it is tipped into the crusher. These still photographs were analysed with WipFrag as displayed in Figure 3.35.



Figure 3.35: Image-based monitoring of the truck feed fragmentation at the quarry (Source: Author's own picture)

The performance of the primary crusher was evaluated in the context of its ability to handle varying sizes of material to a maximum of 450 mm. To determine the relationship between rock fragmentation and crusher throughput, a statistical regression analysis was performed in combination with empirical modelling. The analysis considered two important metrics: the mean fragmentation size and the variance on the size of the feed material. The effects of these two metrics on the efficiency and throughput of the primary crusher were then established. Finally, feed uniformity and operating downtime occurrences were interrogated for an overall view of the performance of the primary crusher. Results are presented in two next two chapters.

3.5. Limitations and challenges encountered

The primary limitation of the investigation was a restricted number of blasts. The quarry only allowed trial blasts that would not disrupt normal production operations, which led to this restriction. This is the main reason why only six experimental blasts could be executed.

Second, the only feasible approach available in the quarry was the indirect image-based measurement of rock fragmentation. Direct techniques could not be used as they would have disrupted production, despite their perceived superiority in terms of precision (Cho et al., 2003).

Third, strict vibration limitations were imposed on the investigation to reduce the possibility of damage to infrastructure and nearby structures. These restrictions hindered the investigation of more aggressive blasting procedures that may have produced alternative insights. It was therefore not possible to freely explore the blast design beyond what was tested, especially regarding timing and explosive intensity.

Fourth, the uniaxial compressive strength (UCS) and Young's modulus of the rock mass used in this study came from historical testing done at the quarry. Therefore, the subsequent results might be affected as the

information may not have adequately reflected the state and characteristics of the presently uncovered rock.

Lastly, the fragmentation model used subsequently in the study did not account for the delay timing for the blast. By neglecting to include timing in the fragmentation model, the study might have overlooked crucial elements that affect the blast overall effectiveness.

Chapter 4: Effects of stemming length and inter-hole delay on rock fragmentation

This chapter presents a comprehensive assessment of blasting performance by combining historical data, field observations, statistical analysis, and empirical modelling. While field measurements provided useful insights into operational effectiveness, historical blasting performance enabled the creation of a standard for comparison. Experimental blasting tests, on the other hand, provided the necessary controlled data that enabled the assessment of the impact of both stemming length and inter-hole delay timing. Statistical analysis was used to highlight trends, variations, and correlations. And lastly, in terms of fragmentation analysis, the Kuz-Ram and the KCO models were tested for their adequacy to be used as predictive tools at the quarry.

4.1. Introduction

Six blast trials were conducted with focus on two variable parameters (i.e., stemming length and delay timing) with other blast design parameters kept constant. This was to isolate their effects on blast fragmentation and crushing performance.

The experimental process began with an examination of each blast area including the bench terrain and highwall face. This step provided insights into the geological structure to ensure a suitable blast design. The bench was then staked (refer to Figure 3.4 in Chapter 3) with a GPS Trimble system to precisely determine the location and depth of each drilled hole. Additionally, a face profile was employed to identify areas that needed angled drilling and mitigate possible problems of fragmentation.

Post-blast, the muckpile size distribution was analysed using the WipFrag software. Furthermore, blast video recordings and ground vibration data were analysed to assess the safety compliance of the six blasts carried out.

Details of the results obtained from the endeavour are presented in the subsequent sections.

4.2. Historical blasting performance

4.2.1. Review of historical results

The historical blasting data used in this study includes parameters from three distinct blasts designated blast no. 0122, 0622, and 0223. Results summarised in Table 4.1 show a gradual improvement in performance, particularly with reduced boulders across blast no. 0122, 0622, and 0223 (Internal Quarry Document, 2022 – 2023).

Table 4.1 also highlights that the occurrence of boulders decreased significantly from 30% in blast no. 0122 to 15% in blast no. 0223. This is likely due to adjustments in delay timings and stemming length.

Table 4.1: Overview of historical blast reports showing various parameters

Blasting parameters	Blast no. 0122	Blast no. 0622	Blast no. 0223
Type of explosive	Emulsion	Emulsion	Emulsion
Burden	2.5 m	2.5 m	2.5 m
Spacing	2.8 m	2.8 m	2.8 m
Average hole depth	13.9 m	14.3 m	14.4 m
Hole diameter	102 mm	102 mm	102 mm
Inter-hole delay timing	25 ms	17 ms	17 ms
Inter-row delay timing	42 ms	42 ms	23 ms
Blast pattern	Staggered	Staggered	Staggered
Final stemming length	2.8 m	2.7 m	2.5 m
Size of stemming material	10 mm	10 mm	10 mm
Mass fraction of boulders (visual estimation)	30%	20%	15%

While key parameters such as type of explosive (emulsion), burden, spacing, hole diameter, and stemming material remained constant, changes

in inter-hole and inter-row delay timings were notable. The inter-hole delay was reduced from 25 ms in blast no. 0122 to 17 ms in blast no. 0622 and blast no. 0223. The inter-row delay was further decreased to 23 ms in blast no. 0223. Moreover, the final stemming length decreased slightly across the blasts from 2.8 m in blast no. 0122 to 2.5 m in blast no. 0223. This may also have improved energy confinement thereby contributing to better fragmentation. The use of a consistent staggered blast pattern further supported these results. Overall, these adjustments led to a marked improvement in fragmentation with blast no. 0223 achieving the best outcome. It is argued that further optimisation on delay timing and stemming length could enhance performance and efficiency even more.

4.2.2. Assessment of safety compliance of historical blasts

The historical seismograph data recorded for the three blasts in Table 4.1 were examined. The ground vibration results are shown in Table 4.2 from two different vibrio locations (i.e., the quarry viewpoint and the primary crusher). The radial, transverse, and vertical components of the particle velocities are reported along with corresponding frequencies.

Table 4.2: Historical seismographic results taken from the quarry viewpoint and the primary crusher

Vibrio location	Blast no.	Particle velocity (mm/s)			Frequency (Hz)		
		Radial	Transverse	Vertical	Radial	Transverse	Vertical
Primary Crusher	0122	7.976	4.470	4.343	34.10	64.00	39.30
	0622	9.271	4.267	5.944	17.60	36.50	36.50
	0223	2.515	3.124	3.023	15.50	16.50	18.20
Quarry viewpoint	0122	1.270	0.279	0.330	85.00	102.40	170.60
	0622	2.692	2.001	1.930	23.20	36.50	21.30
	0223	5.791	3.937	4.293	30.10	46.5	23.20

The primary crusher had significantly higher radial velocities; the highest radial velocity, 9.271 mm/s, was recorded for blast no. 0622. The frequency range for this location was between 15.50 Hz and 64 Hz, with transverse frequencies typically being higher. In comparison, the quarry viewpoint showed lower velocities where for example the radial velocity peaked at 5.791 mm/s for blast no. 0223. The quarry viewpoint had much higher frequencies, particularly for vertical components, with a peak of 170.60 Hz during blast no. 0122. According to these findings, the quarry viewpoint generally exhibited more noticeable vertical frequencies whereas the primary crusher experienced high radial vibration velocities. Additionally, the recorded ground vibrations met the safe limit requirements established by the United States Bureau of Mines (USBM) and the OSM as shown in Figure 4.1. Indeed, the PPVs recorded for all blasts were below 12.7 mm/s. This is the USBM safe limit criteria that the quarry has adopted when assessing seismograph readings.

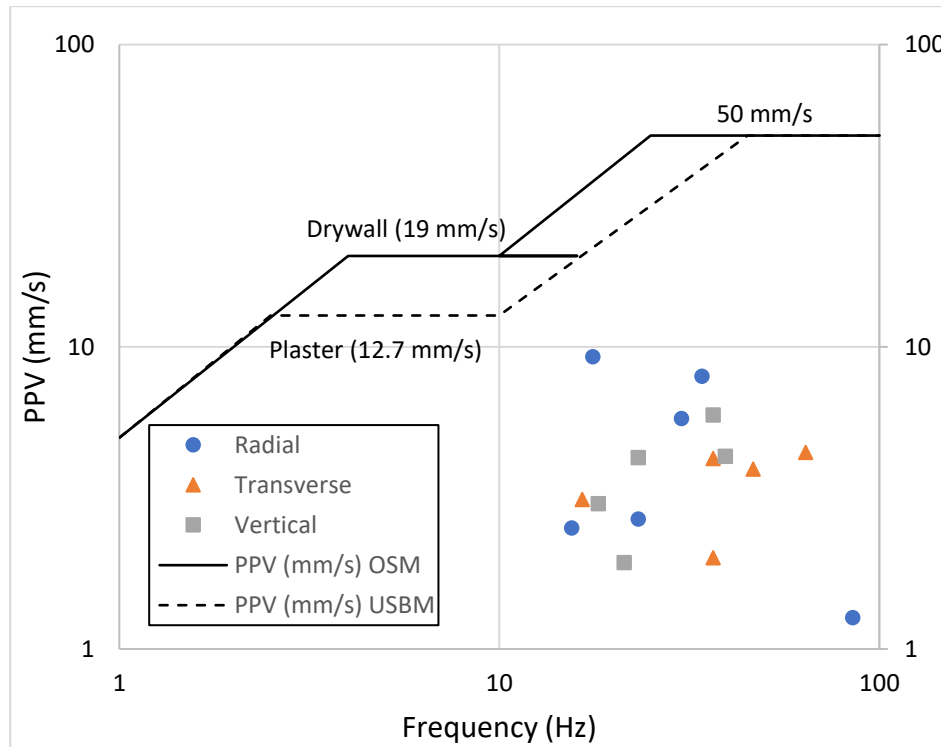


Figure 4.1: Safety limits for ground-born vibrations from historical blasting as established by USBM and OSM

4.3. Field observation and measurement

The six trial blasts carried out during the investigation period represented the basis for field observations. Assessing the terrain and geological discontinuities of each blast bench was the first step in the observation process. Section 4.3.1 provides a detailed presentation of the qualitative observations. And in terms of bench face profiling, relevant results are covered in Section 4.3.2.

4.3.1. Blast bench face and terrain conditions

Visual inspections were carried out on both the terrain and the face of the bench for the 6 trial blasts. The inspections were explicitly centred on the geological conditions of the trial blasts as well the geomechanical characterisation of rock mass.

Singh et al. (2015) stated that rock fragmentation is influenced by rock mass properties as an uncontrollable variable. However, in the context of the present research study, observations made in term of rock mass properties was aimed at assisting in the optimisation of the blast design. To this end, the condition of the bench terrain for blast #1 resulting from the observation is used for illustration. It can be seen in Figure 4.2 (A) that the bench terrain was relatively flat with minimal loose material. Upon assessing the condition of the bench terrain condition, a Global Positioning System (GPS) was used after staking to precisely determine the depth and position of each blast hole. This method was systematically applied to all the blasts as detailed earlier in Section 3.3.2. Observations of the terrain for blasts #2, #3, #4 and #5 showed specific patterns including minimal loose material along the top and edge of the crest as can be seen in Figure 4.2. In addition to this, uneven surfaces and high spots that also comprised some loose material along the edge were observed.

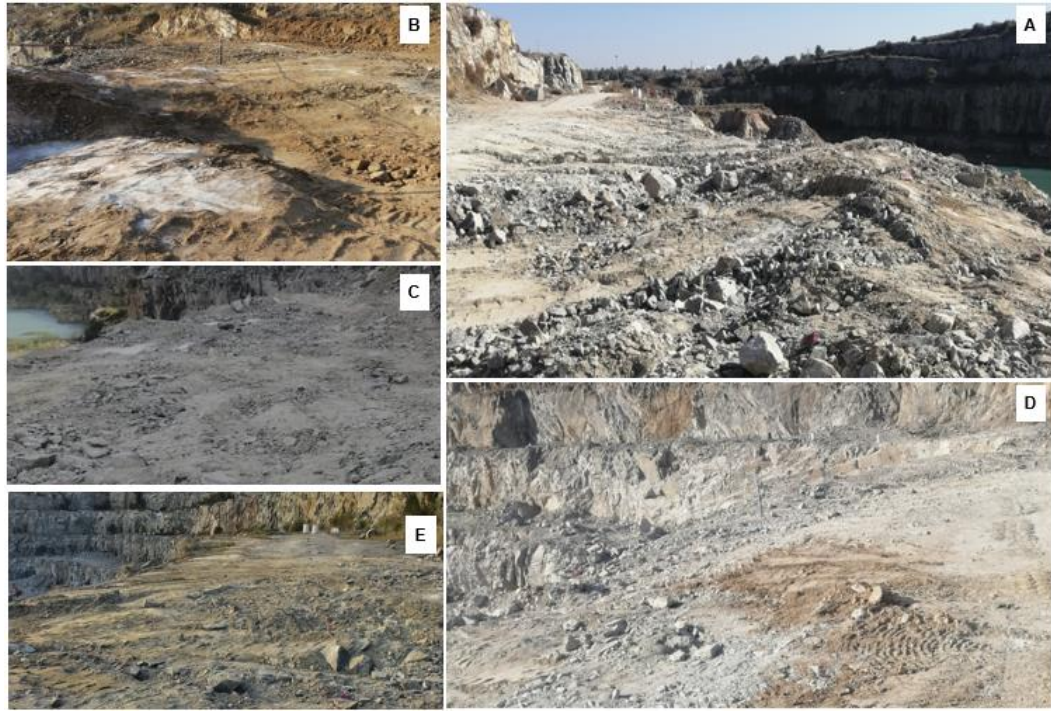


Figure 4.2: A – Bench terrain for blast #1; B – Bench terrain for blast #3; C – Bench terrain for blast #2; D – Bench terrain for blast #4; and E – Bench terrain for blast #5

The distinct geological conditions associated with each blast were identified by additional observations and measurements of the geological discontinuities on the benches. Appendix A provides more details on this in terms of joint plane spacing (*JPS*), joint plane angle (*JPA*), hardness factor (*HF*), rock density influence (*RDI*), and rock mass description (*RMD*). Suffice it to say here that the in-situ granite rock has a density of 2.72 t/m³, a Young's modulus of 70 GPa, and a Uniaxial Compressive Strength of 235 MPa (Internal Quarry Document, 2022 – 2023). In addition to this, the following should be noted: $20 \text{ m} \leq JPS \leq 50 \text{ m}$; $20^\circ \leq JPA \leq 40^\circ$; $HF = 47$; $RDI = 18$; $20 \leq RMD \leq 50$; and $40 \leq JF \leq 90$.

The above results were later used to characterise the blastability index of the rock mass following the summary provided in Table 2.1 of the literature review.

Likewise, visual inspection of the geological condition of the highwall was conducted. Figure 4.3 illustrates the geological condition of the highwall

corresponding to blast #2. It is in this case characterised of horizontal and vertical joints, weathered areas, blocky structure and some brittle zones near the bench crest. Appendix B at the end of the dissertation documents all the inspections conducted during the study.

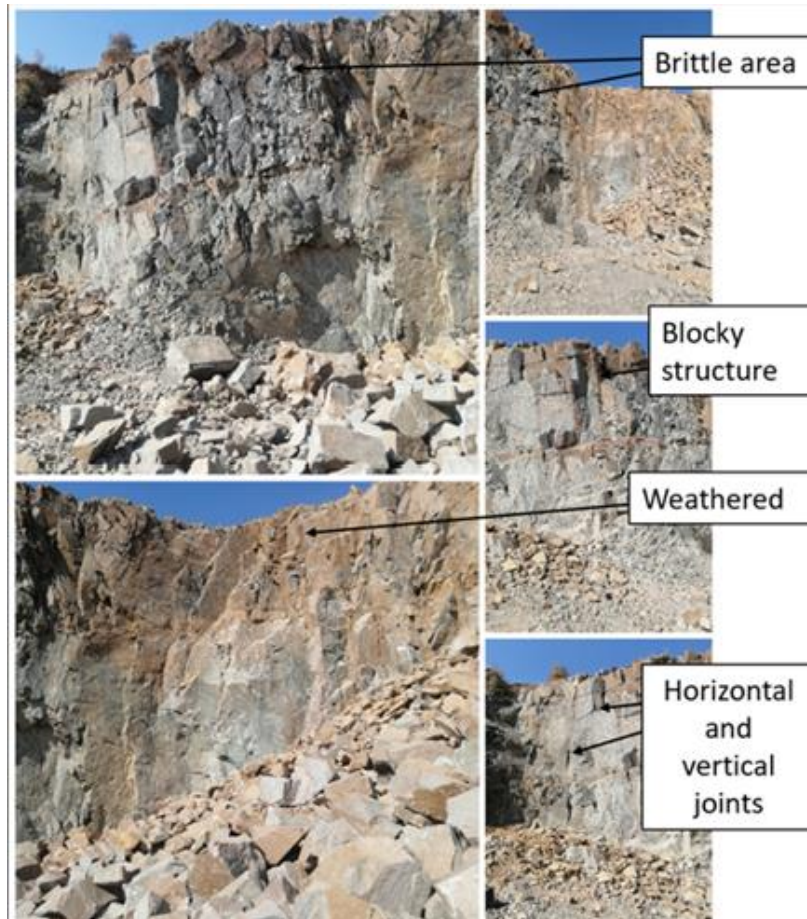


Figure 4.3: Observed features of the bench face for blast #2 with key geological characteristics

4.3.2. Measurements taken during surveys to profile rock faces

The bench face of the blasting area was profiled through the blast highwall. The surveyed measurements were conducted on the first rows of the blast layout; they are indicated by the vertical lines in Figure 4.4. These measurements taken during the survey yielded important information about the profile of the rock face. They enabled one to ascertain whether the rock face had excessive burden or there was toe protrusion and/or protrusion at

the crest of the bench. This information assisted in optimising the blast design for enhanced safety yielding minimal flyrock and ensuring that the structural integrity of the blast area is maintained. A detailed procedure employed on face profiling is outlined in Section 3.3.3.

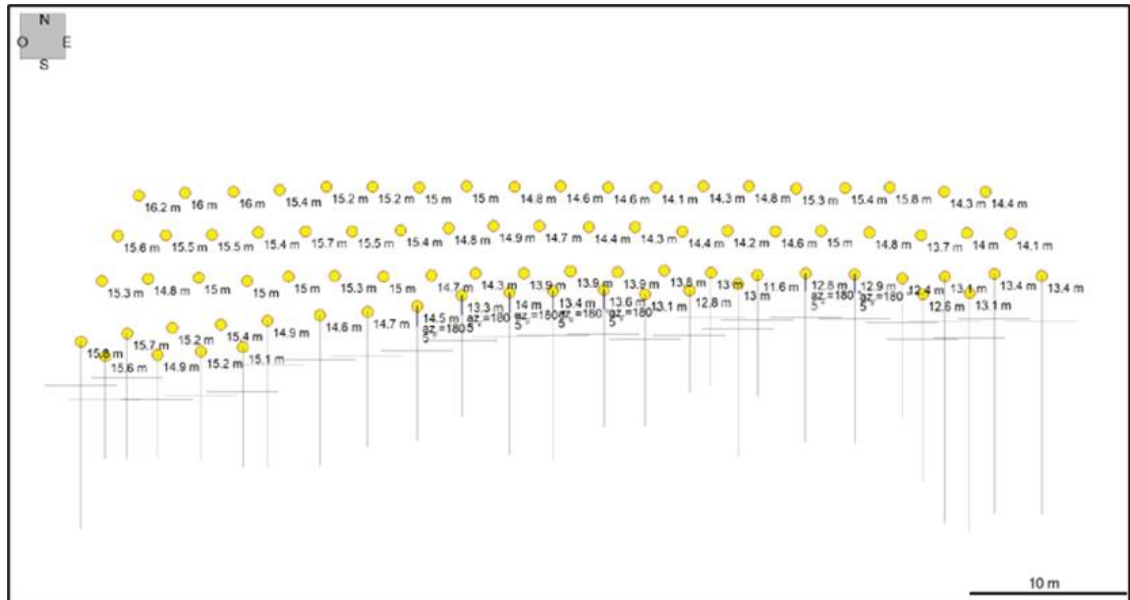


Figure 4.4: Drilling pattern with hole depths and angles for blast #2

In terms of results, the bench faces blasts #2, #4 and #5 indicated an excessive burden that necessitated the use of angled hole drilling at a 5° inclination. Figure 4.5 illustrated this for blast #2 where some drill holes were designed at an angular orientation. On the other hand, blasts #1 and #3 displayed no protrusion; as a result, the use of angled hole was deemed impractical. In this case then, all drill holes were designed at a right angle relative to the horizontal plane of the bench.

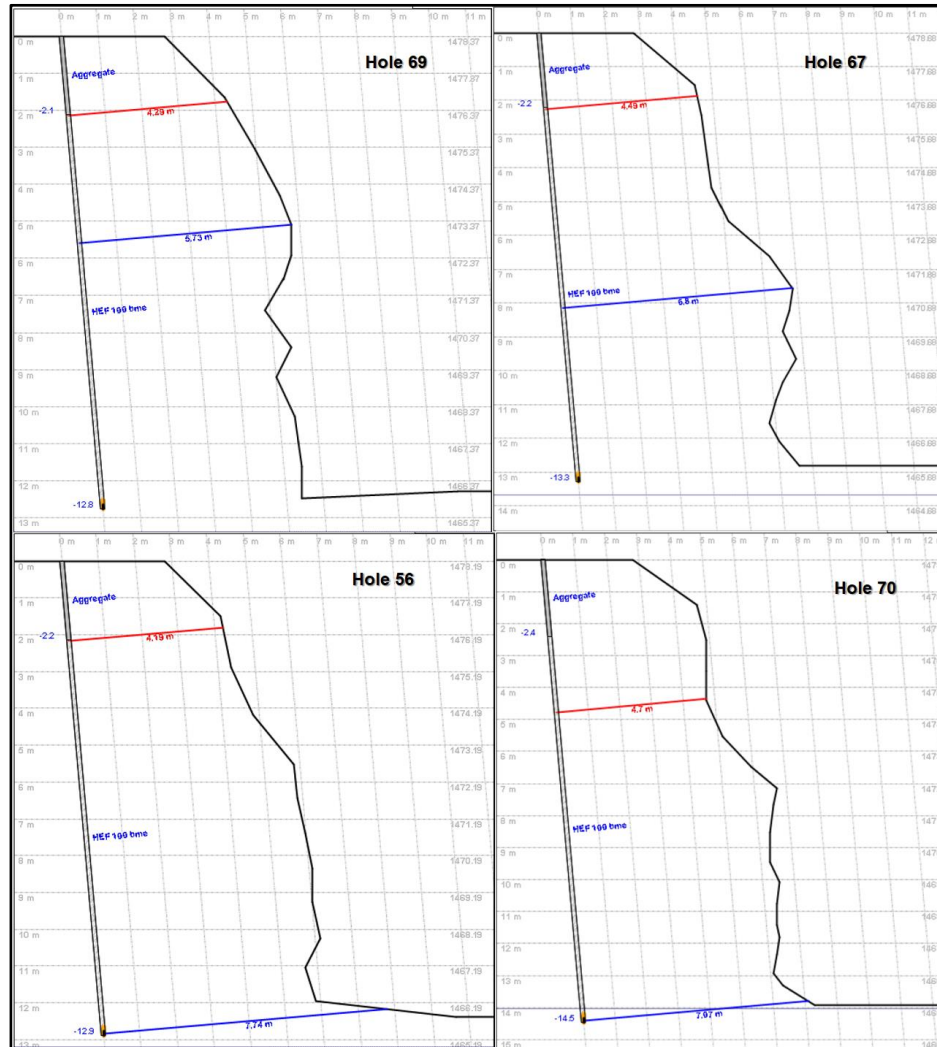


Figure 4.5: Surveyed face profiling showing excessive burden on holes 69, 67, 56 and 70 for blast #2

4.4. Experimental blast results

The study involved the observation and analysis of the performance of six experimental blasts conducted within the set timeframe. These blasts were numbered in sequential order based on their occurrence. Table 4.3 outlines the design details as well as essential parameters that were employed during the study. The primary focus of these trials was to investigate the effects of both stemming length and inter-hole delay timing on rock fragmentation. The results of the scientific enquiry are presented in this section.

Table 4.3: Summary of blast design parameters for the experimental study

Blast no.	Blast #1	Blast #2	Blast #3	Blast #4	Blast #5	Blast #6
Date	23-Feb-2023	28-Mar-2023	04-Apr-2023	15-Jun-2023	29-Jun-2023	11-Jul-2023
Type of explosive	Emulsion	Emulsion	Emulsion	Emulsion	Emulsion	Emulsion
Burden (m)	2.5	2.5	2.5	2.5	2.5	2.5
Spacing (m)	2.8	2.8	2.8	2.8	2.8	2.8
Bench height (m)	14.5	14.5	14	14	11	12.5
Average hole depth (m)	15	15	14.5	14.5	11.5	13
Hole diameter (mm)	102	102	102	102	102	102
No. of holes	69	81	47	57	118	88
Inter-hole delay timing (ms)	17	9	6	6	6	6
Inter-row delay timing (ms)	23	23	23	23	23	23
Blast pattern	Staggered	Staggered	Staggered	Staggered	Staggered	Staggered
Final stemming length (m)	2.5	2.5	2.5	2	1.5	1
Powder factor (kg/m ³)	1.15	1.70	1.44	1.29	1.20	1.17
Size of stemming material (mm)	10	10	10	10	10	10

4.4.1. Effects of stemming length on rock fragmentation

Six blasts were carried out during this experimental investigation, as was previously mentioned. Three of the blasts were fundamental to investigating the impact of stemming length on rock fragmentation. These blasts were blast #4, blast #5, and blast #6.

Following the gassing procedure detailed in Section 3.2.2, the final stemming lengths were measured and are presented in Table 4.3. The actual field measurements following the gassing process are displayed in Appendix C. A stemming length of 2 m was recorded for blast #4. Blast #5 used a 1.5 m stemming length while blast #6 employed a 1-m stemming length. The WipFrag software was then used to investigate how the parameter affected rock fragmentation. Details of the methodology are described earlier in Section 3.4.1. But in terms of fragmentation analysis, Figure 4.6 presents the muckpile image from blast #4 with a reference point. The established reference point used was a safety hardhat with a length of 290 mm. This reference point was employed for post-blast analysis and incorporated into the image analysis with the WipFrag software. Given the extensive length of the muckpile, all the blasts were each divided into distinct sections to enhance the accuracy of the fragmentation analysis.



Figure 4.6: Muckpile produced from blast #4 with a safety hardhat used as a 290 mm wide reference point

Figure 4.7 shows the results from the WipFrag-based image analysis of the muckpile of blast #4. The particle size distribution is plotted as a bar chart of the mass fraction of material retained on different screen sizes. The cumulative size distribution can also be seen plotted alongside in the form of a line chart.

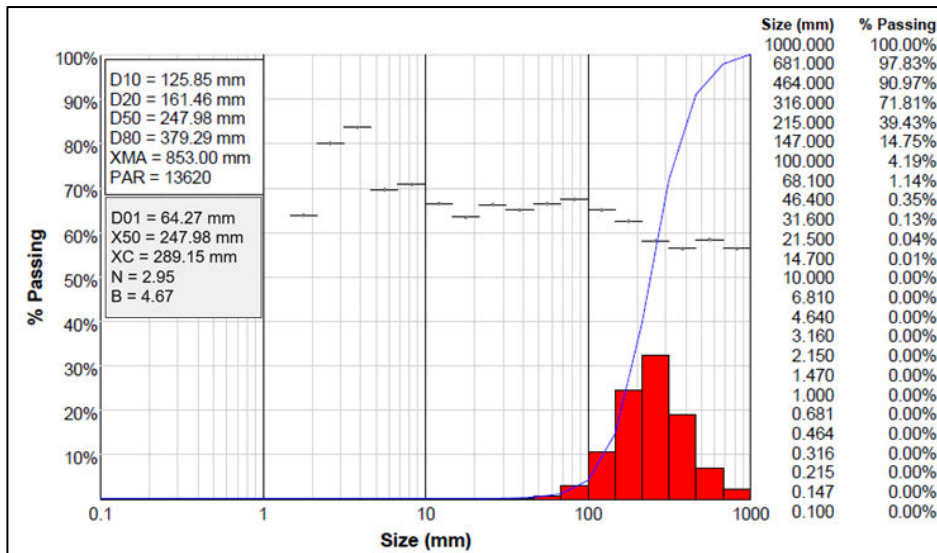


Figure 4.7: Fragmentation analysis report for blast #4 generated with the WipFrag software

The overlain line chart in Figure 4.7 highlights that 20% of material falls below size $D_{20} = 161.46$ mm while the average size of fragments in the muckpile is $X_{50} = 247.96$ mm. The 80% passing size is $D_{80} = 379.29$ mm. The software also reveals that a total of 13 620 particles (PAR) was processed with a largest being $X_{max} = 853$ mm. The following parameters descriptive of the size distribution are provided based on Equations (2.7) and (2.9): the undulation index $b = 4.76$; the Rosin-Rammler characteristic size $X_c = 289.15$ mm; and the Robin-Rammler uniformity index $n = 2.95$.

The image analysis of blast #6 processed 21 017 particles with $X_{max} = 826$ mm and $X_{50} = 212.97$ mm. Conversely, the results for blast #5 reported the largest particle processed of size $X_{max} = 865$ mm from a total (PAR) of 13 941 particles analysed. Detailed results for both blasts are summarised in Table 4.4. This comparative analysis illustrates significant variations in particle size distribution across the three blasts.

Table 4.4: Characteristics of the muckpile size distributions corresponding to blasts #4, #5, and #6

Wipfrag outputs	Blast #4	Blast #5	Blast #6
D01	64.27 mm	63.76 mm	112.77 mm
D20	161.46 mm	93.59 mm	149.84
D80	379.29 mm	402.13 mm	382.40mm
PAR	13620	13941	21017
X_{max}	853 mm	865 mm	826 mm
X_{50}	247.96 mm	236.45 mm	212.97 mm
X_c	289.15 mm	290.65 mm	282.7 mm
n	2.95	2.02	2.66
b	4.67	2.31	4.27

The actual mass fractions of passing material associated with each blast are listed in Table 4.5. These figures provide a means for comparing quantitatively the relative performance of all three blasts. They equally show relative variations in particle size distributions across blasts. Blasts #4 and #6 share the fact that their corresponding muckpiles contain large fragments of size around 1 000 mm. In contrast, the largest fragments for blast #5 are around 681 mm. This suggests that the blasting process successfully shrivelled the largest material to sizes that could be handled by the loading equipment. But as the particle sizes get smaller, the mass fraction of material that passes through finer sizes varies greatly from one blast to another testament of the different blasting conditions tested.

Table 4.5: Cumulative particle size distributions for blasts #4, #5 and #6

Size (mm)	Mass fraction passing (%)		
	Blast #4	Blast #5	Blast #6
1000	100.00	100.00%	100.00
681	97.83	99.89%	97.18
464	80.97	88.99%	88.90
316	61.81	67.48%	72.70

215	39.43	50.43%	43.88
147	14.75	36.08%	18.96
100	4.19	22.17%	6.66
68	1.14	11.39%	2.11
46	0.35	4.44%	0.61
31	0.13	1.48%	0.05
21	0.04	0.41%	0.24
14	0.01	0.09%	0.01
10	0.00	0.03%	0.00
1	0.00	0.00%	0.00

The best comparison is best done when the data in Table 4.5 is represented graphically on a semi-logarithmic scale. This is presented in Figure 4.8 where fragment size is plotted on a logarithmic scale following accepted conventions.

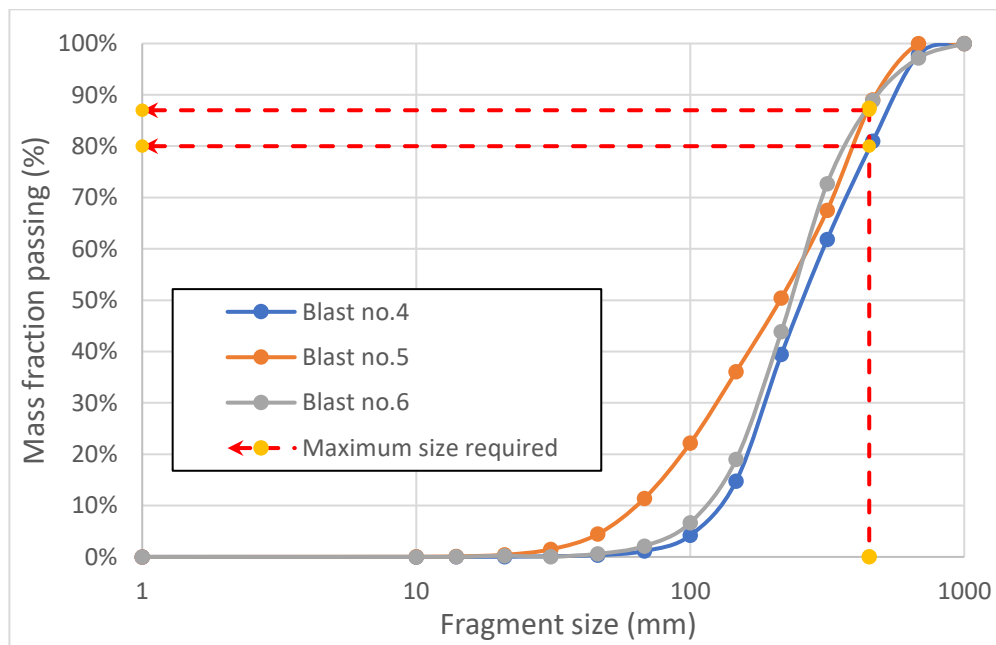


Figure 4.8: Particle size distributions plotted for blasts #4, #5 and #6, with a maximum size requirement of 450 mm.

It can now be seen from Figure 4.8 that blast #4 produced the coarsest muckpile with a marginal number of oversized fragments. The distinction amongst the three blasts is even more evident when examining the spread of their corresponding curves. Indeed, blast #5 shows a gradually sloped curve with the spread extending down to about 10 mm. This is indicative of the presence of smaller fragments in the muckpile. The observation is in line with Choudhary et al. (2021) who noted that the flatness and spread of the curves signify a lack of uniformity in fragmentation. In contrast, blast #6 produced a steeper and less spread curve, indicating a muckpile with more uniformly sized fragments. One may argue that blast #5 performed the best considering that the granite quarry aims at consistently producing narrowly sized muckpiles as required by the market.

4.4.2. Effect of inter-hole delay timing on rock fragmentation

Blasts #1, #2, and #3 were designed with inter-hole delay timings of 17 ms, 9 ms, and 6 ms respectively. This made it possible to gain some insight into the effects of delay on blast fragmentation. For reference, Figure 4.9 shows the blast layout design for blast #3 while the corresponding experimental conditions were presented earlier in Table 4.3. The blast design maintained a stemming length of 2.5 m and an inter-row delay timing of 23 ms.

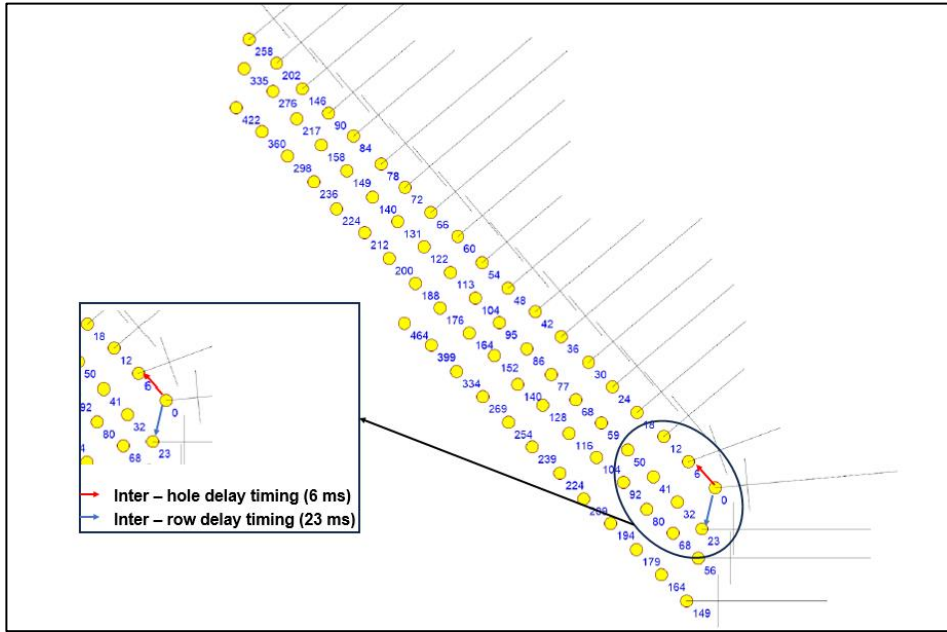


Figure 4.9: Design for blast #3 incorporating an inter-hole delay timing of 6 ms and an inter-row delay timing of 23 ms

Table 4.6 summarises the results from the muckpile analysis report for blast #3 as well as blasts #1 and #2. The comprehensive raw data is documented in Appendix D1, D2, and D3 at the end of the dissertation.

Table 4.6: Characteristics of the muckpile size distributions corresponding to blasts #1, #2, and #3

Wipfrag outputs	Blast #1	Blast #2	Blast #3
D01	33.69 mm	94.07 mm	45.58 mm
D20	137.38 mm	213.02 mm	134.98 mm
D80	920.50 mm	531.32 mm	650.78 mm
PAR	22938	14132	11360
X_{max}	1290 mm	1310 mm	856 mm
X_{50}	492.78 mm	322.47 mm	276.08 mm
X_c	661.53 mm	393.47 mm	409.70 mm
n	1.67	3.100	1.94
b	1.85	4.950	2.59

Blast #2 achieved the finest and most uniform fragmentation. This is because the blast recorded the largest D01 at 94.07 mm and the steepest curve slope ($n = 3.1$). There is also an indication of a higher production of fine particles with $b = 4.95$.

Looking at blast #1, this trial produced the coarsest material as evidenced by the lowest production of fines ($b = 1.85$) and the highest D80 = 920.50 mm. Also of note is the mean size $X_{50} = 492.78$ mm and the characteristic size $X_c = 661.53$ mm. On the other hand, blast #3 achieved a balance between reduced oversize fragments and finer fragmentation. Indeed, the blast produced the smallest maximum particle size ($X_{max} = 856$ mm) and moderate n and b values at 1.94 and 2.59 respectively.

The impact of varying blast design on fragmentation is clearly highlighted in Table 4.6. Summarily, blast #2 yielded a fine and uniform muckpile while blast #1 produced larger particles. Blast #3, however, achieved an intermediate performance between blast #1 and #2. And by rendering the distribution curves, Figure 4.10 highlights the presence of oversized materials for blast #1. It is important to note that 44% of the material in blast #1 is over the 450 mm specification set by the quarry. This makes it more oversized than blasts #2 and #3 that resulted in 26% and 34% oversize materials respectively. It is also clear that secondary breaking would be required on these large fragments.

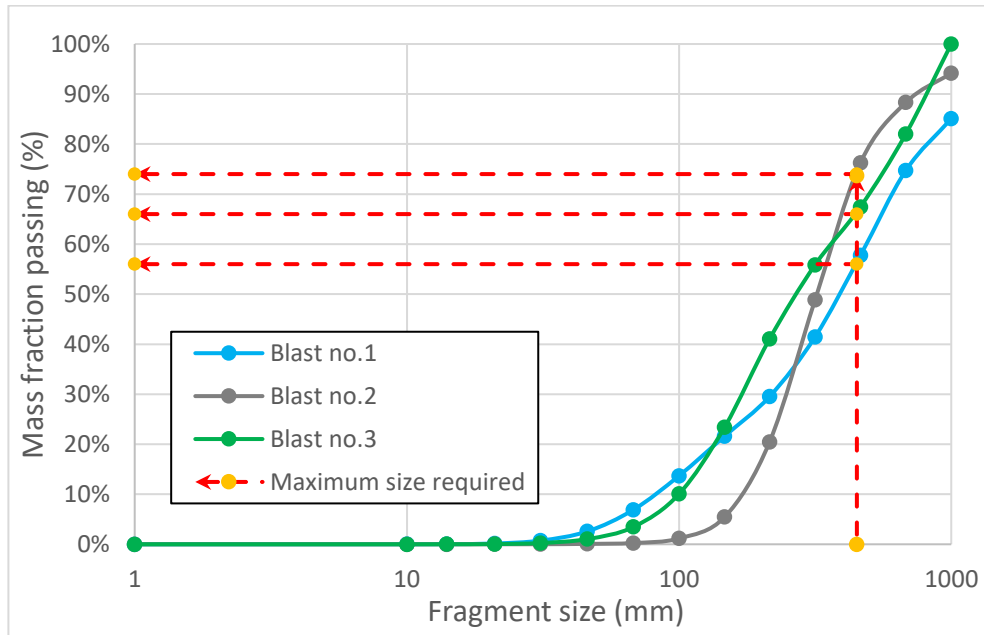


Figure 4.10: Particle size distributions plotted for blasts #1, #2, and #3, with a maximum size requirement of 450 mm.

Going back into the historical blasts, it is noted that blast no. 0223 (refer to Table 4.1) and blast #1 were carried out using similar blast designs. However, a striking difference in oversized materials is apparent with blast no. 0223 and blast #1 producing 15% and 44% oversize respectively. This possibly points to a flaw in the historical estimates where the fraction of oversize material is understated. It is posited that the actual fragmentation was not adequately represented by visual estimation. Be that as it may, the experimental results in Figure 4.8 and Figure 4.10 highlight how crucial it is for the quarry to use image analysis for improved estimation of fragmentation.

4.4.3. Safety evaluation of the experimental blasts

Throughout the experimental work, safety was the top priority. Given the commitment to safety, the initial assessment of the results began with reviewing video footage and ground vibration data. This primary examination was essential to understanding the immediate impact and

consequences of the blasts. Only after this careful evaluation did the study proceed to the detailed analysis of the fragmentation results. This section looks at the blast outcomes in relation to safety. The video recording and ground vibration data are analysed for the purpose.

4.4.3.1. Analysis of video recording

Figure 4.11 provides a visual presentation of selected blasts that were captured through a high-speed video recording during the trials. Instances of stemming ejection and flyrock were spotted as part of the assessment.

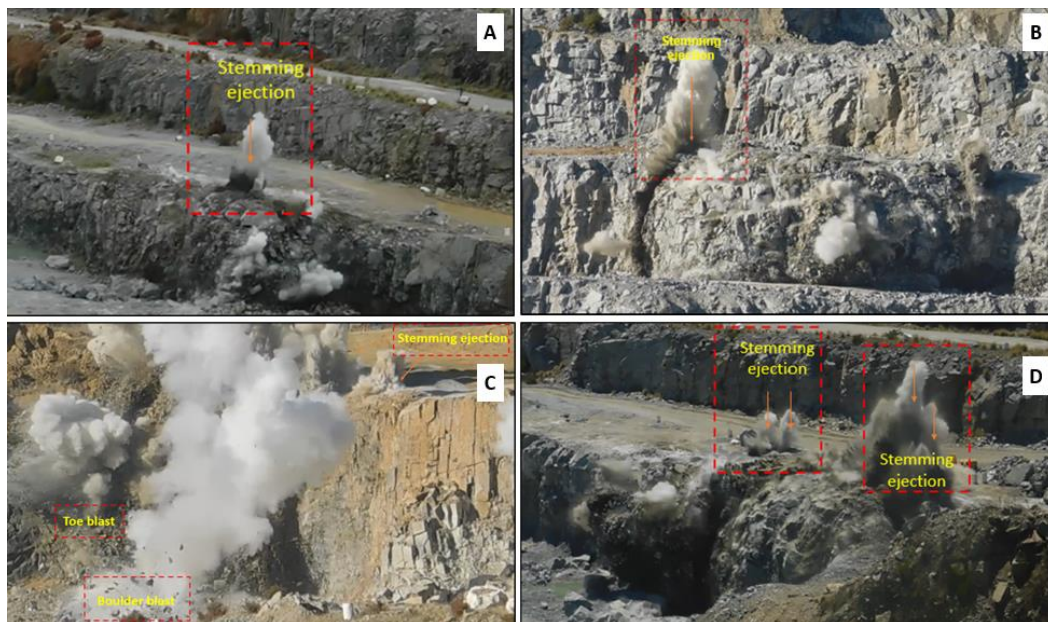


Figure 4.11: A – Detonation with a minimal stemming ejection for blast #1; B – Blast #4 with four blast hole stemming ejection; C – Stemming ejection in blast #5; and D – Stemming ejection in blast #6

As shown in Figure 4.11(A) and (B), blast #1 experienced a single stemming hole ejection with little flyrock. Blast #4 also led to few blast holes ejecting the stemming material. The increased ejection was primarily caused by the unique arrangement of blast #4, which included additional blasting area at the toe with several in-situ boulders. Nevertheless, both blasts had maintained acceptable stemming ejection. The stemming was therefore

effective at containing the explosive energy while also preventing the premature venting of the gases through the blast holes.

Several instances of stemming ejection were observed with blasts #5 and #6 which contributed to generating notable flyrock (see Figure 4.11 C and D). Interestingly, the flyrock stayed within the 500-m blast radius as required by safety regulations.

To sum up, the empirical results presented above point out the importance of ongoing monitoring of blasts for controllable and uncontrollable variables. This ensure that occurrence of stemming ejection and flyrock are reduced to within the safe operating limits set by the relevant departments in the jurisdiction.

4.4.3.2. Analysis of ground vibration data

The seismograph measurements from the six blast trials collected at the quarry viewpoint and primary crusher locations are examined in this section. The associated results provided in Figure 4.12 shows notable differences in particle velocity and frequency. This translates in the large scatter of data observed. Important information on the effects of stemming and delay timing on ground vibrations can also be extracted from Figure 4.12; however, the analysis is beyond the scope of the dissertation. Comprehensive details on the seismograph results produced from the quarry viewpoint and primary crusher locations are available in Appendix D8. Suffice it to say that all blasts were below the USBM limits deeming the tests conducted as safe.

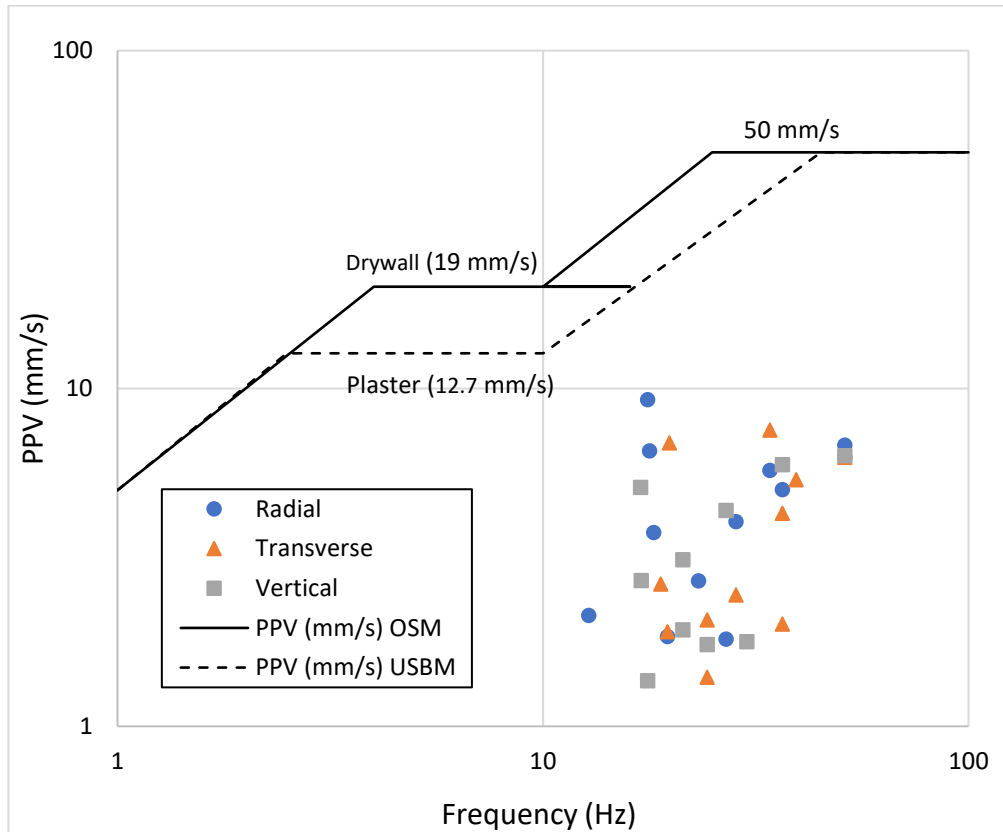


Figure 4.12: Map of the peak particle velocities and frequencies for the ground vibrations generated during all the blasts to verify compliance with USBM standards

Let us briefly look at the seismograph measurements from a quantitative point of view.

The velocity measurements for blast #1 at the primary crusher were 2.127 mm/s in the radial direction, 2.064 mm/s in the transverse direction, and 1.365 mm/s in the vertical direction. A balanced distribution of vibrational energy across the components was shown by the corresponding frequencies which were 21.27 Hz, 20.64 Hz, and 13.65 Hz respectively. At the quarry viewpoint, the particle velocity of 6.795 mm/s (radial), 6.445 mm/s (transverse), and 3.493 mm/s (vertical) were recorded. The corresponding frequencies of 67.95 Hz, 64.45 Hz, and 34.93 Hz indicated an unbalanced distribution of vibrational energy. The higher velocity and frequency readings confirm that the quarry viewpoint was much closer to the blast.

In terms of blast #2, results from primary crusher displayed a slight increase in ground vibrations compared to blast #1 with readings of 3.747 mm/s (radial), 2.445 mm/s (transverse), and 2.699 mm/s (vertical). Corresponding frequencies were 3.747 Hz (radial), 24.45 Hz (transverse), and 26.99 Hz (vertical). As for the quarry viewpoint, greater particle velocities were again noted with radial velocity of 4.032 mm/s, transverse velocity of 2.635 mm/s, and vertical velocity of 3.112 mm/s. Corresponding frequencies were also higher at 40.32 Hz radially, 26.35 Hz transversely, and 31.12 Hz vertically.

For blast #3, the primary crusher location recorded 5.017 mm/s for radial velocity, 7.525 mm/s for transverse velocity, and 4.35 mm/s for vertical velocity. The associated frequencies were 18.10 Hz, 19.05 Hz, and 17.46 Hz respectively. Conversely, the quarry viewpoint shows somehow greater magnitudes in radial, transverse and vertical velocities at 6.538 mm/s, 6.892 mm/s, and 5.098 mm/s respectively. For blast #4, the quarry viewpoint yielded 6.255 mm/s (radial), 6.318 mm/s (transverse), and 6.147 mm/s (vertical) while corresponding frequencies were 62.55 Hz, 62.55 Hz, and 63.18 Hz. Blast #5, on the other hand, registered readings of 9.271 mm/s (radial), 4.2672 mm/s (transverse) and 5.9436 mm/s (vertical) at the primary crusher with frequencies of 17.60 Hz, 36.50 Hz and 36.50 Hz respectively. A distinct pattern was seen with blast #6, where the main crusher exhibited lower readings: 1.842 mm/s (radial), 1.397 mm/s (transverse), and 1.778 mm/s (vertical). The frequencies measured were 18.42 Hz (radial), 13.97 Hz (transverse), and 17.78 Hz (vertical). The quarry viewpoint, located 700 m from the blast, recorded significantly higher particle velocities of 5.715 mm/s in the radial direction, 5.366 mm/s in the transverse direction, and 3.556 mm/s in the vertical direction. Frequencies were marginally higher at 57.15 Hz radially, 53.66 Hz transversely, and 35.56 Hz vertically.

Finally, the most important note to make is that all the recorded vibrations were below 12.7 mm/s. This is the safe limits set by the USBM as can be seen in Figure 4.12. This is further reinforced by the fact that airblast levels were also well within the established safety thresholds of 134 dB as displayed in Figure 4.13.

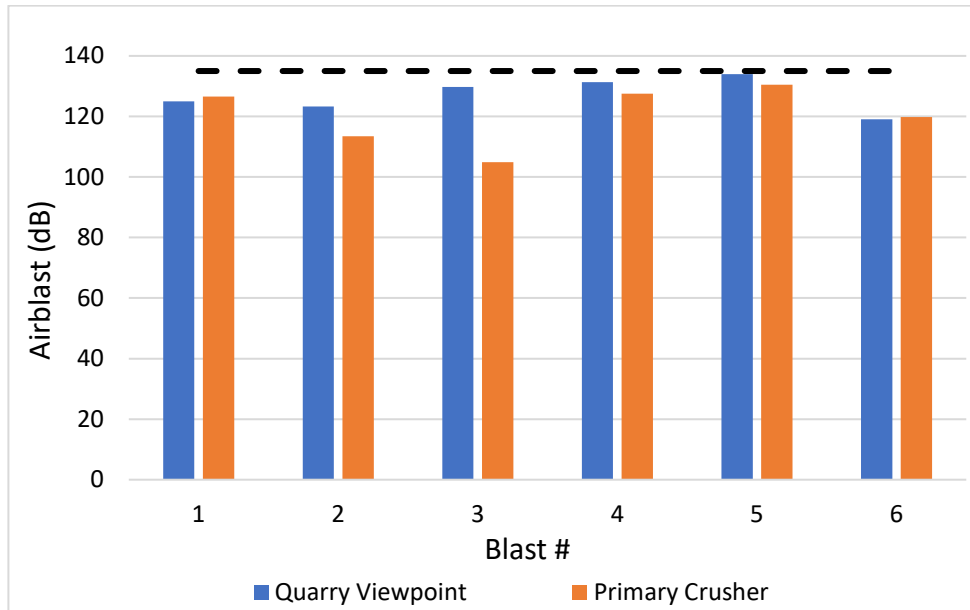


Figure 4.13: Airblast levels below the safety threshold as measured for the six blast trials at the quarry viewpoint and the primary crusher

4.5. Statistical analysis

A statistical analysis of the results highlighting the impact of stemming length and inter-hole delay timing on mean fragmentation size is carried out in this section. The analysis shows that the relationship between fragmentation size and stemming length can be adequately described by a linear function. On the other hand, the influence of the inter-hole delay timing seems to require a power function.

4.5.1. Relationship between mean fragmentation size and stemming length

The impact of stemming length on rock fragmentation size is statistically assessed in this sub-section. The mean fragmentation size X_{50} is used because it reduces the complexity of describing a particle size distribution into a single representative value.

Based on the results covered in Sections 4.4., it was established by curve-fitting that the correlation between stemming length and mean fragmentation size can be represented as shown in Figure 4.14.

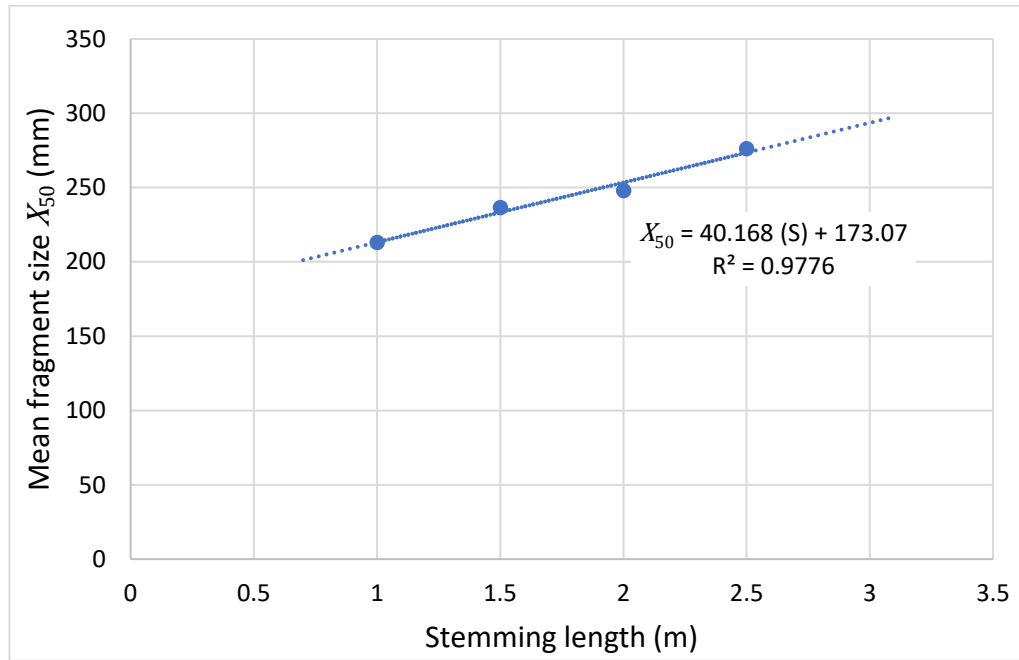


Figure 4.14: Relationship between mean fragmentation size and stemming length

As seen in Figure 4.14, stemming length is a critical factor that influences rock fragmentation. A strong correlation between mean fragmentation and stemming length is noted as indicated by the statistical correlation R^2 of 0.9776, which is close to 1. An increase in stemming length subsequently leads to a proportional increase in mean fragmentation size. Conversely, smaller fragment sizes can be produced at shorter stemming lengths. Conversely, shorter stemming lengths can result in smaller fragment sizes, though the extent depends on factors such as rock type and blast parameters.

These findings align with several studies exploring the effect of stemming on fragmentation. Indeed, Prasad et al. (2017) conducted a comparable investigation in an open cast mine and reported that the mean fragment size increases as stemming length to burden ratio increases. Most importantly, this occurred while maintaining all other burden-related parameters constant throughout the blasting process. The findings by Prasad et al. (2017) strongly suggest that increasing the stemming length played a key role in shaping the fragmentation outcomes. It could therefore be argued

that longer stemming lengths likely influence the distribution of explosive energy within the blast block thereby affecting the final fragmentation size.

Another investigation conducted by Cevizci and Ozkahraman (2012) examined the effect of blast stemming length on rockpile fragmentation. Their research emphasised the importance of a careful selection of stemming length in any blasting operation. This is because here also, the reported findings align remarkably well with the results covered in this dissertation. Cevizci and Ozkahraman (2012) concluded that the choice of stemming length should be done carefully because the formation of undesirable boulders closely depends on it.

In a follow-up study, Cevizci (2013) was able to demonstrate that stemming length plays a critical role in rock fragmentation. He argued that shorter stemming lengths lead to blasts of improved fragmentation quality and operational efficiency.

Lastly, the careful consideration of stemming length selection can significantly impact the size and distribution of fragments. This has also been observed in this study as shown in Figure 4.14. And in practical terms, stemming length should systematically be used at the quarry to adjust fragmentation outcomes until optimised blasting is obtained.

4.5.2. Relationship between fragmentation size and inter-hole delay timing

The timing of inter-hole blasting delays has a significant effect on the size and distribution of fragments produced. Research indicates that optimal delay times can increase fragmentation efficiency, while poor timing can result in outcomes that are not ideal from a safety and fragmentation point of view (Chung and Katsabanis, 2001; Zhou et al., 2024).

As far as this research study goes, Figure 4.15 shows the correlation between delay timing and average fragmentation size X_{50} . The extended Kuz-Ram model in Equation (2.19) was also tested and successfully validated against the experimental blast data collected in this study.

Appendix D9 provides ample information of the model parameters and curve-fitting done on the extended Kuz-Ram model.

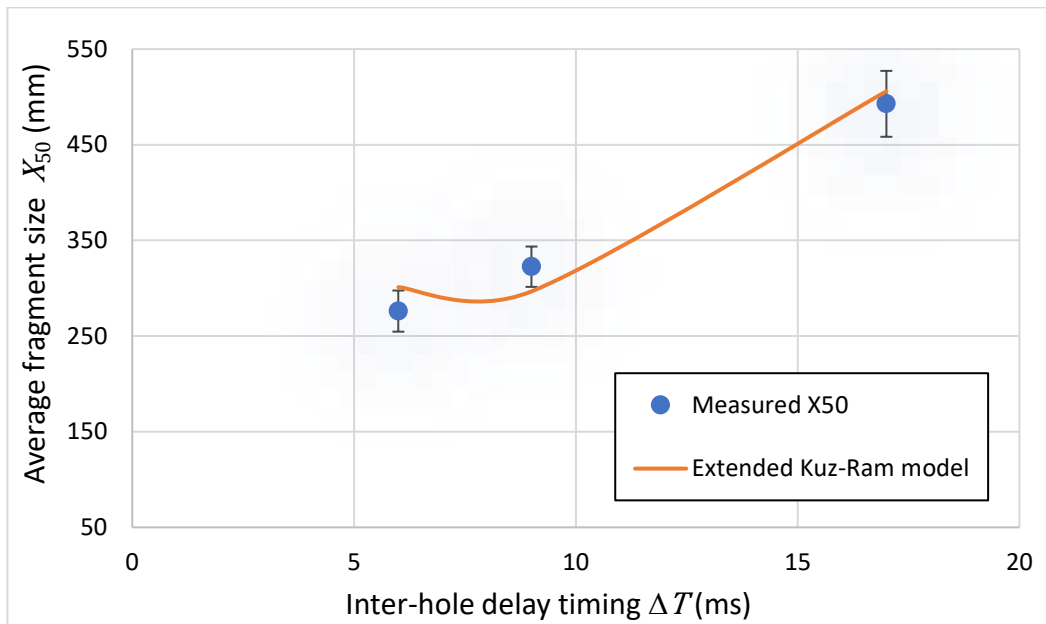


Figure 4.15: Relationship between mean fragmentation size and inter-hole delay timing with error bars representing the 95% confidence interval

Unlike the trend provided by the measured data points, the extended Kuz-Ram model displays a slight downwards concavity around 8 ms. This suggests that as the delay timing increases, the mean size X_{50} is expected to decrease slightly before increasing steadily. And based on the relative position of error bars about the solid line, it may be argued that the actual data and the extended model are statistically similar at a 95% confidence level. Table 4.7 also provides some statistics for a qualitative assessment of the variations inherent to the image-based measurement of the muckpile size done by means of repeated camera captures of the same.

As a way forward, additional blast tests are required to reinforce the provisional statement alluding to the validity of the extended Kuz-Ram model. And until that is done, it is reasonable to accept the statistical similarity between actual measurements and the extended model.

Table 4.7: Statistics relating the measurement of the mean fragmentation size at 95% confidence

Muckpile images	Mean fragment sizes (X_{50})		
	Blast #1	Blast #2	Blast #3
1	524.56	306.0	297.8
2	436.08	339.45	266.02
3	485.64	320.57	265.06
4	484.83		
5	532.78		
Mean	492.78	322.47	276.2
Standard deviation	38.533	18.632	18.632
Standard error	17.232	10.551	10.757
Confidence error	34.465	21.10	21.514

The statistics generated for blasts #1, #2, and #3 at 95% confidence reveal significant differences in the fragmentation results. For blast #1, the mean fragment size of 492.78 mm combined with a confidence error of ± 34.465 mm indicates that the true mean fragment size lies within the range of 458.32 mm to 527.25 mm. Similarly, for blast #2, the mean fragment size can be quoted as 322.47 ± 21.10 mm at 95% confidence while blast #3 is at a mean fragment size of 276.2 ± 21.514 mm. The three ranges of mean size values do not overlap suggesting that the three blasts are statistically different. Mean sizes predicted with the extended Kuz-Ram model, on the other hand, fall within these 95% confidence ranges; hence, the statistical similarity argued earlier between actual measurement and extended model.

Another important note is that inter-hole delay timing has been reported to plays an enabling role in achieving optimal rock fragmentation (Liu and Katsabanis, 1997). Additional remarks by Winzer et al. (1979) stressed the importance of accurate timing in minimizing noise, vibration, fly rock, backbreak, and poor fragmentation while achieving consistent blasting

results. Saadatmand Hashemi and Katsabanis (2020) also stated that inter-hole delay affects how stress waves interact within the rock mass. An excessively short delay can cause interference and lead to uneven fragmentation. On the other hand, excessively long delays between detonations can lead to energy dissipation. This reduced efficiency can result in incomplete fragmentation.

So, in summary, it can be argued for this research that the limited observations made on the effects of inter-hole delay timing agree with the available literature on the matter. But more tests are required in future for a comprehensive analysis of the phenomenon.

4.6. Discussion of the fragmentation results

4.6.1. Contribution of stemming length to rock fragmentation

Based on the findings presented in Section 4.3.1, the effect of stemming length on rock fragmentation is significant and cannot be overlooked. Indeed, proper stemming is essential to containing and transferring the explosive energy to the rock mass. This ensures that the desired fragmentation is achieved. Insufficient stemming causes premature gas venting and coarse fragmentation (see Figure 4.11). Conversely, excessive stemming reduces energy transfer and limit breakage efficiency as noted by Prasad et al. (2017). As presented earlier in Section 4.4.1, a directly proportional relationship is demonstrated between stemming length and mean fragment size. An increase in stemming length leads to an increase in mean fragmentation (see Figure 4.14). Conversely, shorter stemming does not necessarily yield the best fragmentation.

To determine the most effective blast settings, a comparison of the fragmentation outcomes across the three blasts was done. According to the blast results in Table 4.4, blast #6 would be considered to have yielded the best fragmentation. Figure 4.8 provides evidence for this where blast #6 exhibits a relatively narrow particle size distribution than the other two blasts. And despite this, boulders are still present with 10% above 450 mm.

This can be attributed to the stemming ejection reported in Figure 4.11(D) that led to some energy loss during the blast. Additionally, the presence of a prominent cracks and the blocky structure of the bench face also contributed to the higher mean fragmentation size (see Appendix B5). In contrast, blast #4 shows a wide size distribution due to a greater fraction of fine particles. Blast #5 meets the maximum size requirement but with a wider particle size distribution compared to blast #4. Therefore, while blast #5 meets the maximum size requirement, blast #6 is still generally preferred due to its narrower particle size distribution.

4.6.2. Contribution of inter-hole delay timing to rock fragmentation

The extended Kuz-Ram prediction model was utilised to understand how inter-hole delay timing affects rock fragmentation. This approach proved particularly valuable due to the limited number of trial blasts (only three) that specifically focused on inter-hole delay variations. With such a small dataset, identifying clear trends and patterns in fragmentation behaviour was challenging. However, this limitation was overcome by means of the empirical modelling presented in Section 4.5.2 with detailed information available in Appendix D9. Figure 4.15 alluded to the possibility that the minimum X_{50} may fall between 6 ms and 9 ms. This window hints to the need for further enquiry into the effective use of energy to break the rock mass.

In terms of benchmarking, the effect of inter-hole delay timing reported in the present research are deemed consistent with past studies. These include the following papers that were covered extensively in Section 2.2.2. of the literature review: Bergmann et al. (1974), Stagg (1987), Kopp (1987), Bosman et al. (1997), Otterness et al. (1991), and Cunningham (2005). By and large, shorter delays tend to produce a fine and uniform muckpile size distribution. They should be the preferred option for the quarry where delays between 6 ms and 9 ms should be explored.

4.7. Empirical modelling of rock fragmentation

The accurate prediction of the size distribution of fragmented rocks after blasting is essential to efficient and cost-effective operations in the mining and quarrying industries (Esen, 2017). It is against this backdrop that this section compares the performance of two prominent fragmentation models: the Kuz-Ram and the KCO. The comparative analysis is done to identify the most suitable model for the quarry under investigation.

4.7.1. Modelling using the Kuz-Ram and KCO models

The Kuz-Ram and KCO models rely on the blast design parameters and rock properties some of which are available in Appendix A. These were used as inputs in Equations (2.5) to (2.18) for prediction purposes.

4.7.1.1. *Modelling the effects of inter-hole delay timing*

Table 4.8 summarises the fragmentation results for blast #1 generated from the computation of Equations (2.5) – (2.18). It can be seen that the Kuz-Ram and KCO models predict similar retained mass fractions. However, these predictions overestimate the average fragment sizes (i.e., 150 – 450 mm) compared to WipFrag measurements. Note here that the quarry classifies material under 150 mm as fine material while the intended size range defined as 150 – 450 mm is termed average size.

Table 4.8: Predicted fragmentation for blast #1

Fragment size	Mass fraction retained (%)		
	WipFrag	Kuz-Ram	KCO
Fines < 150 mm	22	18	16
Average (150 – 450 mm)	34	45	51
Oversize (>450 mm)	44	37	33

Moreover, both models underpredicts the oversize material generated in the blast (also see Figure 4.16). In essence, the Kuz-Ram model and the KCO model estimated the fraction of fine material well but overestimated the

average sized fragments. The KCO model therefore seems to have performed the least for blast #1.

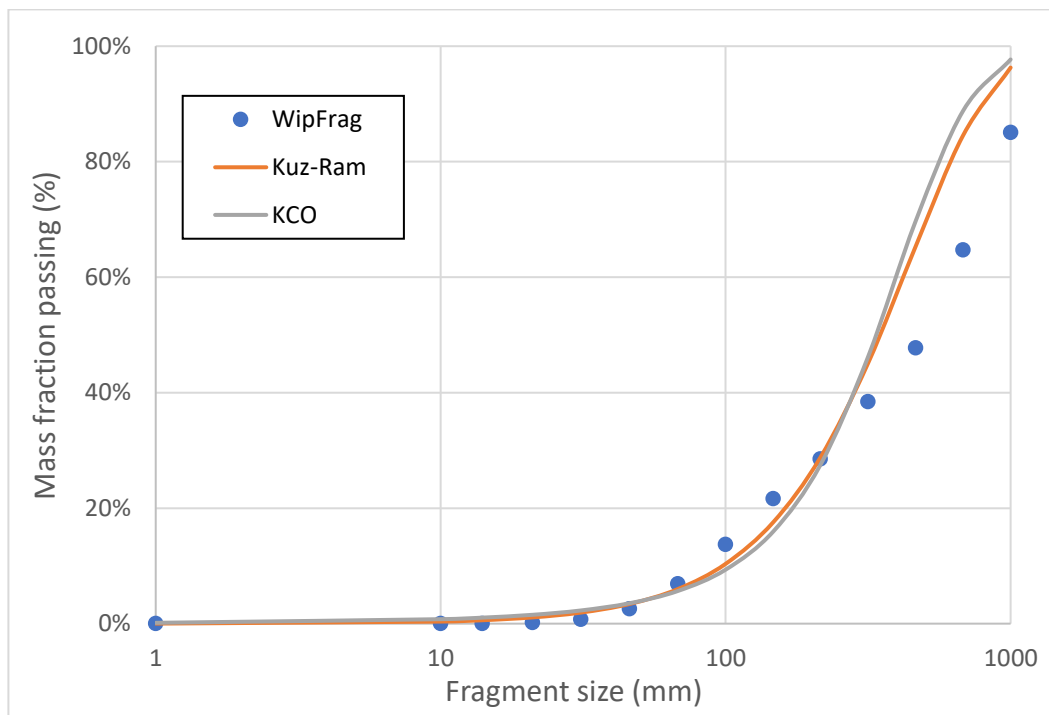


Figure 4.16: Muckpile size distribution predicted for blast #1

Looking at Table 4.9, one can argue that both models overestimated the fine fraction while the average material was underestimated. By and large, the Kuz-Ram model described the WipFrag measurement reasonably well at oversize and average fractions.

Table 4.9: Predicted fragmentation for blast #2

Fragment size	Mass fraction retained (%)		
	WipFrag	Kuz-Ram	KCO
Fines < 150 mm	7	26	17
Average (150 – 450 mm)	67	51	47
Oversize (>450 mm)	26	23	36

A depiction of the predictive modelling is presented in Figure 4.17 which is equivalent to results in Table 4.9 but rendered graphically. The KCO model is seen to predict a coarser muckpile while the Kuz-Ram model is finer with the WipFrag distribution being in-between down to about 300 mm.

Thereafter, models systematically overpredict the finer tail end of the distribution. It is possible that the camera used to take pictures of muckpiles may not have been sensitive enough to capture finer fragments. At this point in time, one may simply say that the two models are not describing well the distribution at finer particle sizes. Further scrutiny is required to elucidate the deviations observed.

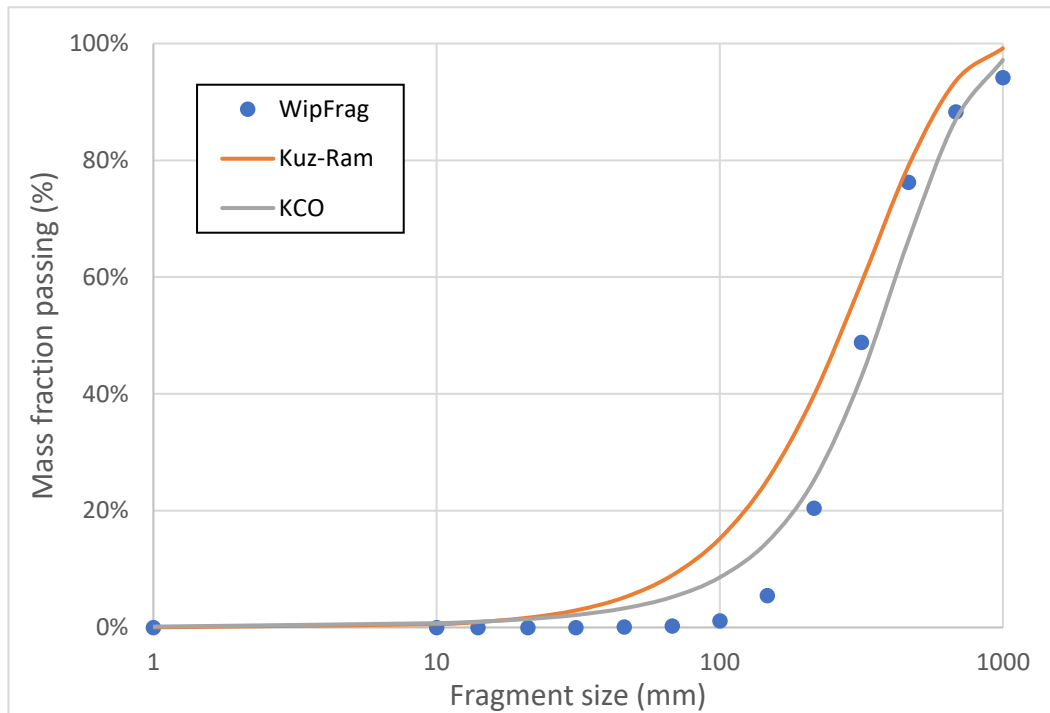


Figure 4.17: Estimated muckpile size distribution for blast #2

Lastly, Figure 4.18 presents the graphical predictions obtained from Kuz-Ram and KCO for blast #2. In this case, the KCO model espouses better the average and fine fragment size distributions. This is in contrast to the Kuz-Ram model that predicts a fine muckpile size distribution throughout.

In terms of fragment size distribution, Table 4.10 shows that fine and oversized fractions are predicted reasonably well with the KCO model. Conversely, the model deviates significantly from the Wipfrag data of the average size fraction. Finally, it can be noted that both the Kuz-Ram and KCO models underestimated the number of boulders produced from blast #3.

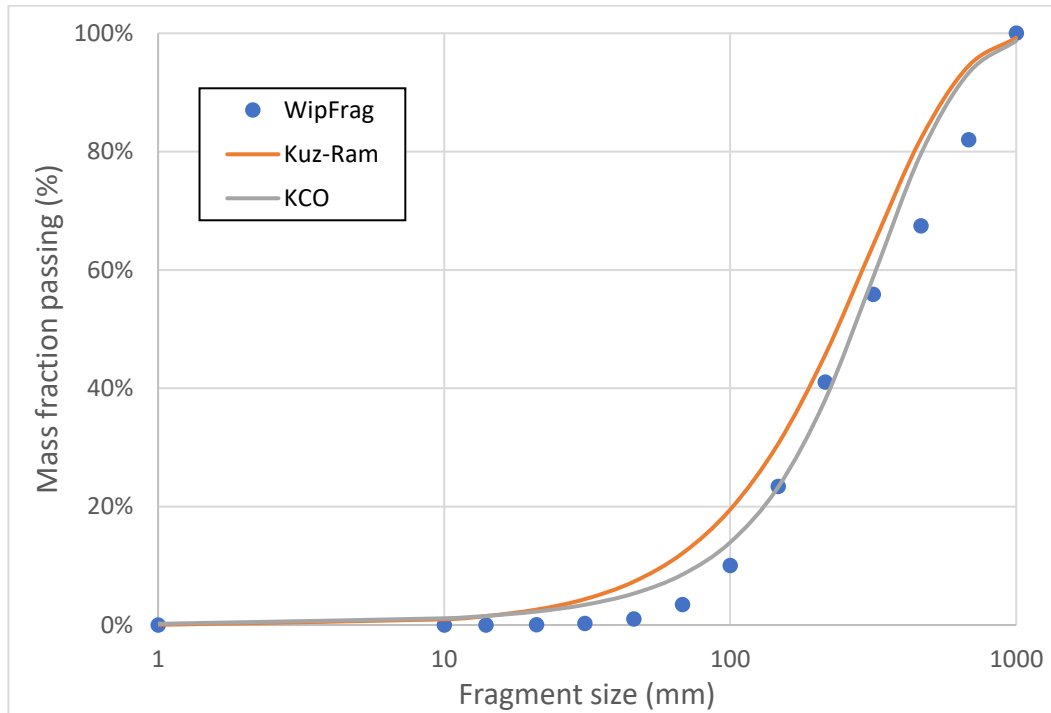


Figure 4.18: Muckpile size distribution predicted for blast #3

Table 4.10: Predicted fragmentation for blast #3

Fragment size	Mass fraction retained (%)		
	WipFrag	Kuz-Ram	KCO
Fines < 150 mm	24	31	24
Average (150 – 450 mm)	32	49	54
Oversize (>450 mm)	44	20	22

The two fragmentation models (i.e., Kuz-Ram and KCO) evaluated in this section were found to consistently overpredict at various degrees the fine fraction of muckpile for blasts #1, #2, and #3. This is in contradiction with Woldeselassie et al. (2021) as well as Omotehinse and Taiwo (2023) who found that the Kuz-Ram model underpredicted finer particles. The KCO model also produced similar trends but with a closer match to the Wipfrag size distributions. Gheibie et al. (2009) and Woldeselassie et al. (2021) also reported a better prediction ability of the KCO model. However, the systematic discrepancies reported in this section may be attributed to variations in geological features and rock properties across the quarry. These are known to significantly affect fragmentation outcomes.

It is also important to examine the mean size X_{50} as a commonly used indicator of rock fragmentation. Table 4.11 provides a summary of the estimated mean sizes for blasts #1, #2, and #3. The KCO model produced estimates closer to actual mean sizes from WipFrag except for blast #1.

Table 4.11: Summary of the predicted mean sizes for blasts #1, #2, and #3

Blast	Mean fragment size X_{50} (mm)		
	WipFrag	Kuz-Ram	KCO
Blast #1	492.78	349	337
Blast #2	322.47	266	357
Blast #3	276.08	236	271

To a certain extent, the KCO model seems to work well at this quarry under investigation. However, a more thorough statistical analysis is explored later in Section 4.7.2. to quantify its overall performance.

4.7.1.2. *Modelling the effects of stemming length*

Let us now look at the performance of the Kuz-Ram and KCO models from the viewpoint of the effects of stemming length on muckpile size distribution.

Table 4.12 provides the actual and predicted mass fractions as classified by the quarry for blast #4.

Table 4.12: Predicted fragmentation for blast #4

Fragment size	Mass fraction passing (%)		
	WipFrag	Kuz-Ram	KCO
Fines < 150 mm	15	23	19
Average (150 – 450 mm)	64	50	54
Oversize (>450 mm)	21	27	27

It appears that the KCO model performs slightly better than Kuz-Ram model even though the two are comparable for fines and oversized. And when these predictions are presented graphically in Figure 4.19, the KCO model yields a slightly coarser distribution than the Kuz-Ram model.

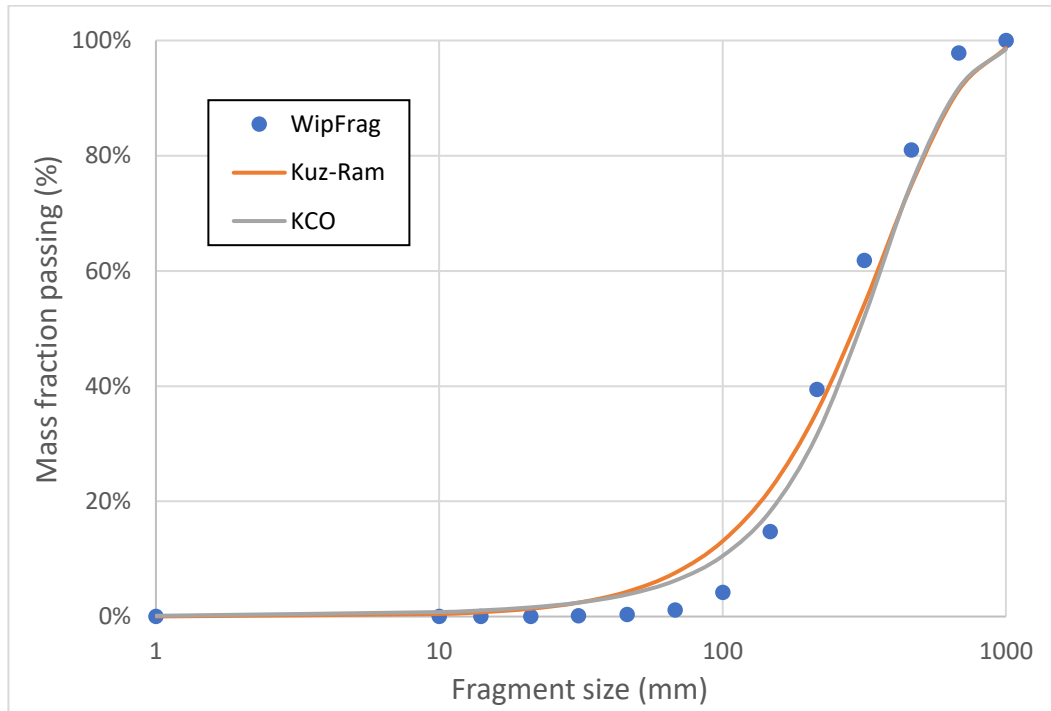


Figure 4.19: Muckpile size distribution predicted for blast # 4

For blast #5, fines were estimated by the Kuz-Ram and KCO models to be 31% and 26% respectively as shown in Table 4.13.

Table 4.13: Predicted fragmentation for blast #5

Fragment size	Mass fraction passing (%)		
	WipFrag	Kuz-Ram	KCO
Fines < 150 mm	36	31	26
Average (150 – 450 mm)	50	53	56
Oversize (>450 mm)	14	16	18

And in terms of particle size distribution, Figure 4.20 shows that the KCO model produced a coarse muckpile closely followed by the Kuz-Ram model while the actual measurements are slightly finer. Overall, the two models provided comparable size distribution estimates for blast #4.

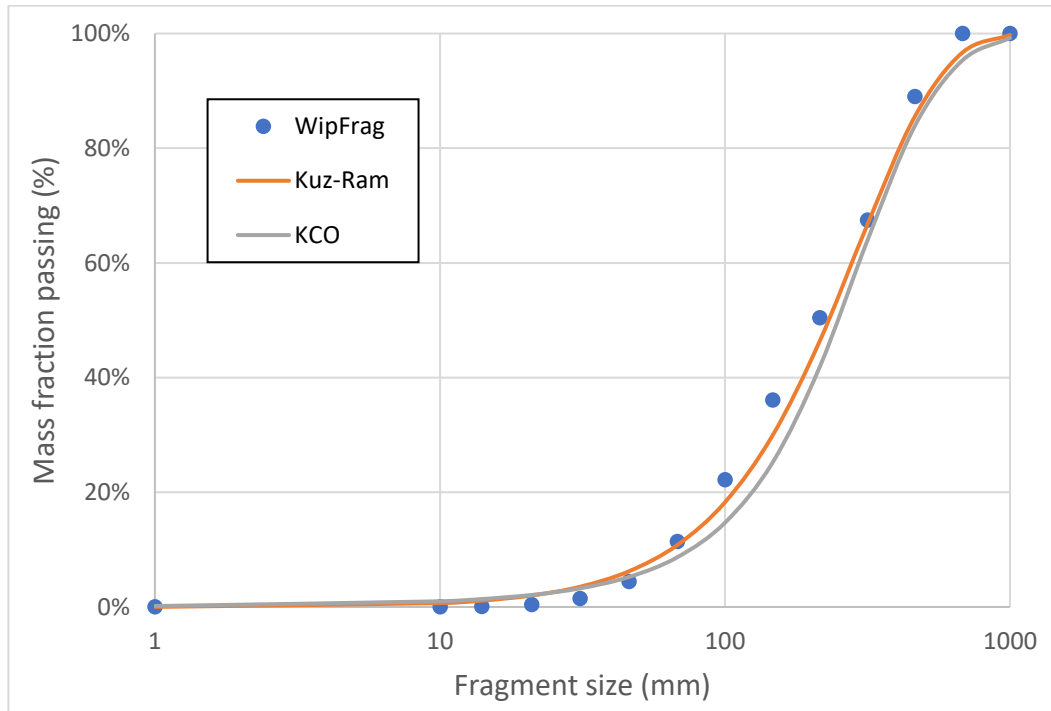


Figure 4.20: Muckpile size distribution predicted for blast #5

Next, the prediction results of the two fragmentation models for blast #6 are shown in Table 4.14 and Figure 4.21. Similarly to the predictions made for blasts #4 and #5, fines are overestimated for blast #6 while the distribution is well predicted for coarse and average sizes, see Figure 4.21. This equally translates in better estimates for these two size fractions as reported in Table 4.14. it may be said that the Kuz-Ram and KCO models predicted the distribution and mass fractions well expected for particles below 150 mm.

Table 4.14: Predicted fragmentation for blast #6

Fragment size	Mass fraction passing (%)		
	WipFrag	Kuz-Ram	KCO
Fines < 150 mm	20	30	26
Average (150 – 450 mm)	67	60	59
Oversize (>450 mm)	13	10	15

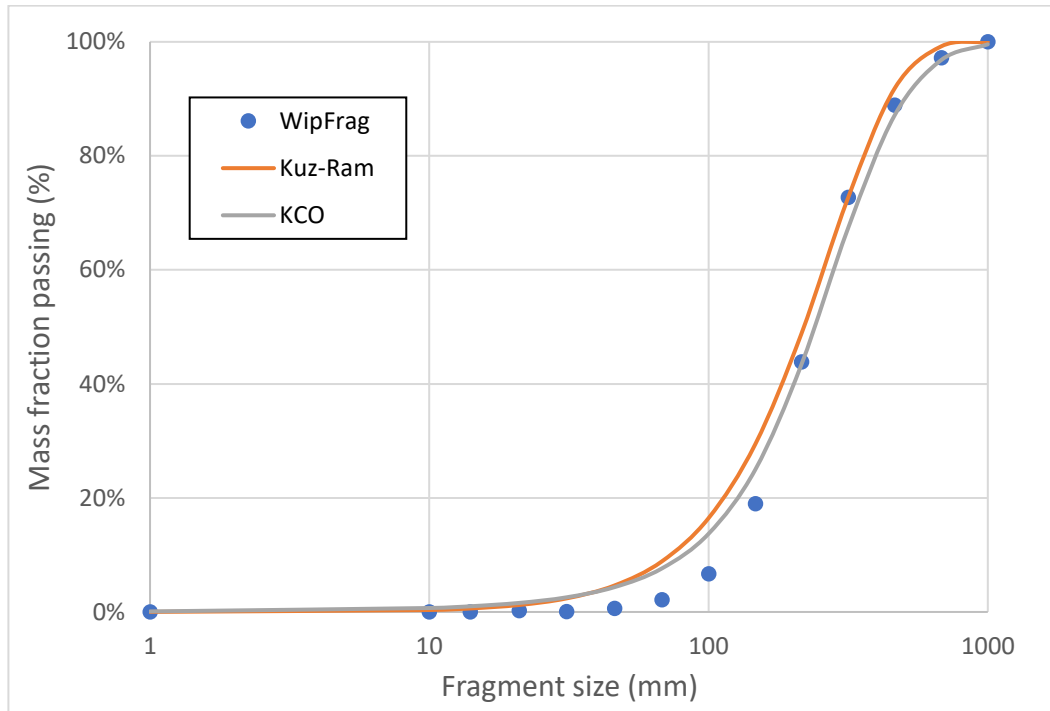


Figure 4.21: Muckpile size distribution predicted for blast #6

Overpredictions at smaller size classes have also been reported by Lawal (2021) amongst others for the Kuz-Ram model. This researcher explained that the Kuz-Ram model frequently overestimates the size of the fragments. In contrast, Esen (2013) reported underestimated Kuz-Ram distributions for fine particles generated by blasting. And for the KCO model, predictions seem to match the actual fragmentation sizes better.

When examining the mean sizes in Table 4.15, several key observations can be made. The mean fragmentation sizes predicted by the Kuz-Ram model are closer to the actual measured sizes for blasts #4 and #5. The KCO model performs better with blast #6.

Table 4.15: Summary of mean sizes expected from blasts #4, #5, and #6

	Mean fragment size X_{50} (mm)		
	WipFrag	Kuz-Ram	KCO
Blast #4	247.96	292	306
Blast #5	212.97	231	249
Blast #6	236.45	219	240

4.7.2. Performance of the fragmentation models: Kuz-Ram versus KCO

The performance of the two empirical fragmentation models (i.e., Kuz-Ram and KCO) was analysed qualitatively in Section 4.7.1. Now in this section, an attempt is made to appraise the two models using rigorous statistical tools. Several statistical indicators are used for the purpose. They are described below. Thereafter, the two models are compared while expected variances from actual fragmentation size distributions are also estimated for the quarry. Note that statistical comparison is done using the WipFrag measurements as the actual reference.

4.7.2.1. Definition of the key performance indicators

Regression model evaluation matrix was employed to analyse the performance of the results obtained. This was instrumental in assessing the prediction accuracy and effectiveness of the Kuz-Ram and KCO models. The matrix for evaluating the regression models included the Mean Absolute Error (MEA), Mean Square Error (MSE), Root Mean Squared Error (RMSE), and Pearson coefficient of determination (R^2).

According to Omotehinse and Taiwo (2023), MAE is a widely adopted indicator that measures the average magnitude of errors in predicting fragmentation size distribution. A smaller MAE value indicates a better model performance, suggesting that the predictions are closer to the actual values. On the contrary, a larger MAE value suggests poorer model performance. MAE is defined as follows (Guo et al., 2021) as expressed in Equation (4.1):

$$MAE = \frac{1}{n} \sum_{i=1}^n |y_i - \hat{y}| \quad (4.1)$$

Where y_i denotes the actual value; \hat{y} is the anticipated value of the output variable; and n is the number of data points.

MSE calculates the average of the squared differences between the estimated mass fractions of fragments in each size class and the actual mass fractions. A model with a lower MSE is more accurate in making

predictions whereas one with a higher MSE is less accurate. MSE is calculated using the following formula (Guo et al., 2021) as expressed in Equation (4.2):

$$MSE = \frac{1}{n} \sum_{i=1}^n (y_i - \hat{y})^2 \quad (4.2)$$

RMSE is a statistical measure that indicates the standard deviation of the differences between values predicted by the model and the actual values. It reflects the variation between two sets of values obtained from different models (Soufi et al., 2018). RMSE is given by (Guo et al., 2021) as expressed in Equation (4.3):

$$RSME = \sqrt{\frac{\sum_{i=1}^n (\hat{y} - y_i)^2}{n}} \quad (4.3)$$

The final indicator is the coefficient of determination R^2 , a statistical measure that evaluates how well a model prediction align with the actual data. Also known as the Pearson correlation coefficient, it was calculated following (Guo et al., 2021) as expressed in Equation (4.4):

$$R^2 = 1 - \frac{\sum_{i=1}^n (y_i - \hat{y})}{\sum_{i=1}^n (y_i - \bar{y})} \quad (4.4)$$

Where y_i is the actual cumulative mass fraction of the fragmentation size distribution and \bar{y} is the actual average mass fraction.

4.7.2.2. Comparison of the two fragmentation models

To validate the accuracy of the Kuz-Ram and KCO models, Microsoft® Excel® was utilized to compute all the key performance indicators presented in Equations (4.2) to (4.5) above. Further details of the computations are available in Appendix G. The two empirical fragmentation models were then compared to the measurements obtained using WipFrag. Following that, Table 4.16 was produced for appraisal.

Table 4.16: Calculated error values for model prediction for all experimental blasts

Blast #	MAE		MSE		RMSE		R^2		Best Predictor
	Kuz-Ram	KCO	Kuz-Ram	KCO	Kuz-Ram	KCO	Kuz-Ram	KCO	
1	4.83	6.03	64.46	95.72	8.03	9.78	0.9904	0.9846	Kuz-Ram
2	6.86	3.94	88.09	24.96	9.39	5.00	0.8636	0.9923	KCO
3	5.83	3.72	53.21	26.43	7.29	5.14	0.8928	0.9937	KCO
4	4.06	3.96	25.14	23.86	5.01	4.89	0.8949	0.9952	KCO
5	2.12	3.60	7.50	23.26	2.74	4.82	0.9983	0.9951	Kuz-Ram
6	3.23	2.60	22.20	12.30	4.71	3.51	0.8963	0.9977	KCO

Table 4.16 indicates that the KCO model performed better than the Kuz-Ram model in 4 out of the 6 blast trials conducted at the quarry.

In terms of expected errors, MAE values are not expected to exceed 6.86% and 6.03% when the Kuz-Ram model and the KCO model respectively are used at the quarry. This suggests that the KCO model may perform marginally better at the quarry.

A final comparison is made in the form of the parity plot showed in Figure 4.22. It can be seen that the Kuz-Ram model yielded a lower coefficient of determination at $R^2 = 0.9533$ compared to the KCO model at $R^2 = 0.9647$. This means that the KCO model explained at 96.47% of the actual fragmentation data. It should therefore be further explored in future for the quarry under investigation.

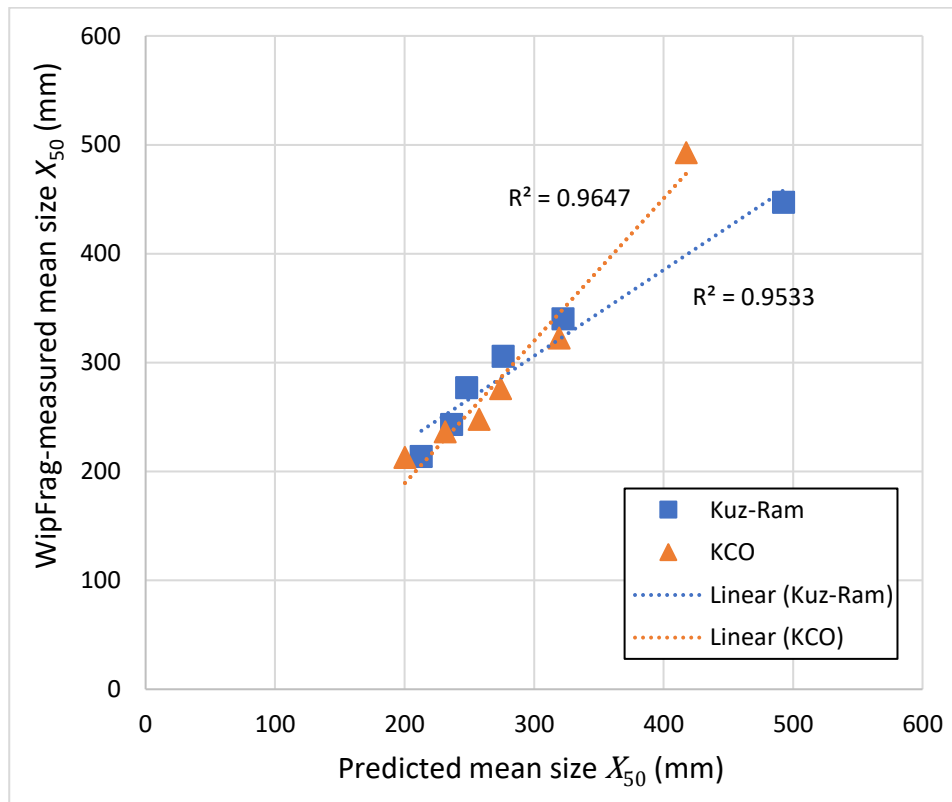


Figure 4.22: Overall correlation between the KCO and Kuz-Ram models

Based on the above analysis, it can be concluded that the KCO model is the most suitable fragmentation model for the quarry. Indeed, Omotehinse and Taiwo (2023) also argued that the model exhibits a lower prediction

error making it superior for the prediction of blast size distributions. Finally, similar conclusions were reached by Woldeselassie et al. (2021) as well as Lawal (2021).

4.8. Summarised findings

In this chapter, the effects of stemming length and inter-hole delay timing on rock fragmentation were investigated. Results showed that stemming length has a substantial effect on fragmentation. Shorter stemming (≤ 1.5 m) was found to generate smaller fragment sizes. Longer stemming (> 1.5 m), on the other hand, is associated with coarser fragmentation.

Rock fragmentation was also monitored for the various times of inter-hole delays used for the blasts. It was established that adjusting the inter-hole delay interval between blasts can improve fragmentation by generating a more uniformly sized muckpile. By applying the extended Kuz-Ram model to the fragmentation data, it was found that short delay intervals (< 6 ms) can cause the rock to remain intact thereby resulting in larger fragments. On the other hand, overly long delays (> 9 ms) may cause blast waves to overlap and subsequently limit the effectiveness of the fragmentation process. A delay timing window period for optimal rock fragmentation was provisional located to be between 6 ms and 9 ms. However, further on-site confirmatory tests are required for the extended Kuz-Ram model so that the optimal delay timing range is refined.

Finally, the fragmentation modelling effort demonstrated that the KCO model surpassed the Kuz-Ram model. Indeed, the KCO model captured variations in stemming length and in inter-hole delay timing better for the most part and for the limited data collected.

4.9. Concluding remarks

In this chapter, the effects of altering stemming length and delay timing on rock fragmentation was analysed based on the experimental data collected.

The experimental data was centred on videos of the blasts and pictures of the muckpiles. Airblast and ground vibrations were also considered in the analysis. The experimental research essentially utilised the following tools: Nikon COOLPIX B500 camera for video and photographic capturing, I-Blast for designing drilling patterns, WipFrag software for muckpile image analysis, and Nomis Seismographs for airblast and ground vibration monitoring.

Nikon COOLPIX B500 and WipFrag played an essential role in analysing muckpile size distributions. Considering the various discrepancies observed especially in trying to model the fragmentation data using the Kuz-Ram model and the KCO models, better versions of these tools may be required with enhanced sensitivity towards finer particles. Also noteworthy is the fact that the I-Blast software was utilized during the design phase of drilling patterns and timing. Instances requiring angled blastholes may have also contributed to the discrepancies between empirical modelling estimates and actual fragmentation data. The above have prompted us to explore estimates of the muckpile size distribution at the mouth of the primary crusher. This is done in the following chapter (i.e., Chapter 5) while the effects of stemming length and inter-hole delay timing are also explored in terms of the throughput of the primary crusher as the next step downstream.

Finally, Nomis Seismographs generated quality data that enable us to conclude that all six blast trials were conducted in compliance with safety regulations in place.

Chapter 5: Effects of rock fragmentation on downstream crusher throughput

5.1. Introduction

The experimental work in Chapter 3 also described the methods used to assess the effect of rock fragmentation on downstream crusher throughput. In this context, the study aimed to look at how fragment size distribution affected crusher performance expressed as a throughput rate. The muckpile size distributions from the six controlled blasts analysed in Chapter 4 were fed to the primary crusher for the purpose.

The investigation started by analysing the properties of the feed size distributions to the primary crusher. These were then compared with the blasting generated muckpile fragmentation from the six experimental blasts. The comparison shed light on the variations in size distribution between muckpile and crusher feed inherent to the image-based fragmentation analysis. Subsequently, the study investigated operational stoppages at the primary crusher for the six run-of-mine (ROM) feeds. This enabled the identification of delays caused by oversized fragments, chute blockages, and material handling inefficiencies. Performance data of the crusher was also analysed to understand the impact of these stoppages on throughput. After that, the performance of the primary crusher was evaluated in terms of throughput rates. Correlations between ROM size, crusher throughput, and operational variables were then established. Regression models and correlation analyses were used to identify important trends and interactions.

The study ended by reviewing the overall effects of rock fragmentation on the performance of the downstream crusher. Among other things, this was to make recommendations on possibilities of optimised blasting for increased throughput, reduced downtime, and improved overall efficiency along the mine value chain.

5.2. Run-of-mine size distributions to the primary crusher

In this section, the characteristics of the run-of-mine (ROM) feed material entering the primary crusher are examined and compared to those of the muckpile where it comes from. Understanding the inconsistencies offers important information about how well the fragmentation size analysis of the muckpiles were done. In doing so, the updated size distributions are used to determine how blast fragmentation affected the crushing operation downstream.

The primary crushing station involved a Pegson Telsmith D type 44 x 48 jaw crusher operating at a closed side setting (CSS) of 127 mm and processing a maximum feed size of 450 mm. The ROM feed to the jaw crusher was measured to see how similar it was to the muckpile size distribution. This was to gain insights into the changeover from blasting to crushing amongst others. This was also to ascertain the possible relationship between blasting practices, material fragmentation, image-based size analysis, and crusher performance.

Numerous studies have reported a strong link between muckpile size distribution and downstream crusher throughput (Lam et al., 2001; Brent et al., 2013; Gaunt et al., 2015). The present research study attempts to determine the extent to which this is valid for the quarry under investigation so that options for improved crusher throughput are identified. To this end, the impact of rock fragmentation on crusher throughput was monitored for the six trial blasts presented in Chapter 4. The feed material to the crusher came from these trial blasts. Here, images were taken at the rear of trucks dumping their payloads at the primary crushing station. These images were processed for particle size distribution using the WipFrag software presented earlier in Section 3.3.5. The comparison between muckpile size distributions and the corresponding ROM feeds is covered in section 5.2.2.

5.2.1. Feed size distributions to the primary crusher

The six different feeds to the primary crusher were measured through image analysis. A camera captured multiple images of the various truck loads from each muckpile. The images were then merged to generate a fragmentation report using the WipFrag software. Figure 5.1 illustrates the ROM size distribution from blast #1 while Figure 3.35 in Chapter 3 shows one of the trucks dumping the material into the primary crusher with the measured width over the tailgate serving as the reference. This single reference measurement of 3 268 mm was measured from the truck and employed in the subsequent image analysis in all the subsequent payloads.

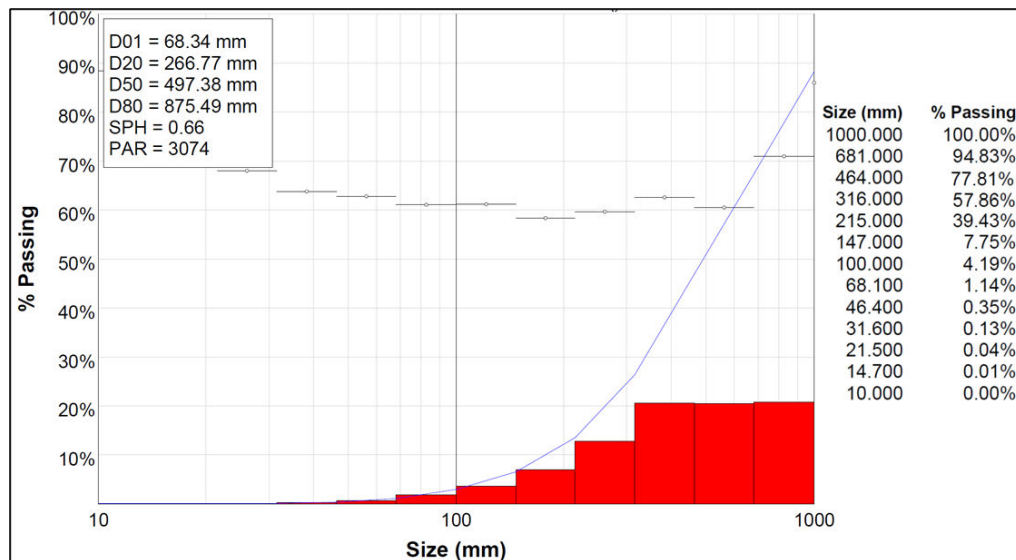


Figure 5.1: Fragmentation analysis report of the crusher feed from blast #1

The cumulative mass fractions measured for each of the six ROM feeds are summarised in Table 5.1. A consistent pattern across all feed materials from the six blasts is noted where the smallest fragments detected by image analysis are of size around 68.1 – 31.6 mm. On the other hand, 3 blasts (i.e., blast #2, blast #3, and blast #4) resulted in truncated feed size distributions evidence of the occurrence of fragments larger than 1000 mm not accounted for by the WipFrag image analysis software. Notably, blast #5 produced a 100% material passing 681 mm suggesting that most of the fragments in its feed were fit for the primary crusher set to receive essentially fragments not exceed the maximum size of 450 mm. However,

marginal deviations from this set size are not uncommon at the crushing station as is discussed later in the chapter.

Table 5.1: Summary of the cumulative mass fractions of the six ROM feeds

Size (mm)	Blast #1	Blast #2	Blast #3	Blast #4	Blast #5	Blast #6
1000	100%	90%	83%	93%	100%	100%
681	95%	63%	73%	75%	100%	97%
464	78%	43%	50%	53%	81%	89%
316	58%	26%	38%	38%	55%	73%
215	39%	15%	23%	24%	39%	44%
147	8%	7%	13%	14%	28%	19%
100	4%	3%	5%	8%	16%	7%
68.1	1%	1%	2%	3%	8%	2%
46.4	0%	0%	0%	1%	3%	1%
31.6	0%	0%	0%	0%	1%	0%
21.5	0%	0%	0%	0%	0%	0%
14.7	0%	0%	0%	0%	0%	0%
10	0%	0%	0%	0%	0%	0%

Next, the key characteristic sizes of the six ROM feeds were analysed. The outcome is illustrated in Figure 5.2 where blasts #1, #2 and #3 are seen to contain coarser particles in the corresponding ROM feeds with substantial portion of material exceeding the 450 mm threshold. In contrast, blasts #4, #5 and #6 show a decrease in coarseness with 50% of material below the accepted feed size of 450 mm. Blasts #5 and #6 yielded ROM feeds were characterised by moderately finer distributions with a significant portion of fragments below 450 mm. While there are still some oversized fragments, these feeds are closer to the accepted feed size. It is also clear that blasts #5 and #6 led to high fragmentation efficiency and resulted in a ROM feed size distribution that aligns well with the crusher capacity. A feed size that mostly stays below the crusher threshold size (i.e., maximum feed size to

the primary crusher) increases throughput and cut down on blockage-related downtime (Gaunt et al., 2015).

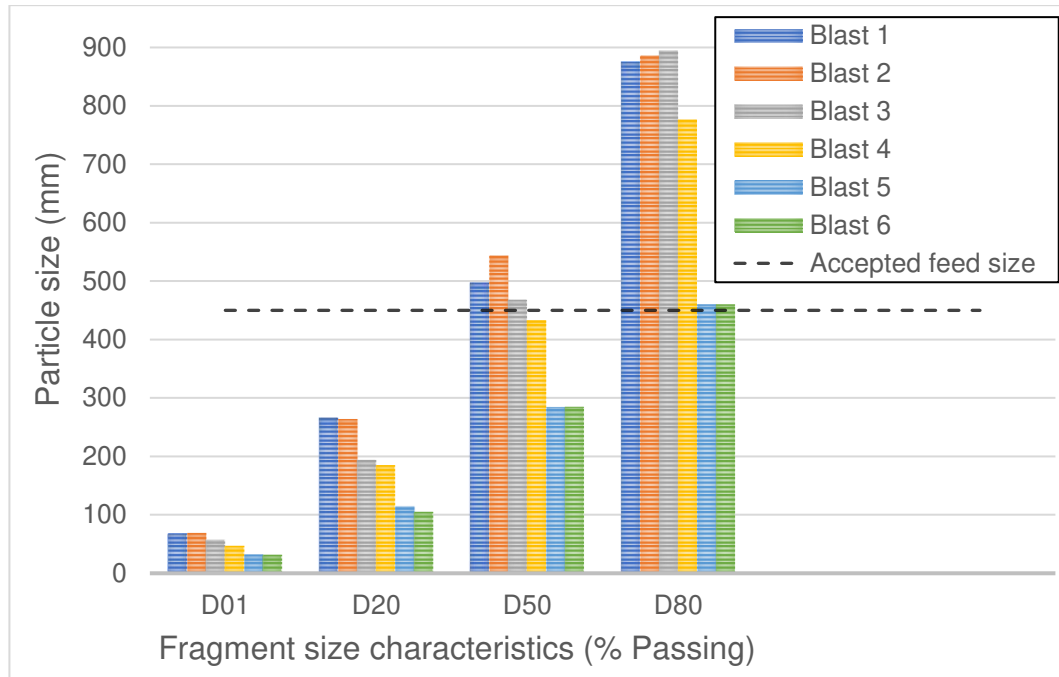


Figure 5.2: Size characteristics of the crusher feeds from the six blasts

5.2.2. Comparison of muckpile and crusher feed size distributions

Material flow through the crusher and its throughput are strongly dependent on the ROM feed size distribution. An essential aspect of this section is to compare the muckpile fragmentation and the corresponding feed size to the crusher. This is later related the data to the performance of the crusher.

In terms of results, Table 5.2 shows a comparison between muckpile and ROM feed from blast #1 as classified at the quarry. It is evident that the material received at the crushing station is substantially different to the initial muckpile. Indeed, less oversize fragments (>450 mm) are present at the crushing station, see 24% versus 55% in Table 5.2. On the other hand, there are more average-sized fragments (150 – 450 mm) in the crusher feed than in the muckpile. Remarkably, about the same mass fraction of fines (>150 mm) is available in the muckpile and the ROM feed at 7% and 9% respectively. This may suggest that oversize fragments may have broken

down into the average size fraction because of handling by excavators at the quarry.

Table 5.2: Summary of particle size distributions at the quarry muckpile and crusher feed for blast #1

Fragment size	Mass fraction passing (%)	
	Quarry	Crusher feed
Fines (<150 mm)	7	9
Average (150 – 450 mm)	38	67
Oversize (>450 mm)	55	24

The cumulative distributions of the ROM feed and the muckpile can also be compared. As can be seen in Figure 5.1., the muckpile is coarser than the feed to the crusher. The proportion of fine particles is similar while the ROM feed size distribution gets steeper between 147 mm and 215 mm. This is also an indication of some breakage probably caused by excavators.

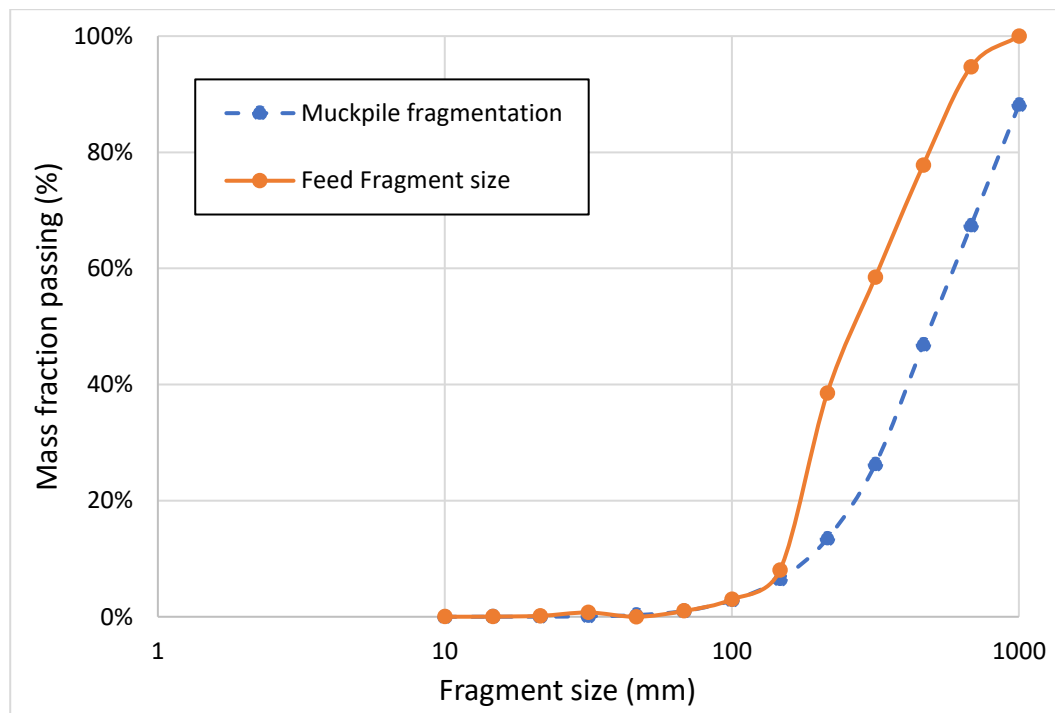


Figure 5.3: Comparison between the size distributions at the crusher feed and the muckpile for blast #1

Similar outcomes are illustrated in Figure 5.4 for blast #2 with the ROM feed also seen to be finer than the initial muckpile.

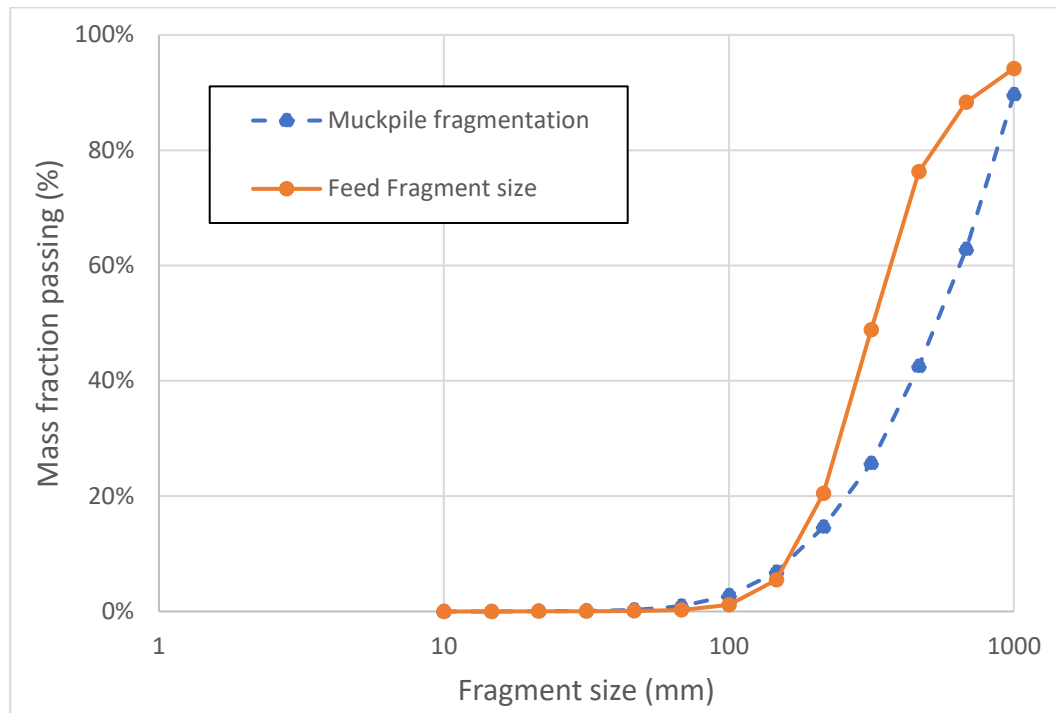


Figure 5.4: Comparison between the size distributions at the crusher feed and the muckpile for blast #2

Viewed in terms of size classification as per the quarry, Table 5.3 also show that blast #2 led to a crusher feed containing fewer oversize fragments than the initial muckpile. Equally, it is conjectured that some oversize fragments of the muckpile experience breakage induced by loading equipment and report into the average fraction.

Table 5.3: Summary of particle size distributions at the quarry muckpile and crusher feed for blast #2

Fragment size	Mass fraction passing (%)	
	Quarry	Crusher feed
Fines (<150 mm)	7	6
Average (150 – 450 mm)	34	74
Oversize (>450 mm)	59	26

The examination of muckpile and crusher feed size distributions done in this section was extended to blasts #3, #4, #5, and #6. Details of the quantitative and graphical results are available in Appendix E. Suffice it to say that the ROM feed presented fewer oversize fragments than the muckpile for all six experimental blasts. Similar trends across the cumulative size distributions were also observed with finer ROM feeds compared to corresponding muckpiles produced at the quarry.

These above findings underscore the importance of measuring particle size distribution across the entire value chain. In the case of the present study, there is evidence of breakage of oversize fragments during the transfer from muckpile to crusher. The protocol followed for image analysis and the associated tools are also another possible source of the discrepancies observed. But in keeping with the integrity of the crusher, it was resolved to use the ROM size distributions and make sense of the actual throughputs and the stoppages observed at the primary crusher in the subsequent sections.

5.3. Stoppages observed at the primary crusher

Instances of downtime at the primary crusher plant are presented in this section. Downtime occurrences, whether planned or unplanned, have a major impact on overall plant performance and production efficiency (Sharma et al., 2009). An assessment of the performance of the primary crusher was conducted in terms of downtime stoppages. This was aimed at gaining a better understanding of the contribution of the fragmentation size distributions to crusher performance.

Table 5.4 provides a comprehensive overview of the results compiled at the primary crusher over a period of a month for each blast.

Table 5.4: Performance results of the primary crusher plant recorded for each blast over a month worth of production

	Blast #1	Blast #2	Blast #3	Blast #4	Blast #5	Blast #6
Actual Shift Hours	234	280.5	200	251.54	200	199.5
Planned Shift Hours	207.5	257.5	187	245	200	199.5
Operating Hours	88.50	101.5	75.5	127.5	71	85
Tons Produced	24 965	28 549	20 921	37 283	21 062	24 965
Commitment Tons	48 672	58 344	41 600	52 320	41 496	41 496
Production Stoppages (Hours)	48.5	67	39.5	59.5	60	59.5
Planned Production Stoppages (Hours)	28	32.25	22.75	32.25	29	28.5
Idle Time Stoppages (Hours)	86.5	94.5	64.5	39.5	66	65.5
Total Production Stops (Hours)	135	161.5	104	99	125	28.5
Planned Maintenance Stoppages (Hours)	9.5	16.5	26.5	66	65	0
Production (t/h)	282	281	277	293	297	300
D01 (mm)	68.34	69.16	57.59	47	32.10	60.26
D20 (mm)	266.77	264	194.06	185.04	115.25	191.06
D50 (mm)	497.38	543.7	467.9	433.21	300	309.22
D80 (mm)	875.49	885.32	893.48	776.69	460.33	606.52

All six blasts in Table 5.4 demonstrated how production stoppages can affect operational performance. For example, blast #2 experienced the most stoppages overall (161.5 h), which had a major impact on effectiveness. The highest production rate recorded at 300 t/h was attained by blast #6 which saw the fewest stoppages (28.5 h). It should be mentioned that unplanned idle time stoppages as well as planned maintenance and production stoppages coexist. They all add to the total downtime. With this mind, blast #4 was allotted 66 h for scheduled maintenance to ensure the availability of the crushing equipment. In contrast, blast #2 recorded 94.5 h of idle time stoppages indicative of operational inefficiencies. The persistent failure to meet production targets where unplanned interruptions predominate amply illustrates the relationship between stoppages and production. Further scrutiny of stoppages is therefore necessary. To this end, Figure 5.5 provides a detailed breakdown of the crusher downtime for blast #1.

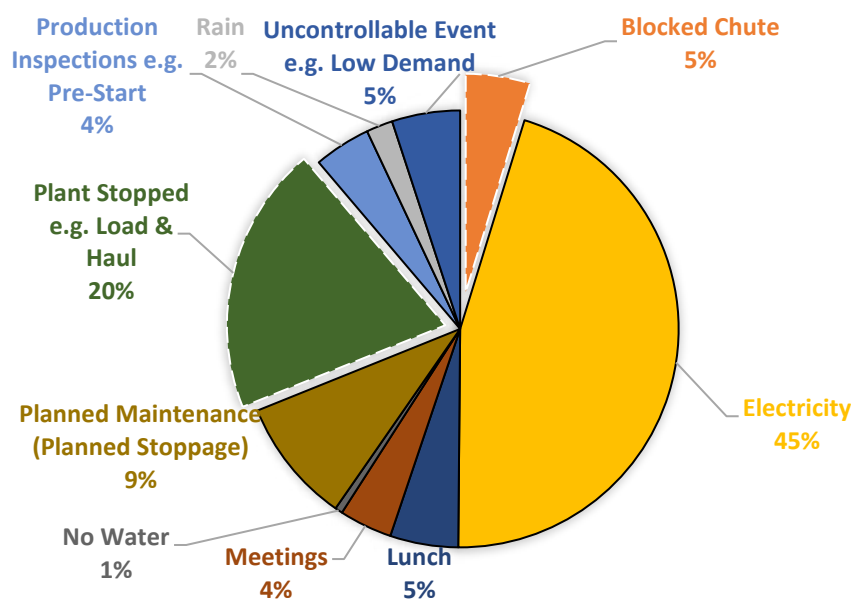


Figure 5.5: Comprehensive analysis of stoppages at the primary crusher fed with the muckpile produced from blast #1

Figure 5.5 shows that crusher downtime events are predominantly due to electricity outages, which account for the largest share at 45%. Planned maintenance contributes 9% while plant stoppages, largely attributed to

load and haul inefficiencies, represent 20% of downtime. The latter may point to potential challenges in material handling and transportation. Other disrupting factors include rain (2%), unforeseen circumstances (5%), obstructed chutes (5%), pre-start inspections (4%), water shortages (1%), meetings (4%), and lunch breaks (5%). These factors highlight key areas for improvement such as enhancing power reliability, optimizing maintenance schedules, and streamlining material handling processes to boost the overall plant productivity.

Figure 5.6 presents the analysis of stoppages associated with the ROM feed from blast #2. Like with blast #1, electricity outage is the highest contributor to downtime accounting for 53%. Second is plant stoppage due to load and haul inefficiencies (12%), a bottleneck that may also need attention. Last, production inspections, rain, and other factors collectively adds up to 25% of the downtime.

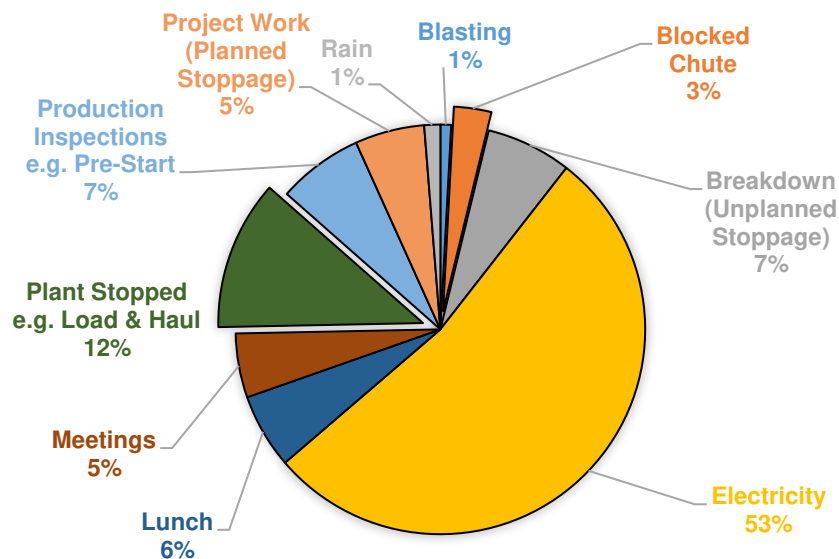


Figure 5.6: Detailed examination of stoppages at the primary crusher fed with the muckpile produced from blast #2

Ample details of the analysis of downtime for all six blasts are available in Appendix F1. However, based on the features standing out from Figure 5.5 and Figure 5.6, power outages account for at least 40% of downtime in all

blasts. And for most blasts, plant stoppages are the second largest cause of downtime hinting at loading and hauling issues at the quarry. Finally, other events, including production inspections, rain, blasting, blocked chutes, breakdowns, meetings, and lunch breaks, have limited contribution to the overall downtime picture.

5.4. Performance of the primary crusher as a function of blasting

The ability of the primary crusher to sustain continuous crushing and the consistency of the rock flow to the crusher are the two key factors driving performance. Articulated dump trucks (ADT) are used to ensure a constant supply of rock material to the crusher. However, as can be seen in Figure 5.7, the crushing performance has not reached the planned production target set at 325 metric tons per hour (t/h) for the quarry.

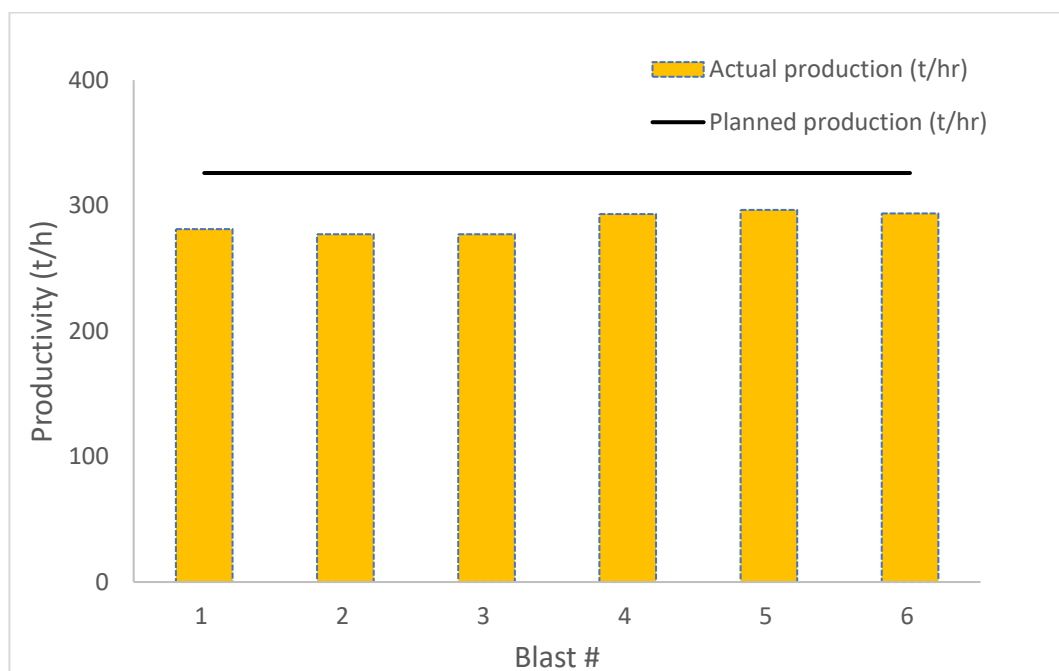


Figure 5.7: Performance of the primary crushing plant across the six blasts

By comparing planned and actual production rates (measured in tons per hour, t/h) for the six blasts, the results in Figure 5.7 also revealed that the crusher performed better for blasts #4, #5, and #6.

In terms of actual production rates, blast #2 recorded the lowest throughput at 277.10 t/h while the highest, i.e., 300 t/h, is associated with blast #6. This represents a 7.63% difference from the lowest to the highest production levels across all six blasts. Despite this improvement, none of the blasts was able to reach the planned production rate of 325 t/h. The noted shortfalls underscore the persistent operational inefficiencies alluded to in the previous Section 5.3. It is therefore posited that production rates can be achieved by reducing operational downtime, debottlenecking haul-and-load operations, and improving fragmentation quality.

5.5. Effect of rock fragmentation on crusher throughput

In this section, linear regression is used to determine the relationship between ROM mean fragmentation and crusher throughput. This is done to ascertain whether there could be a marked relationship between the two variables. The outcome of the endeavour is depicted in Figure 5.8.

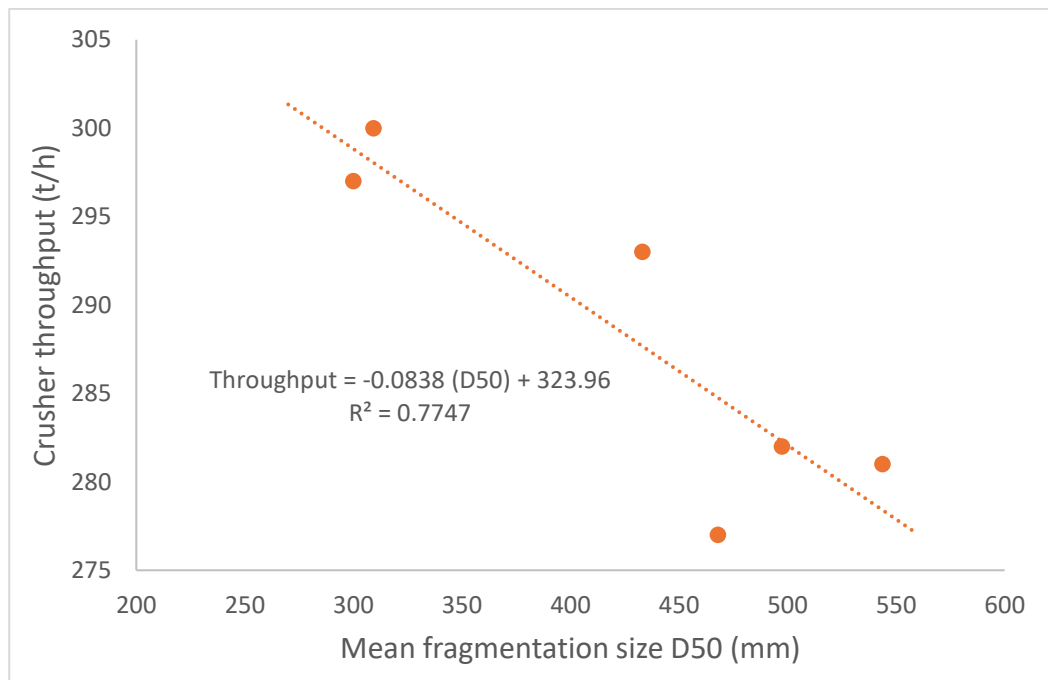


Figure 5.8: Relationship between ROM feed size and crusher throughput

The production throughput of the primary crusher is mostly proportional to the mean particle size (D50) of the ROM feed. And as can be seen in Figure

5.8, an increase in the mean size (D50) results into a decrease in throughput. This is consistent with various studies that have shown that a coarser ROM feed hinders throughput (Kazem and Bahareh, 2006; Kim, 2010; Choudhary et al., 2017; Gyamfi and Afum, 2021). The empirical correlation is also characterised by a strong correlation at $R^2 = 0.7747$. This suggests that changes in the mean fragmentation are largely responsible for variations in crusher throughput.

In another concordant study, Ozdemir (2021) assessed the relationship between blast fragmentation size and jaw crusher throughput. The researcher concluded that the mean size of the blasted rock has a great bearing on crusher throughput. And McKee et al. (1995) claimed that a 20% increase in throughput capacity can be achieved by systematically reducing fragmentation size. The current research study achieved a 7% increase reported in Figure 5.7. It is argued that when the ROM feed size is small, the crusher can treat more material in less time. As a result, the mining operation becomes more productive, efficient, and economical.

Finally, an analysis of variance (ANOVA) was carried out to examine the statistical significance of the fragmentation-throughput relationship. Table 5.5 displays some of the outputs of the ANOVA including Standard Error, R^2 , Multiple R, and Adjusted R^2 . Multiple R represents the correlation coefficient between the actual and predicted values. A strong correlation (Multiple R = 0.8802) is therefore apparent for the model in Figure 5.8. In addition, 71.47% of the data can be explained by the model as supported by the coefficient of determination R^2 .

The two important statistics are also stated in Table 5.5: the F-statistic and its associated p-value. Using the fact that p-values are less than 0.05, the model is deemed statistically significant. And with the Standard Error at 5.06, the slope and y-intercept of the model can be quoted as (-0.0838 ± 0.1254) and (323.96 ± 54.55) . Note the wide variation on the slope that requires further refinement as additional experimental blast data becomes available.

Table 5.5: Statistics associated with the regression analysis of the fragmentation-throughput correlation

<i>Regression Statistics</i>	
Multiple R	0.8801
R Square	0.7747
Adjusted R Square	0.7184
Standard Error	5.0645
Observations	6

ANOVA					
	<i>df</i>	<i>SS</i>	<i>MS</i>	<i>F</i>	<i>Significance F</i>
Regression	1	352.75	352.75	13.75465	0.02067
Residual	4	102.58	25.65		
Total	5	455.33			

	<i>Coefficients</i>	<i>Standard Error</i>	<i>t Stat</i>	<i>P-value</i>	<i>Lower 95%</i>	<i>Upper 95%</i>	<i>Lower 95.0%</i>	<i>Upper 95.0%</i>
Intercept	323.95589	9.825048351	32.9724474	5.04531E-06	296.677183	351.2346	296.6772	351.2346
Mean Fragmentation	-0.0837715	0.022587662	-3.7087264	0.020677032	-0.1464849	-0.02106	-0.14648	-0.02106

5.6. Significance of the findings

The impact of rock fragmentation on the throughput of the primary crusher was evaluated in this chapter. Results in Figure 5.8 capture the relationship between feed and throughput of the crusher. However, the coefficient of proportionality (i.e., slope of the model in Figure 5.8) should be validated against at least 10 additional points for the model to be confidently used for optimisation purposes.

Secondly, Figure 5.7 shows that the crusher performance is influenced by ROM feed size. The highest throughput rate was observed for crusher processing fragments from blast #5 while the lowest rate was recorded for blast #2. This is probably because the muckpile from blast #5 was the finest (see Table 4.15) and contained more rock material of average size within the desired range of 150 – 450 mm. This equally means that blast #1 was to yield the lowest throughput rate since it was the coarsest (see Table 4.11). However, blast #2 experienced pronounced breakage probably during loading and hauling (see Appendix F). The compounded effects of blockages caused by large fragments (>450 mm) and plant stoppages due to load and haul may have translated in the decreased throughput shown in Figure 5.7. Note here that load and haul actually accounted for 20% of plant stoppages (see Figure 5.5) while selective loading explains the differences in crusher feed and quarry fragment sizes shown in Figure 5.3. To put it another way, more time was spent handling the coarser muckpile at the quarry with negative effect on the performance of the crusher.

Thirdly, chute blockages incurred a 3% delay for the ROM feeds from blasts #3 and #4. On top of that, blast #3 recorded a 12% downtime from load and haul operations while blast #4 experience significant disruptions due to power outages in the form of electricity loadshedding. The latter resulted in elevated stoppages which in turn greatly affected throughput. In fact, the persistence of loadshedding across all blasts prompted the company to authorise overtime work to offset production losses as reflected in Table 5.4 by the increased shift hours.

Lastly, the enhanced throughput associated with blasts #5 and #6 can be ascribed to the effective flow of material through the crusher. Ideally, fragmented rocks should run more smoothly through the crusher chamber and take less time to reduce in size. At the quarry, this is particularly valid for particles between 300 mm and 400 mm. This is what blasts #5 and #6 produced the most (refer to Table 4.13, Table 4.13, Table 5.1, and Table 5.1). In the end, their corresponding throughputs were higher at approximately 300 t/h as shown in Figure 5.7.

5.7. Conclusion

The efficiency of rock fragmentation and its subsequent effect on crusher performance were presented in this chapter. Care was taken to compare the particle size distribution of the muckpile and the crusher feed. This is because size distribution from blast site to primary crusher is frequently altered by material handling and transportation procedures. Stoppages around the crusher were also recorded for a fuller picture of the value chain.

As anticipated, differences were observed between muckpile and feed size distributions. These differences are believed to be due to load and haul operations at the quarry. There is therefore a need to quantify the contribution of load and haul operations to the transition from quarry to crusher. Sampling and measurement procedures for particle size distribution should also be reviewed for increased precision.

Finally, a correlation was found between rock fragmentation, crusher throughput, and plant downtime. Indeed, distributions with particles of size preferentially below 300 mm translated into higher throughput material flow through the crusher was improved. Oversized fragments, on the other hand, caused blockages in the crusher, longer downtime, and therefore lower throughput. Lastly, load and haul delays as well as power outages were identified as the downtime elements greatly contributing to low throughput.

Chapter 6: Conclusion and recommendations

6.1. Introduction

Rock blasting is a key factor that influences the performance and efficiency of downstream crushing. From a point of view of fragmentation, the optimal muckpile should be of uniform rock size distribution. This is essential given that fragmentation size directly affects the efficiency of the crushing process. In addition, optimal fragmentation enhances the overall operational efficiency of the mine value chain.

The primary goal of this dissertation was to assess the impact of stemming and inter-hole delay on rock fragmentation and crusher throughput. Three stemming lengths and three inter-hole delay timings were tested as part of the blasting work done at the selected quarry. The associated findings and recommendations made for future research are summarised below.

6.2. Summary of the research findings

This section is devoted to reviewing the major outcomes drawn from the field data and experimental work conducted in Chapter 3. These outcomes and associated findings were presented in detail in Chapters 4 and 5. They are now summarised below.

6.2.1. Relationship between stemming length and rock fragmentation

Three blast tests were conducted at the quarry to explore how different stemming lengths affected the quality of fragmentation. From the testwork, fragments as coarse as 1 000 mm were observed for the two extreme stemming lengths, i.e., 1 m and 2 m. In contrast, the 1.5 m stemming resulted in most fragments preferentially reporting into the 300 – 400 mm size range so desired by the crushing plant. A linear relationship was also apparent between the mean fragmentation size and stemming length. In other words, longer stemming translated into increased mean fragment size

within the muckpile. However, a stemming around 1.5 m appropriately produced the correct blend of particles for the primary crusher located downstream. This emphasizes how crucial it is to choose the right stemming length that will guarantee a balance between good correct fragmentation and safe containment of explosive energy.

Speaking of safe blasting, it was also important to check that all blasts were carried out within acceptable levels of airblast and ground vibrations. This was true for shorter stemming generally expected to lead to higher noise levels and flyrock. This research study was no difference with the 1 m stemming length recording the highest levels of airblast and ground vibration at 130 dB and 9 mm/s respectively at approximately 700 m from the blast source. These values were still below the regulatory limits (135 dB of airblast and 12.7 mm/s of ground vibration); hence, all six (including the three presented in the next sub-section) blasts were considered safe. In addition to this, where flyrock was observed, it did not reach the 500 m blast radius.

To sum up, optimal stemming length is critical to enhancing blast performance. As has been demonstrated in this study, stemming can be adjusted to improve fragmentation and contain the explosive energy and flyrock while ensuring acceptable levels of airblast and ground vibrations.

6.2.2. Relationship between inter-hole delay timing and rock fragmentation

The experimental work also involved three additional blasting tests each with the following inter-hole delay timing: 6 ms, 9 ms, and 17 ms.

As mentioned in the previous section, the three blasts complied with safety regulations in terms of airblast and ground vibrations.

In terms of the effects of inter-hole delay time on blast performance, optimal delay timing was tentatively found to be located between 6 ms and 9 ms. This is because the delay timings of 6 ms and 9 ms both yielded muckpiles with a mean size around 296 mm while the 17 ms delay led to a muckpile

of mean size 495 mm. Also noted is that the first two blasts falling within the 6 – 9 ms timing window allowed blast waves to propagate simultaneously through the air and the ground better than the blast with a 17 ms delay. In addition, the investigation showed that the inter-hole delay timing of 9 ms produced the most suitable fragmentation size distribution for downstream crushing.

The above findings led to the conclusion that the accurate control of inter-hole delay timing is essential to achieving the intended fragmentation results. As such, precise modifications to timing is necessary until the suitable delay timing range is identified in line with the strategic objectives of the operation.

6.2.3. Evaluation of fragmentation models

The next step of the study was concerned with testing two most prominent fragmentation models against the blast data collected. These two models are the Kuznetsov-Rammler (Kuz-Ram) model and the Kuznetsov-Cunningham-Ouchterlony (KCO) model.

The blast data measured using the WipFrag was used as the actual fragmentation size distributions from the six blasts. Predictions of the distributions were then produced using in turn the Kuz-Ram model and the KCO model. Rock mass properties, geological settings, and blast design parameters were also considered in the estimations. Statistical analysis was also employed to compare the two fragmentation models.

In effect, the KCO models outperformed the Kuz-Ram model in four out of the six blasts. And despite the user-friendliness of the Kuz-Ram model, the KCO model showed better prediction accuracy for the mean size and the overall fragment size distribution. The prediction errors were also low. It is therefore recommended that the KCO model be adopted at the quarry for better operational planning and fragmentation prediction.

6.2.4. Relationship between rock fragmentation and downstream crusher performance

The last phase of the research study involved evaluating the relationship between fragmentation and downstream crushing. Understanding this relationship is crucial for optimising the overall productivity of the crushing process.

The study compared the particle size distribution of the muckpile and crusher feed, noting that variations in size distribution often occur during material handling and transportation. Differences between the muckpile and feed were primarily attributed to load and haul operations at the quarry, suggesting the need to better quantify their contribution to the transition from quarry to crusher. The research also calls for more precise sampling and measurement procedures for particle size distribution to improve data accuracy.

The study further explores the correlation between rock fragmentation, crusher throughput, and plant downtime. It was found that fragmentation producing particles mainly below 300 mm led to higher throughput and smoother material flow, while oversized fragments caused blockages and longer downtimes, reducing throughput. Delays in load and haul operations, as well as power outages, were identified as key contributors to downtime and low throughput. These findings highlight the critical role of fragmentation control in optimising crusher performance.

All in all, the main findings are that proper stemming lengths and inter-hole delay timings can significantly improve fragmentation. Moreover, the study demonstrated that better blast fragmentation can reduce blockages and downtime around the crusher. This in turn can translate into increased crusher throughput.

6.3. Recommendations for future work

Based on the conclusions drawn from this research, the following recommendations are proposed to enhance blasting operations and improve fragmentation outcomes:

- More blast data for refinement of models and more sites. This approach may potentially lead to enhanced model refinement, resulting in more accurate predictions of blast outcomes. The inclusion of multiple sites further strengthens the models, enabling their effective application across different mining environments.
- Investigate how stemming length affect the distribution of explosive energy within the blast hole and the rock mass so that this may be linked to rock fragmentation itself. Understanding this connection may aid in improving the design and techniques for stemming.
- Explore the connection between rock fragmentation and the energy efficiency of the crushing process. It may help minimise energy usage and maximise throughput by the crusher.
- Find a way of quantifying breakage around the loading equipment and possibly a better way of conducting image analysis. This approach will enable a more accurate assessment of fragmentation impact on loading times and equipment performance.
- It is recommended that that production rates be achieved by reducing operational downtime, debottlenecking haul-and-load operations, and improving fragmentation quality. By addressing bottlenecks in haul-and-load operations and improving fragmentation quality, operational efficiency can be increased, delays reduced, and production rates enhanced.
- Installing a camera at the crusher to capture real-time fragment data would enhance analysis of fragmentation and crusher throughput, improving performance and efficiency.

List of references

- Adebola, J.M., Ajayi, O.D., Elijah, O.P., 2016. Rock fragmentation prediction using Kuz-Ram model. *Journal of Environmental and Earth Science*, vol. 6, no. 5, pp. 110 – 115
- Adeyemi, R. A., Jafaru, B., Anikoh, G. A., & Idowu, K. A. (2019). Optimization of Blast Design for Quarries - A Case Study of ZIBO Quarry. *American Journal of Engineering Research*, vol. 8, no. 8, pp. 84 – 92
- AEL. (2014). *Surface Blasting Handbook* (1st ed.). Modderfontein: AEL mining services
- Agyei, G., Assuan, P., 2022. Predicting fragmentation distribution of rock blasting at Eshiem Pit of Aliko Resources Limited, Ghana. *Nigerian Journal of Technology (NIJOTECH)*, vol. 41, no. 4, pp. 651 – 661
- Alderliesten, M., 2013. Mean Particle Diameters. Part VII. The Rosin-Rammler size distribution: Physical and mathematical properties and relationships to moment-ratio defined mean particle diameters. *Particle and Particle Systems Characterization*, vol. 30, no. 3, pp. 244 – 257
- Alipour, A., Mokhtarian, M., Chehreghani, S., 2018. An application of fuzzy sets to the Blastability Index (BI) used in rock engineering. *Periodica Polytechnica Civil Engineering*, vol. 62, no. 3, pp. 580 – 589
- Al-Thyabat, S. and Miles, N.J., 2006. An improved estimation of size distribution from particle profile measurements. *Powder Technology*, vol. 166, no. 3, pp. 152 – 160
- Al-Thyabat, S., Miles, N.J., 2006. An improved estimation of size distribution from particle profile measurements. *Powder Technology*, vol. 166, no. 3, pp.152 – 160
- Amick, H., Gendreau, M., 2000. Construction vibrations and their impact on vibration-sensitive facilities. *Construction Congress VI: Building together for a better tomorrow in an increasingly complex world*, pp. 758 – 767

- Amiel, A., 2008. Blast fragmentation optimization at Tarkwa Gold Mine using 6 Sigma methodologies. *Journal of the Southern African Institute of Mining and Metallurgy*, vol. 108, no. 11, pp. 669 – 681
- Babaeian, M., Ataei, M., Sereshki, F., Sotoudeh, F., Mohammadi, S., 2019. A new framework for evaluation of rock fragmentation in open pit mines. *Journal of Rock Mechanics and Geotechnical Engineering*, vol. 11, no. 2, pp. 325 – 336
- Bansah, K.J., Arko-Gyimah, K., Kansake, B.A., Dumakor-Dupey, N.K., 2016. Mitigating blast vibration impact. *UMaT Biennial International Mining and Mineral Conference*, pp. 30 – 36
- Bergmann, O.R., Wu, F.C., Edl, J.W., 1974. Model rock blasting measures effect of delays and hole patterns on rock fragmentation. *International Journal of Rock Mechanics and Mining Sciences and Geomechanics Abstracts*, vol. 11, no. 11, p. A233
- Beyglou, A., Johansson, D., Schunnesson, H., 2017. Target fragmentation for efficient loading and crushing – The Aitik case. *Journal of the Southern African Institute of Mining and Metallurgy*, vol. 117, no. 11, pp. 1053 – 1062
- Bhatawdekar, R.M., Mohamad, E.T., Dan, M.F.M., Singh, T.N., Pathak, P., Armaghani, D.J., 2022. Rock mass classification for the assessment of blastability in tropically weathered igneous rocks. In *Risk, Reliability and Sustainable Remediation in the Field of Civil and Environmental Engineering Elsevier*, pp. 255 – 283
- Bleakney III, E.E., 1984. A study on fragmentation and ground vibration with air space in the blasthole. Master's dissertation, University of Missouri – Rolla, United States of America.
- BME. 2023. BME. URL: <https://bme.co.za/innovex-100/>, Information retrieved on 12 October 2024

Bosman, H.G., Bedser, G., Cunningham, C.V.B., 1997. Production blasting with electronic delay detonators at Peak Quarry. Institute of Quarrying of South Africa, South Africa

Brent, G.F., Rothery, M.D., Dare-Bryan, P.C., Hawke, S.J., Gomez, R., Humeres, I., 2013. Ultra-high intensity blasting for improved ore comminution. In Rock Fragmentation by Blasting: The 10th International Symposium on Rock Fragmentation by Blasting, Taylor and Francis Books Ltd., vol. 2012, no.10, pp. 163 – 169

Cevizci, H., 2013. A new stemming application for blasting: a case study. REM: Revista Escola de Minas, vol. 66, pp. 513 – 519

Cevizci, H., Ozkahraman, H.T., 2012. The effect of blast hole stemming length to rockpile fragmentation at limestone quarries. International Journal of Rock Mechanics and Mining Science, vol. 53, pp. 32 – 35

Cho, S.H., Kaneko, K., 2004. Rock fragmentation control in blasting. Materials Transactions, vol. 45, no. 5, pp. 1722 – 1730

Cho, S.H., Nishi, M., Yamamoto, M. and Kaneko, K., 2003. Fragment size distribution in blasting. Materials transactions, vol. 44, no. 5, pp. 951 – 956

Choudhary, B.S., Agrawal, A., Arora, R., 2021. Stemming material and Inter-row delay timing effect on blast results in limestone mines. Sādhanā, vol. 46, no. 23, pp. 1 – 12

Chung, S., Katsabanis, P.D. 2001. An integrated approach for estimation of fragmentation. Proceedings of the 27th ISEE Annual Conference on Explosives and Blasting Technique, Florida

Cunningham, C.V., 1987. Fragmentation estimations and Kuz-Ram model – Four years on. Proceedings of the Second International Symposium on Rock Fragmentation by Blasting, pp. 475 – 487

Cunningham, C.V., 2005. The Kuz-Ram fragmentation model – 20 years on. European Federation of Explosives Engineers, vol. 4, pp. 201 – 210

Delagrammatikas, G., Tsimas, S., 2004. Grinding process simulation based on Rosin-Rammler equation. *Chemical Engineering Communications*, vol. 191, no. 10, pp.1362 – 1378

Dotto, M.S., Pourrahimian, Y., 2024. The influence of explosive and rock Mass properties on blast damage in a single-hole blasting. *Mining*, vol. 4, no. 1, pp.168 – 188

Duvall, W.I. and Fogelson, D.E., 1962. Review of criteria for estimating damage to residences from blasting vibrations, US Dept. of the Interior, Bureau of Mines. Report of investigations, p. 5968

Elevli, B. and Arpaz, E., 2010. Evaluation of parameters affected on the blast induced ground vibration (BIGV) by using relation diagram method (RDM). *Acta Montanistica Slovaca*, vol. 15, no. 4, p. 261

Esen, S., 2013. Fragmentation modelling and the effects of ROM fragmentation on comminution circuits. 23rd International Mining Congress and Exhibition of Turkey, pp. 251 – 260

Esen, S., 2017, January. Evaluating the fragmentation data from copper and gold mines. In 43rd Annual Conference on Explosives and Blasting Technique, pp. 1 – 13

Fan, X., Zhang, P., Zhang, Q., Yang, B., Wang, B., Nie, W., 2016. An explosive range model based on the gas composition, temperature, and pressure during air drilling. *Mathematical Problems in Engineering*, vol. 2016, no. 1, pp.1 – 10

Gaunt, J., Symonds, D., McNamara, G., Adiyansyah, B., Kennelly, L., Sellers, E.A.J.A., Kanchibotla, S.S., 2015. Optimisation of drill and blast for mill throughput improvement at Ban Houayxai Mine. In Proceedings of the 11th International Symposium on Rock Fragmentation by Blasting, Sydney, Australia, pp. 24 – 26

Gebretsadik, A., Kumar, R., Fissaha, Y., Kide, Y., Okada, N., Ikeda, H., Mishra, A.K., Armaghani, D.J., Ohtomo, Y., Kawamura, Y., 2024.

Enhancing rock fragmentation assessment in mine blasting through machine learning algorithms: a practical approach. *Discover Applied Sciences*, vol. 6, no. 5, p. 223

Gheibie, S., Aghababaei, H., Hoseinie, S.H., Pourrahimian, Y., 2009. Modified Kuz-Ram fragmentation model and its use at the Sungun Copper Mine. *International Journal of Rock Mechanics and Mining Sciences*, vol. 46, no. 6, pp. 967 – 973

Gheibie, S., Aghababaei, H., Hoseinie, S.H., Pourrahimian, Y., 2010. Kuznetsov model's efficiency in estimation of mean fragment size at the Sungun Copper Mine. In *Proceeding of 9th International Symposium on Rock Fragmentation by Blasting*, pp. 265 – 270

Gkikizas-Lampropoulos, N., 2016. Examination of the effect of time delay on fragmentation. Master's thesis, Queen's University, Canada

Gomes-Sebastiao, G.L. and De Graaf, W.W., 2017. An investigation into the fragmentation of blasted rock at Gomes Sand. *Journal of the Southern African Institute of Mining and Metallurgy*, vol. 117, no. 4, pp. 321 – 328

Guo, H., Nguyen, H., Bui, X.N., Armaghani, D.J., 2021. A new technique to predict fly-rock in bench blasting based on an ensemble of support vector regression and GLMNET. *Engineering with Computers*, vol. 37, no. 1, pp. 421 – 435

Gyamfi, S., Afum, B.O., 2021. Rock fragmentation evaluation towards blast-to-mill concept of blast optimization in hard rock mines. *Journal of Mineral and Material Science*, vol. 2, no. 2, p. 1030

Hekmat, A., Munoz, S., Gomez, R., 2019. Prediction of rock fragmentation based on a modified Kuz-Ram model. *27th International Symposium on Mine Planning and Equipment Selection – MPES 2018*, Springer International Publishing, pp. 69 – 79

Hettinger, M.R., 2015. The effects of short delay times on rock fragmentation in bench blasts. Master's dissertation, Missouri University of Science and Technology, United States of America

Hosseini, S., Khatti, J., Taiwo, B.O., Fissaha, Y., Grover, K.S., Ikeda, H., Pushkarna, M., Berhanu, M. and Ali, M., 2023. Assessment of the ground vibration during blasting in mining projects using different computational approaches. *Scientific Reports*, vol. 13, no. 1, p.18582

Hudaverdi, T., Kuzu, C. and Fisne, A., 2012. Investigation of the blast fragmentation using the mean fragment size and fragmentation index. *International Journal of Rock Mechanics and Mining Sciences*, vol. 56, pp.136 – 145

Internal Quarry Document, 2022a. Quarry blasting report 0122, Johannesburg Quarry, South Africa

Internal Quarry Document, 2022b. Quarry Blasting report 0622, Johannesburg Quarry, South Africa

Internal Quarry Document, 2022c. Quarry blasting report 0922, Johannesburg Quarry, South Africa

Internal Quarry Document, 2023. Quarry blasting report 0223, Johannesburg Quarry, South Africa

Jhanwar, J.C., Jethwa, J.L. and Reddy, A.H., 2000. Influence of air-deck blasting on fragmentation in jointed rocks in an open-pit manganese mine. *Engineering Geology*, vol. 57, no. 1-2, pp.13 – 29

Kansake, B.A., Temeng, V.A., Afum, B.O., 2016. Comparative analysis of rock fragmentation models – A case study. 4th UMaT Biennial International Mining and Mineral Conference, pp. 1 – 11

Katsabanis, P.D., Tawadrous, A., Braun, C., Kennedy, C., 2006. Timing effects on the fragmentation of small-scale blocks of granodiorite. *International Journal for Blasting and Fragmentation*, vol. 10, no. 1 – 2, pp. 83 – 93

Khandelwal, M. and Singh, T.N., 2006. Prediction of blast induced ground vibrations and frequency in opencast mine: a neural network approach. *Journal of sound and vibration*, vol. 289, no. (4-5), pp. 711 – 725

Kim, S.J., 2010. An Experimental Investigation of the effect of blasting on the impact of breakage of rocks. Master's thesis, Queen's University, Canada

Kopp, J.W., 1987. Initiation timing influence on ground vibration and airblast. *International Journal of Surface Mining, Reclamation and Environment*, vol. 1, no. 3, pp. 167 – 172

Kulula, M.I., Nashongo, M.N., Akande, J.M., 2017. Influence of blasting parameters and density of rocks on blast performance at Tschudi Mine, Tsumeb, Namibia. *Journal of Minerals and Materials Characterization and Engineering*, vol. 5, pp. 339 – 352

Kumar, S., Choudhary, B.S., 2019. Prediction of blast-induced ground vibration by ANN, USBM and CMRI formulae for safety of the structures near surface coal mines. *Journal of Mines, Metals and Fuels*, vol. 67, no. 7, pp. 351 – 356

La Rosa, D., Caron, K., Valery, W., Diaz, R. and Mamani, H., 2015. Blast fragmentation impacts on downstream processing at Goldfields Cerro Corona.

Lam, M., Jankovic, A., Valery, W., Kanchibotla, S., 2001. Maximising SAG mill throughput at Porgera gold mine by optimising blast fragmentation. *International Conference on Autogenous and Semiautogenous Grinding Technology, SAG 2001*, Vancouver, Canada

Lawal, A.I., 2021. A new modification to the Kuz-Ram model using the fragment size predicted by image analysis. *International Journal of Rock Mechanics and Mining Sciences*, vol. 138, p. 104595

- Lilly, P.A., 1986. An empirical method of assessing rock mass blastability. Large Open Pit Mining Conference, Australasian Institute of Mining and Metallurgy, Newman, Australia, pp. 89 – 92
- Liu, K., Zhao, X., Li, X., Sha, Y., Hong, Z., Yang, J., Ma, S., 2024. Effects of delay time on crack coalescence between two boreholes. Theoretical and Applied Fracture Mechanics, vol. 129, p. 104210
- Liu, L., Katsabanis, P.D., 1997. A numerical study of the effects of accurate timing on rock fragmentation. International Journal of Rock Mechanics and Mining Sciences, vol. 34, no. 5, pp. 817 – 835
- Maerz, N.H., Palangio, T.C., Franklin, J.A., 1996. WipFrag image based granulometry system. Proceedings of the FRAGBLAST, pp. 91 – 99
- Marto, A., Hajihassani, M., Jahed Armaghani, D., Tonnizam Mohamad, E. and Makhtar, A.M., 2014. A Novel Approach for Blast-Induced Flyrock Prediction Based on Imperialist Competitive Algorithm and Artificial Neural Network. The Scientific World Journal, vol. 2014, no. 1, p. 643715
- McKee, D.J., Chitombo, G.P., Morrell, S., 1995. The relationship between fragmentation in mining and comminution circuit throughput. Minerals Engineering, vol. 8, no. 11, pp. 1265 – 1274
- MHSA. (2018). Mine Health and Safety Acts no. 29 of 1996 and regulation (14 ed., Vol. 1996). (S. Ngcobo, & S. Govender, Eds.) Tarocube Pty Ltd.
- Mohamad, E., Jahed Armaghani, D., Hasanipanah, M., Murlidhar, B.R. and Alel, M.N.A., 2016. Estimation of air-overpressure produced by blasting operation through a neuro-genetic technique. Environmental Earth Sciences, vol. 75, pp. 1 – 15
- Mpofu, M., Ngobese, S., Maphalala, B., Roberts, D., Khan, S., 2021. The influence of stemming practice on ground vibration and air blast. Journal of the Southern African Institute of Mining and Metallurgy, vol. 121, no. 1, pp. 1 – 10

Mutinda, E.K., Alunda, B.O., Maina, D.K., Kasomo, R.M., 2021. Prediction of rock fragmentation using the Kuznetsov-Cunningham-Ouchterlony model. *Journal of the Southern African Institute of Mining and Metallurgy*, vol. 121, no. 3, pp. 107 – 112

Nanda, S., Pal, B.K., 2020. Analysis of blast fragmentation using WipFrag. *International Journal of Innovative Science and Research Technology*, vol. 5, no. 6, pp. 1561 – 1566

Oates, T.E., Spiteri, W., 2021. Stemming and best practice in the mining industry: A literature review. *Journal of the Southern African Institute of Mining and Metallurgy*, vol. 121, no. 8, pp. 415 – 426

Octova, A., Putri, M., Yulhendra, D., 2022. Estimation of optimal blasting geometry using multivariate modeling to reduce boulder potential and improve mining production. *Geoscience and Remote Sensing Technology*, vol. 1, pp. 1 – 12

Omotehinse, A.O., Taiwo, B.O., 2023. A comparative analysis on the performance of modified Kuz-Ram and Kuznetsov-Cunningham-Ouchterlony models on small and large diameter drill hole blasts. *Rock Mechanics and Rock Engineering*, vol. 56, no. 6, pp. 4251 – 4269

Onederra, I. and Esen, S., 2003, September. Selection of inter-hole and inter-row timing for surface blasting—an approach based on burden relief analysis. In *Proceedings of the 2nd world conference on explosives and blasting technique*, Prague. Taylor & Francis pp. 269 – 275

Onederra, I., 2007. Empirical charts for estimation of minimum response time (T min) in free face blasting. *Mining Technology*, vol. 116, no. 1, pp. 7 – 15

Oraee, K. and Asi, B., 2006. Prediction of rock fragmentation in open pit mines, using neural network analysis. In *Fifteenth international symposium on mine planning and equipment selection (MPES 2006)*.

- Otterness, R.E., Stagg, M.S., Rholl, S.A., 1991. Correlation of shock design parameters to fragmentation. Proceedings of the 7th ISEE Conference on explosives and blasting research, Las Vegas, pp. 179 – 181
- Ouchterlony, F., 2005. The Swebrec© function: linking fragmentation by blasting and crushing. Mining Technology, vol. 114, no. 1, pp. 29 – 44
- Ouchterlony, F., Paley, N., 2013. A reanalysis of fragmentation data from the Red Dog mine – Part 2. Blasting and Fragmentation, vol. 7, no. 3, pp. 139 – 172
- Ouchterlony, F., Sanchidrián, J.A., 2019. A review of development of better prediction equations for blast fragmentation. Journal of Rock Mechanics and Geotechnical Engineering, vol. 11, pp. 1094 – 1109
- Ozdemir, K., 2021. Evaluation of blast fragmentation effects on jaw crusher throughput. Arabian Journal of Geosciences, vol. 14, no. 19, p. 2036
- Park, S., Beak, J., Kim, K. and Park, Y.J., 2021. Study on reduction effect of vibration propagation due to internal explosion using composite materials. International Journal of Concrete Structures and Materials, vol. 15, pp.1 – 20
- Phamotse, K.M. and Nhleko, A.S., 2019. Determination of optimal fragmentation curves for a surface diamond mine. Journal of the Southern African Institute of Mining and Metallurgy, vol. 119, no. 7, pp.613 – 619
- Prasad, S., Choudhary, B.S., Mishra, A.K., 2017. Effect of stemming to burden ratio and powder factor on blast induced rock fragmentation – a case study. IOP Conference Series: Materials Science and Engineering, IOP Publishing, pp. 1 – 9
- Preece, D.S., Thorne, B.J., 1996. A study of detonation timing and fragmentation using 3-D finite element techniques and a damage constitutive model. Proceedings of the Fifth International symposium on Rock Fragmentation by Blasting, Montreal, Quebec, Canada, 25 – 29 August 1996

- Rajpot, M.A., 2009, March. The effect of fragmentation specification on blasting cost. In Masters Abstracts International, vol. 49, no. 02
- Reddy, S., Tripathi, A.K., Parida, S., 2020. Influence of stemming material on performance of blasting. Palarch's Journal of Archaeology of Egypt/Egyptology, vol. 17, no. 7, pp. 9797 – 9809
- Rosales-Huamani, J.A., Perez-Alvarado, R.S., Rojas-Villanueva, U., Castillo-Sequera, J.L., 2020. Design of a predictive model of rock breakage by blasting using artificial neural networks. Symmetry, vol. 12, no. 9, p.1405
- Roy, M.P., Paswan, R.K., Sarim, Md., Kumar, S., Jha, R.R., Singh, P.K., 2016. Rock fragmentation by blasting – A review. Journal of Mines, Metals and Fuels, vol. 64, no. 9, pp. 424 – 431
- Saadatmand Hashemi, A., Katsabanis, P., 2020. The effect of stress wave interaction and delay timing on blast-induced rock damage and fragmentation. Rock mechanics and rock engineering, vol. 53, no. 5, pp. 2327 – 2346
- Salehi, E., Moghadam, M.G., Khani, J., Hajihassani, M. and Abadi, S.R., 2024. Investigation of the specific charge variations in determining the optimal methods for drilling and blasting of tunnels. Acta Montanistica Slovaca, vol. 29, no. 2, pp. 294 – 309
- Sanchidrián, J.A., Segarra, P., Ouchterlony, F., Gómez, S., 2022. The influential role of powder factor vs. delay in full-scale blasting: a perspective through the fragment size-energy fan. Rock Mechanics and Rock Engineering, vol. 55, no. 7, pp.4209 – 4236
- Sayed-Ahmed, E.Y. and Naji, K.K., 2013. Status quo and critical review of PPV safe limits for subsurface construction blasting close to low-rise buildings. Research and Applications in Structural Engineering, Mechanics and Computation, London: Taylor & Francis Group, ISBN, pp. 978 – 1000

- Sazid, M.O.H.D., 2014. Investigating the role of effective stemming in engineering blasting operations for open-pit mines, Doctoral dissertation, Ph. D Thesis, Indian Institute of Technology Bombay
- Sereshki, F., Hoseini, M., Ataei, M., 2016. Fragmentation measurement using image processing. *International Journal of Mining and Geo-Engineering*, vol. 50, no. 2, pp. 211 – 218
- Sharma, G., Haukaas, T., Hall, R.A., Priyadarshini, S., 2009. Bayesian statistics and production reliability assessments for mining operations. *International Journal of Mining, Reclamation and Environment*, vol. 23, no. 3, pp. 180 – 205
- Sharma, S.K. and Rai, P., 2015. Investigation of crushed aggregate as stemming material in bench blasting: a case study. *Geotechnical and Geological Engineering*, vol. 33, pp. 1449 – 1463
- Shehu, S.A., Yusuf, K.O., Hashim, M.H., 2020. Comparative study of WipFrag image analysis and Kuz-Ram empirical model in granite aggregate quarry and their application for blast fragmentation rating. *Geomechanics and Geoengineering*, vol. 17, no. 1, pp. 197 – 205
- Shehu, S.A., Yusuf, K.O., Hashim, M.H.M., 2022. Comparative study of WipFrag image analysis and Kuz-Ram empirical model in granite aggregate quarry and their application for blast fragmentation rating. *Geomechanics and Geoengineering*, vol. 17, no. 1, pp.197 – 205
- Shi, X., Zhang, Z., Qiu, X., Luo, Z., 2023. Experiment study of stemming length and stemming material impact on rock fragmentation and dynamic strain. *Sustainability*, vol. 15, no. 17, p. 13024
- Silva, J., Li, L., Gernand, J.M., 2018. Reliability analysis for mine blast performance based on delay type and firing time. *International Journal of Mining Science and Technology*, vol. 28, no. 2, pp.195 – 204

Silva, J., Worsey, T., Lusk, B., 2019. Practical assessment of rock damage due to blasting. *International Journal of Mining Science and Technology*, vol. 29, no. 3, pp. 379 – 385

Singh, M.M., Singh, R.B. and Gupta, R.N., 1991. Blast design to improve fragmentation in a mismatched combination of drill diameter and depth in bedded rock. *Mining Science and Technology*, vol. 12, no. 2, pp.179 – 186

Singh, P.K., Roy, M.P., Paswan, R.K., Sarim, M.D., Kumar, S., Jha, R.R., 2016. Rock fragmentation control in opencast blasting. *Journal of Rock Mechanics and Geotechnical Engineering*, vol. 8, no. 2, pp. 225 – 237

Singh, T.N., 2012. New trends in economical and safe rock blasting. *Journal of Powder Metallurgy and Mining*, vol. 1, no. 1., e104

Siskind, D.E., Strachura, V.J., Stagg, M.S. and Kopp, J.W., 1980. Structure response and damage produced by airblast from surface mining, US Department of the Interior, Bureau of Mines, vol. 8485

Soufi, A., Bahi, L., Ouadif, L., Kissai, J.E., 2018. Correlation between Rock mass rating, Q-system and Rock mass index based on field data. *MATEC Web of Conferences*, vol. 149, p. 2030

Stagg, M.S., 1987. Influence of blast delay time on rock fragmentation: One-tenth scale tests. *International Journal of Surface Mining*, vol. 1, pp. 215 – 222

Strebig, K., Reese, H.B., 1975. New concepts and techniques spark the Bureau's advanced mining systems program. *Coal Age*, vol. 80, no. 8, pp. 125 – 127

Sudhakar, J., Adhikari, G.R., Gupta, R.N., 2005. Comparison of fragmentation measurements by photographic and image analysis techniques. *Rock Mechanics and Rock Engineering*, vol. 39, no. 2, pp. 159 – 168

- Taji, M., Ataei, M., Goshtasbi, K. and Osanloo, M., 2013. ODM: a new approach for open pit mine blasting evaluation. *Journal of vibration and control*, vol. 19, no. 11, pp. 1738 – 1752
- Tang, H.L., Yang, J., Yu, Q., 2023. Experimental investigation of the effect of delay time on rock fragmentation in multi-hole bench blasting. *Applied Sciences*, vol. 13, no. 12, p. 7329
- Tavakol Elahi, A. and Hosseini, M., 2017. Analysis of blasted rocks fragmentation using digital image processing (case study: limestone quarry of Abyek Cement Company). *International Journal of Geo-Engineering*, vol. 8, no. 1, p.16
- Thornton, D.M., Kanchibotla, S.S., Esterle, J.S., 2001. A fragmentation model to estimate ROM size distribution of soft rock types. *Proceedings of the Annual Conference on Explosives and Blasting Technique*, pp. 41 – 53
- Tosun, A., Konak, G., Toprak, T., Karakus, D., Onur, A.H., 2014. Development of the Kuz-Ram model to blasting in a limestone quarry. *Archives of Mining Sciences*, vol. 59, no. 2, pp.477 – 488
- Uysal, O., Cavus, M., 2013. Effect of a pre-split plane on the frequencies of blast induced ground vibrations. *Acta Montanistica Slovaca*, vol. 18, no. 2, pp.101 – 109
- Wang, P., Ma, Y., Zhu, Y. and Zhu, J., 2020. Experimental Study of Blast-Induced Vibration Characteristics Based on the Delay-Time Errors of Detonator. *Advances in Civil Engineering*, vol 2020, no. 1, p. 8877409
- Wang, Y., Li, S., Geng, Y., Wang, G., 2023. Rock breaking mechanism and field test trials of segmented deep-hole blasting in rock roadway. In *Rock Dynamics: Progress and Prospect*, CRC Press., vol. 2, pp. 345 – 349
- Winzer, S.R., Furth, W., Ritter, A., 1979. Initiator firing times and their relationship to blasting performance. In *ARMA US Rock Mechanics/Geomechanics Symposium*, pp. ARMA-79

Wiss, J.F., 1968. Effects of blasting vibrations on buildings and people. Civil Engineering.

Woldeselassie, E.K., Xiuwen, C., Aredo, D.D., 2021. Optimization of drilling and blasting by empirical modelling specifically Kuz-Ram and modified Kuz-Ram models at Midroc Derba Limestone Quarry Site, Derba, Oromia, Ethiopia. International Journal of Mining Engineering and Mineral Processing, vol. 10, no. 1, pp. 1 – 8

Yi, C., Johansson, D., Nyberg, U., Sjöberg, J., 2013. Numerical simulation for the influence of delay time on the rock fragmentation. In Rock Fragmentation by Blasting: The 10th International Symposium on Rock Fragmentation by Blasting, vol. 2012, no. 10, pp. 213 – 220

Zhou, Z., Ma, J., Wang, J., Guan, S., Zhang, X., Yang, Y., 2024. Evolution characteristics of strain and displacement fields in double-hole short-delay blasting based on DIC. Processes, vol. 12, no. 7, p. 1291

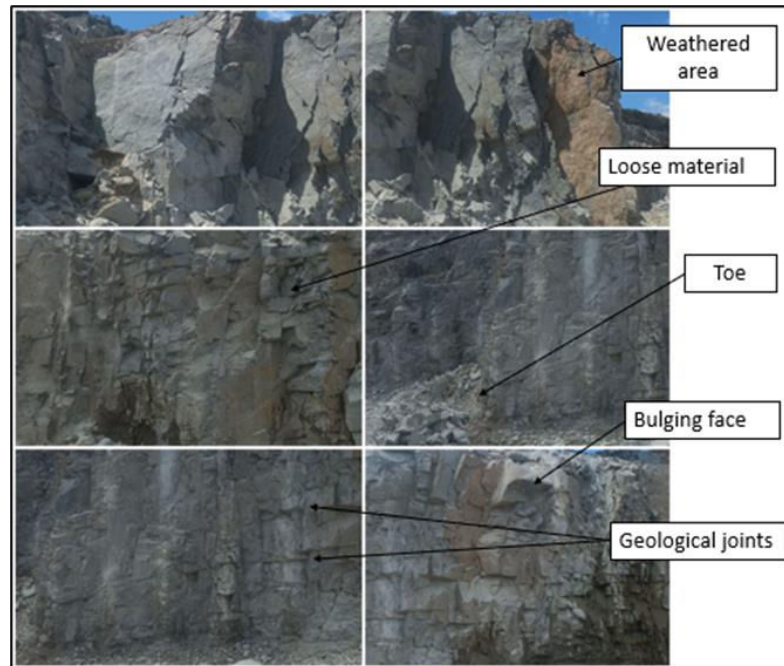
Appendices

Appendix A: Characteristics of quarry rock for various blasted bench highwall faces.

Blast #	Young's modulus E (GPa)	Rock Mass Description RMD	Joint Plane Spacing JPS	Uniaxial Compression Strength UCS (MPa)	Joint Plane Angle JPA	Joint Factor JF	Rock Density Influence RDI	Hardness Factor HF	Rock Density (kg/m ³)
1	70	50	20	235	40	60	18	47.00	2720
2	70	50	50	235	40	90	18	47.00	2720
3	70	20	20	235	40	60	18	47.00	2720
4	70	50	20	235	30	50	18	47.00	2720
5	70	20	20	235	30	50	18	47.00	2720
6	70	20	20	235	20	40	18	47.00	2720

Appendix B: Bench highwall face profiling

B1: The bench face of blast #1 displays the geological characteristics



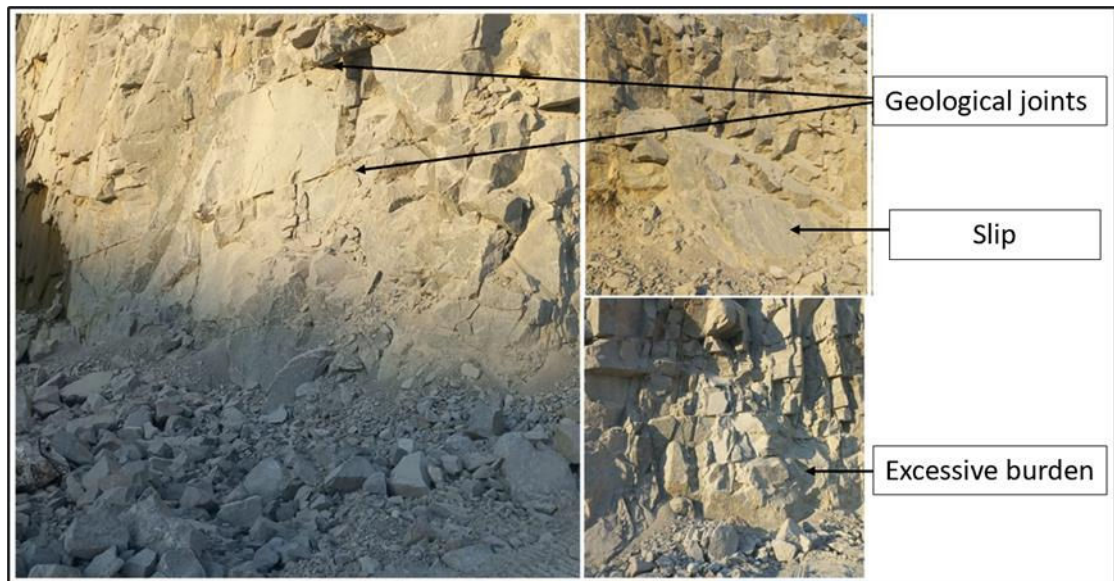
JPO = 20 – dip out of the face; JPS – 20 (>0.1 m (10 cm) -oversize); RMD = 50 (massive); JCF = 1.5 (Relaxed joints);

B2: The bench face of blast #3 displays the geological characteristics



JPO = 40 – dip into face; JPS – 20 (>0.1 m (10 cm) -oversize); RMD = 50 (massive); JCF = 1.5 (Relaxed joints)

B3: The bench face of blast #4 displays the geological characteristics



JPO = 40 – dip into face; JPS – 20 (>0.1 m (10 cm) -oversize); RMD = 50 (Massive); JCF = 1.5 (Relaxed joints)

B4: The bench face of blast #5 displays the geological characteristic



JPO = 30 – Strike normal to face; JPS – 20 (>0.1 m (10 cm) -oversize); RMD = 20 (Blocky); JCF = 1.5 (Relaxed joints)

B5: The bench face of blast #6 displays the geological characteristics



JPO = 30 – Strike normal to face; JPS – 20 (>0.1 m (10 cm) -oversize); RMD = 20 (Blocky); JCF = 1.5 (Relaxed joints)

Appendix C.

C1: Blast #1 – Gassing measurement

Total holes	65	
Total Meters	989.5	
Before gassing	221.1	
After gassing	159.4	
Final stemming/mean	2.5	
Standard deviation	0.2	
alpha	0.4	
Confidence interval	0.181	

		Sucked out
		Overcharged
		Run away
		No charge

	Top up
--	--------

A

Hole No:	1	2	3	4	5	6	7	8	9	10	11	12
Hole depth:	15.8	15.3	14.5	15.6	15.3	15.2	15.0	15.0	14.8	15.8	14.9	14.9
Before gassing	4.2	3.9	3.5	2.6	3.8	3.0	3.5	3.1	2.8	3.6	3.5	3.2
After gassing	2.8	2.2	2.7	2.9	2.6	2.2	2.9	2.6	2.4	2.2	2.7	2.1

B	Hole No:	1	2	3	4	5	6	7	8	9	10	11	12	13	14	15	16	17	18
	Hole depth:	15.1	15.3	15.2	15.1	15.6	15.5	15.5	15.7	15.4	14.9	14.8	14.9	15.0	15.0	15.2	15.5	15.5	15.5
	Before gassing	3.9	3.6	3.6	3.6	3.5	3.6	3.4	3.6	3.7	3.5	2.7	3.5	2.4	3.3	3.1	3.6	2.8	3.0
	After gassing	2.3	2.3	2.3	2.5	2.9	2.5	2.7	2.5	2.7	2.6	2.2	2.4	2.3	2.2	2.7	2.2	2.6	2.3

C	Hole No:	1	2	3	4	5	6	7	8	9	10	11	12	13	14	15	16	17
	Hole depth:	15.4	14.6	15.2	15.6	15.6	15.0	15.8	15.9	15.6	15.0	15.1	14.9	14.9	14.8	14.8	15.5	15.6
	Before gassing	3.7	3.8	3.6	3.5	3.8	3.5	3.7	2.5	2.8	3.8	3.5	2.9	3.3	3.8	3.8	2.7	1.8
	After gassing	2.4	2.2	2.2	2.7	2.7	2.9	2.6	2.6	2.7	2.7	2.2	2.3	2.6	2.5	2.2	2.3	2.8

D	Hole No:	1	2	3	4	5	6	7	8	9	10	11	12	13	14	15	16	17	18
	Hole depth:	15.6	15.9	15.2	14.9	14.7	14.9	14.9	14.7	14.4	14.8	14.8	15.6	15.5	15.8	15.8	15.9	15.1	14.9
	Before gassing	2.9	3.5	2.7	3.3	3.8	3.8	3.6	3.8	3.9	3.9	3.5	4.0	3.8	2.9	3.9	3.4	3.0	3.8
	After gassing	2.2	2.4	2.4	2.5	2.2	2.4	2.3	2.5	2.2	2.4	2.2	2.5	2.6	2.3	2.4	2.2	2.4	2.2

C2: Blast #2 – Gassing measurement

Total holes	57
Total Meters	807.2
Before gassing	189.7
After gassing	139.7

Final stemming	2.5
----------------	-----

Stdv 0.3

		Sucked out
		Overcharged
		Run away
		No charge

	Top up
--	--------

A

Hole No:	1	2	3	4	5	6	7	8	9	10	11	12	13	14
Hole depth:	14.0	13.9	16.0	15.6	15.3	15.1	13.9	13.8	14.8	14.6	14.8	15.1	15.1	15.4
Before gassing	2.7	3.2	3.0	3.4	3.5	3.1	4.1	4.3	4.4	3.2	3.5	3.8	4.5	3.7
After gassing	2.4	2.6	2.5	2.2	2.2	2.2	2.6	2.5	2.3	2.5	2.5	2.2	2.5	2.3

B

Hole No:	1	2	3	4	5	6	7	8	9	10	11	12	13	14	15
Hole depth:	13.4	13.7	13.8	14.7	15.0	14.8	13.6	14.0	14.4	13.7	15.0	15.1	15.1	15.6	15.6
Before gassing	4	3.5	3.4	3.4	3.3	3.3	3.3	3.4	3.2	3.6	3.1	3.4	3.4	3.9	3.4
After gassing	2.5	2.2	2.5	2.5	2.7	2.4	2.5	2.2	2.3	2.5	2.2	2.3	2.5	2.5	2.4

C

Hole No:	1	2	3	4	5	6	7	8	9	10	11	12	13	14	15	16
Hole depth:	14.0	13.4	13.3	13.7	13.4	13.6	13.6	13.6	13.3	11.9	13.0	13.9	14.1	15.5	12.4	12.8
Before gassing	3.0	3.2	3.4	3.2	2.4	3.4	3.2	3.4	3.2	3.3	3.4	3.5	3.3	3.2	3.5	3.5

After gassing	2.5	2.6	2.5	2.6	2.0	2.2	2.5	2.2	2.2	2.5	2.5	2.2	2.7	2.3	2.2	2.3
---------------	-----	-----	-----	-----	-----	-----	-----	-----	-----	-----	-----	-----	-----	-----	-----	-----

D

Hole No:	1	2	3	4	5	6	7	8	9	10	11	12
Hole depth:	13.5	13.4	14.0	13.3	13.4	13.6	14.0	13.2	14.0	14.6	15.2	14.6
Before gassing	3.4	4.4	3.2	3.3	3.2	3.3	3.3	3.2	3.2	3.2	3.6	3.4
After gassing	2.2	3.9	2.5	2.7	2.2	2.6	2.5	2.5	2.9	2.6	2.5	2.6

C3: Blast #3 – Gassing measurement

Total holes	48
Total Meters	715.3
Before gassing	133.5
After gassing	117.7
Final stemming	2.5

stdev 0.4

	Sucked out
	Overcharged

	Top up
--	--------

		Run away
		No charge

A

Hole No:	1	2	3	4	5	6	7
Hole depth:	15.7	15.8	15.2	15.4	16.4	15.7	15.9
Before gassing	4.2	4.3	4.2	4.4	3.5	4.0	4.0
After gassing	3.0	2.6	2.5	2.4	2.3	2.3	2.5

B

Hole No:	8	9	10	11	12	13
Hole depth:	15.9	15.7	15.7	15.7	15.9	16.1
Before gassing	3.7	4.0	3.7	4.5	4.3	3.7
After gassing	2.4	2.5	2.6	2.4	2.9	2.5

C

Hole No:	15	16	17	18	19	20	21
Hole depth:	16.2	15.7	15.2	15.5	15.3	15.4	15.5
Before gassing	3.8	3.6	4.2	4.1	1.2	3.7	4.0
After gassing	2.5	2.8	2.8	3.0	2.4	2.8	2.5

D

Hole No:	22	23	24	25	26	27
Hole depth:	16.4	15.9	15.9	15.6	15.3	15.3
Before gassing	3.1	4.0	3.7	4.0	3.6	4.4
After gassing	2.6	2.5	2.6	3.0	2.4	2.4

E

Hole No:	29	30	31	32	33
Hole depth:	15.9	15.9	15.6	15.7	15.7
Before gassing	2.6	2.9	4.0	3.9	4.0
After gassing	2.6	2.9	2.6	2.5	2.8

F

Hole No:	34	35	36
Hole depth:	15.6	13.9	14.2
Before gassing	2.6	2.9	2.9
After gassing	2.3	2.2	2.3

G

Hole No:	37	38	39	40
Hole depth:	15.4	15.3	13.4	0.0

H

Hole No:	41	42	43
Hole depth:	14.8	13.7	13.5

Before gassing	3.9	2.9	3.8	0.0
After gassing	2.4	2.2	2.3	0.0

I

Hole No:	44	45	46
Hole depth:	13.5	13.9	13.6
Before gassing	3.6	3.4	3.0
After gassing	2.3	2.3	2.2

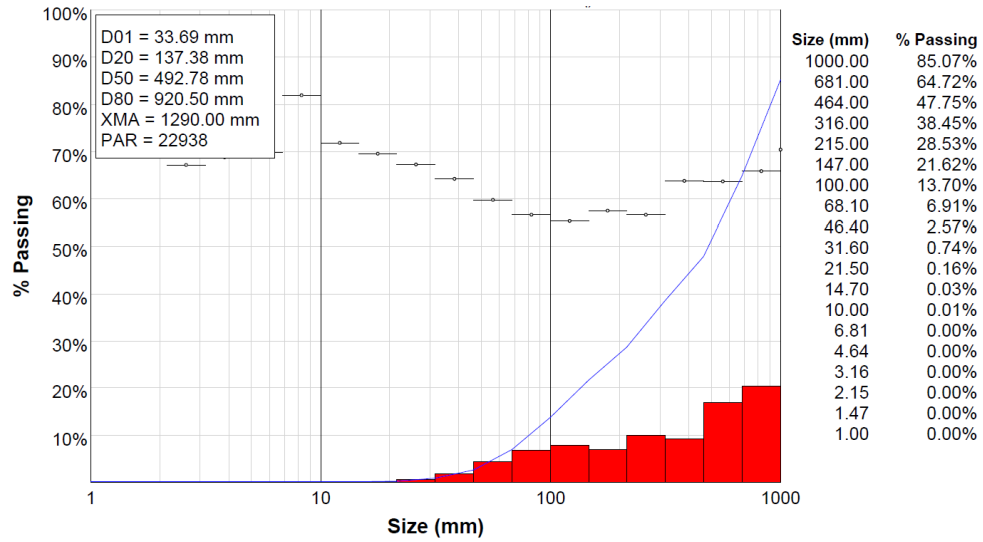
Before gassing	2.9	3.2	3.6
After gassing	2.2	2.3	2.4

J

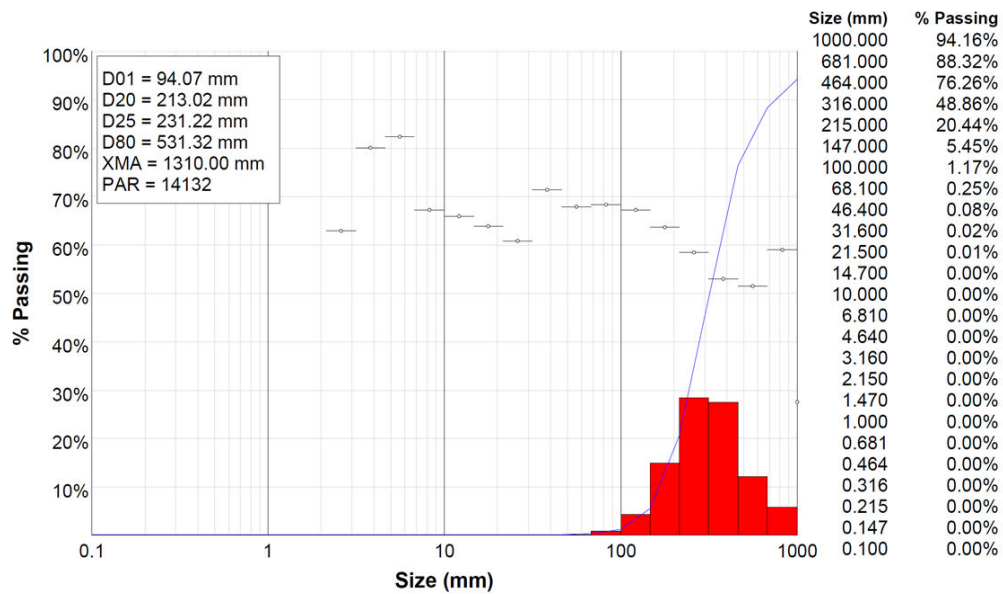
Hole No:	47	48
Hole depth:	13.9	13.7
Before gassing	3.6	3.1
After gassing	2.3	2.2

Appendix D.

D1: Blast #1 – WipFrag fragmentation results

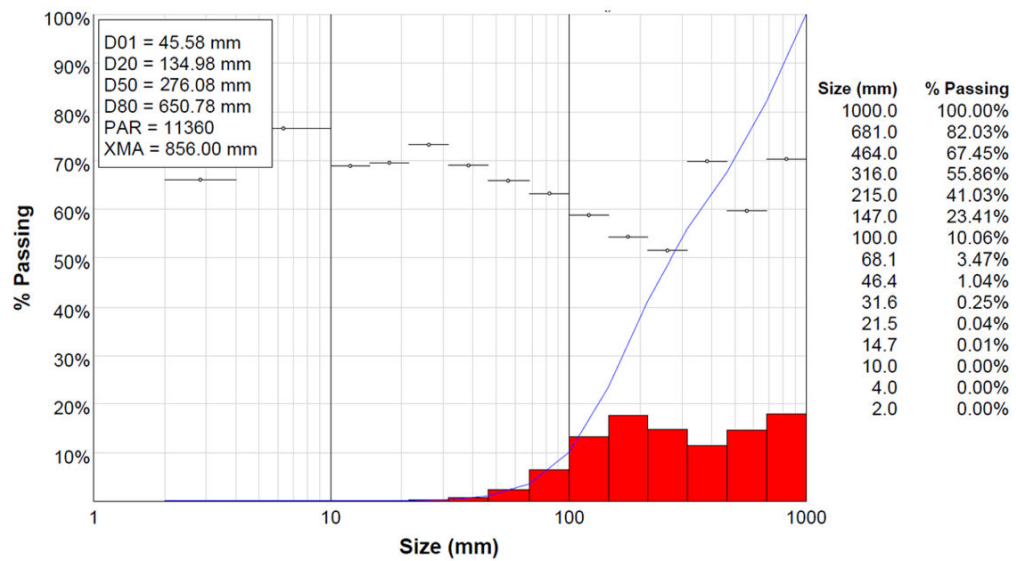


D2: Blast #2 – WipFrag fragmentation results





D3: Blast #3 – WipFrag fragmentation results and the actual muckpile

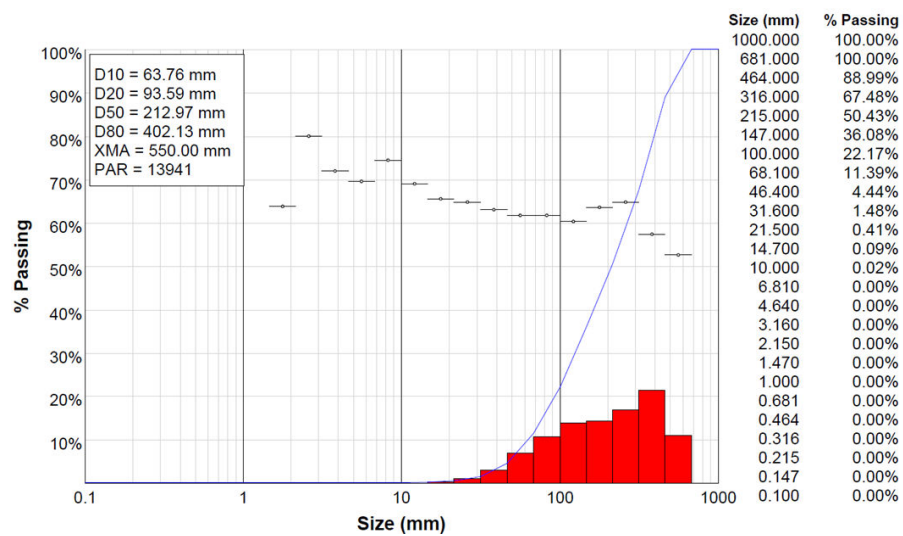


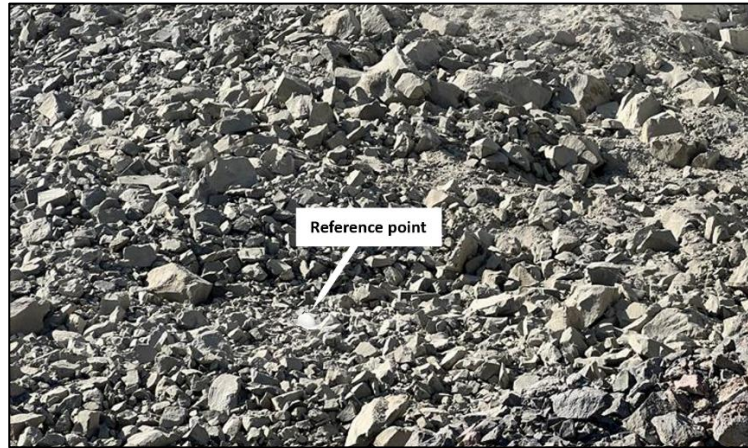


D4: Blast # 4 – Actual muckpile fragmentation

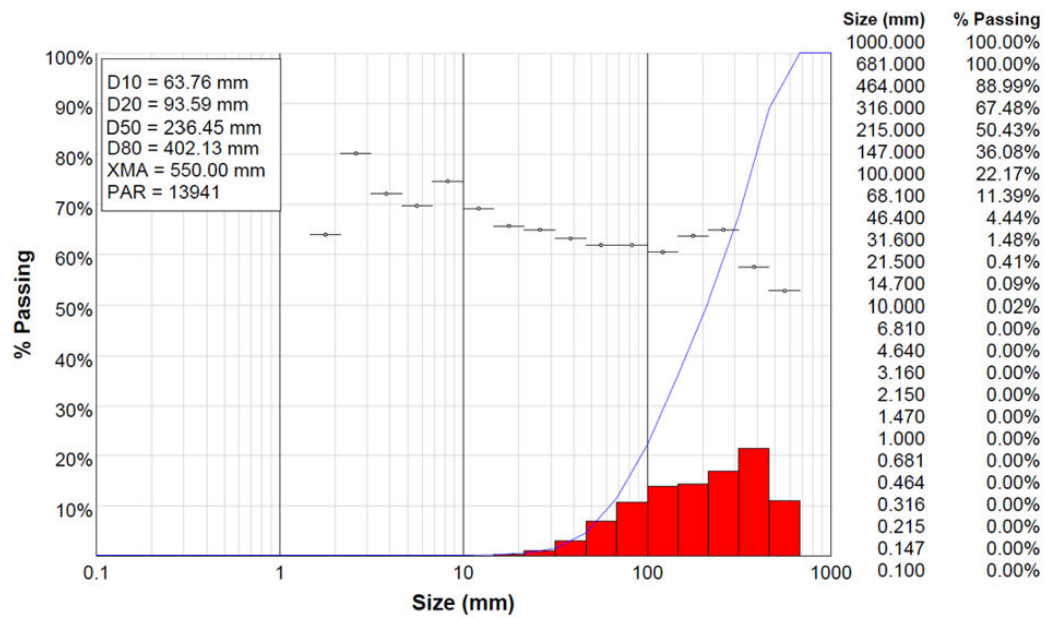


D5: Blast #5 – WipFrag fragmentation results and the actual muckpile





D6: Blast #6 – WipFrag fragmentation results



D7: Cumulative particle size distributions for blast #1, #2 and #3

Size (mm)	Blast #1	Blast #2	Blast #3
1000	85.07%	94.16%	100%
681	64.72%	88.32%	100%
464	57.75%	76.26%	89.40%
316	41.45%	48.86%	59.20%
215	29.53%	20.44%	42.81%
147	21.62%	5.45%	31.93%
100	13.70%	1.17%	22.00%
68	6.91%	0.25%	12.55%
46	2.57%	0.08%	5.64%
31	0.74%	0.02%	2.09%
21	0.16%	0.01%	0.61%
14	0.03%	0.00%	0.14%
10	0.01%	0.00%	0.00%
1	0.00%	0.00%	0.01%

D8: Blast seismograph results from primary crusher and quarry viewpoint

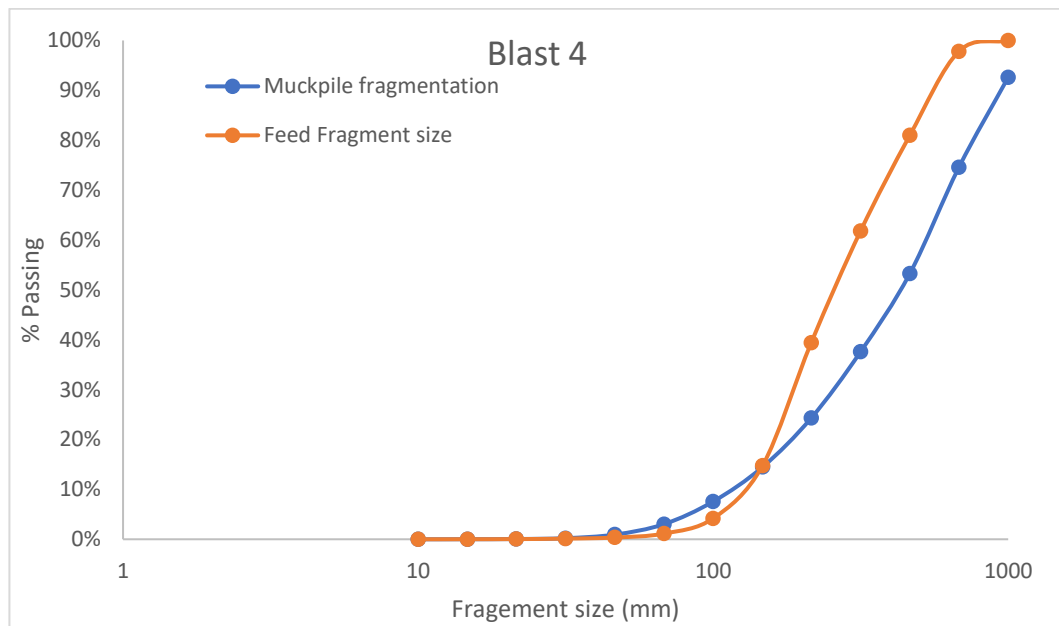
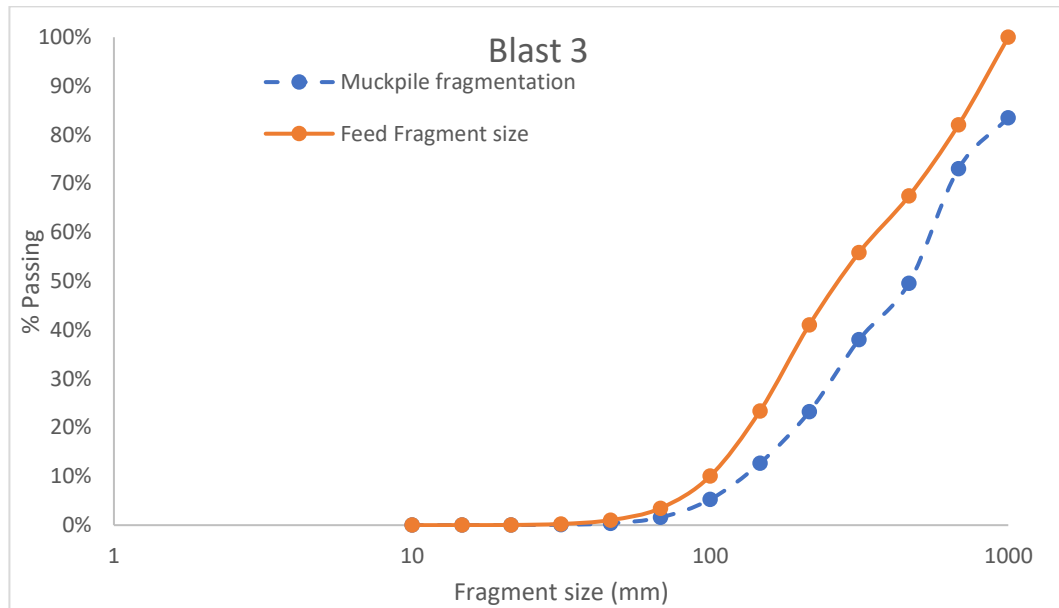
Vibrio location	Blast no.	Particles velocity (mm/s)			Frequency (Hz)		
		Radial	Transverse	Vertical	Radial	Transverse	Vertical
Primary Crusher	1	2.127	2.064	1.365	21.27	20.64	13.65
	2	3.747	2.445	2.699	37.47	24.45	26.99
	3	5.017	7.525	4.35	18.10	19.05	17.46
	4	1.810	1.905	1.746	18.10	19.05	17.46
	5	9.271	4.267	5.944	17.60	36.50	36.50
	6	1.842	1.397	1.778	18.42	13.97	17.78
Quarry viewpoint	1	6.795	6.445	3.493	67.95	64.45	34.93
	2	4.032	2.635	3.112	40.32	26.35	31.12
	3	6.538	6.892	5.098	17.80	19.80	16.95
	4	6.255	6.255	6.318	62.55	62.55	63.18
	5	2.692	2.007	1.930	23.20	36.50	21.30
	6	5.715	5.366	3.556	57.15	53.66	35.56

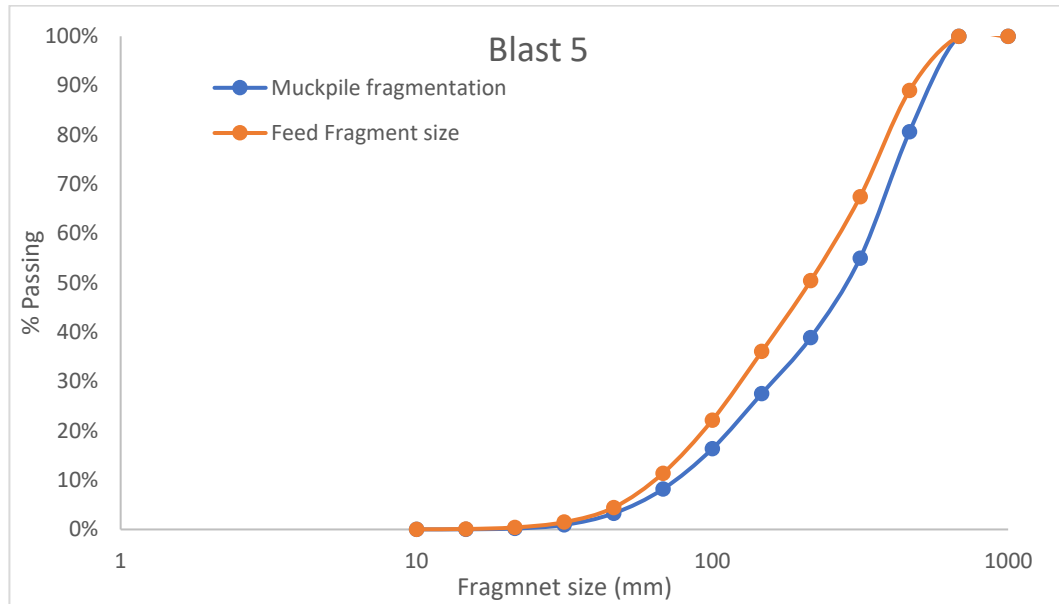
D9: Extended Kuz-Ram model distribution parameters

Inter-hole delay (T)	6.0	9.0	17.0
T_{max}	7.50	7.50	7.50
T/T_{max}	0.80	1.20	2.27
A_t	1.09	0.92	1.03
C(A)	1.00	1.00	1.00
X50 (Extended Kuz-Ram)	301.03872	296.6724	505.9208

Appendix E.

E1:



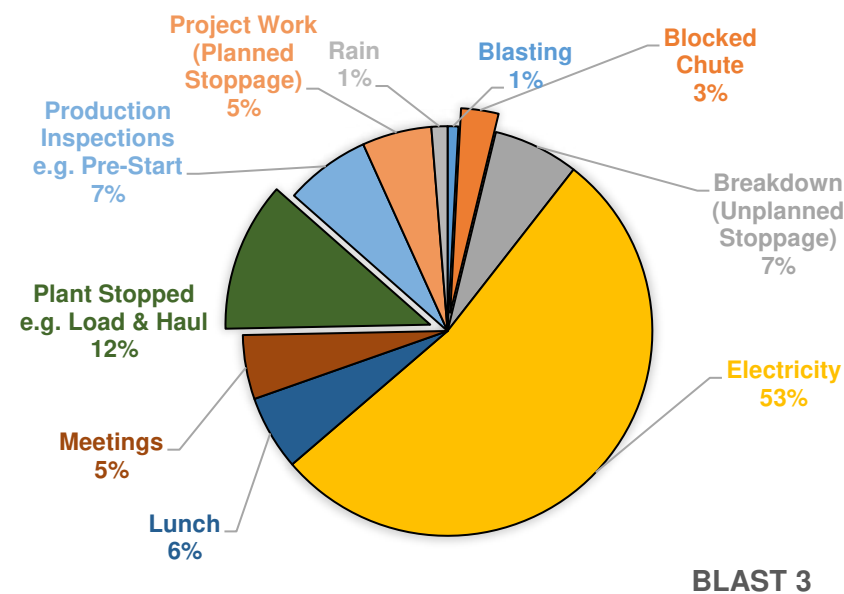
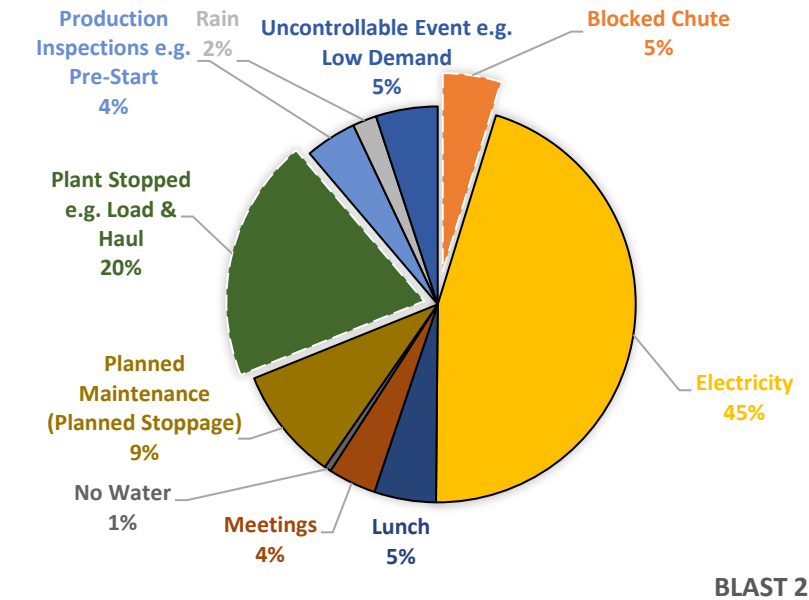


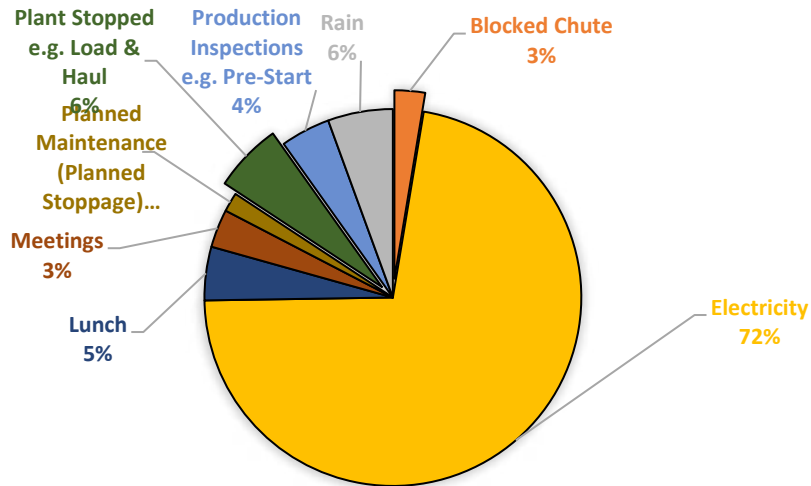
E2:

Blast	Material (%) <150 mm	Material (%) <=450 mm	Material (%) >450 mm
1	22%	47%	53%
2	6%	74%	26%
3	24%	66%	34%
4	16%	79%	21%
5	37%	87%	13%
6	20%	87%	13%

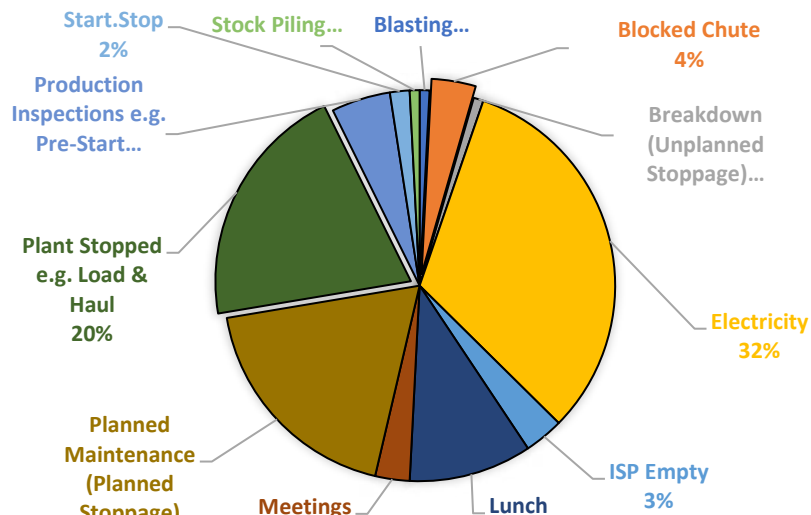
Appendix F: Primary Crusher Stoppages

F1: Detailed Overview of Stoppages at the Primary Crusher for blast feed

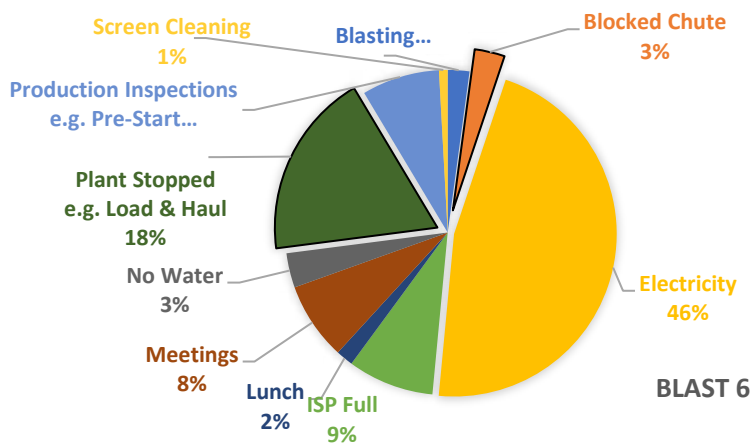




BLAST 4

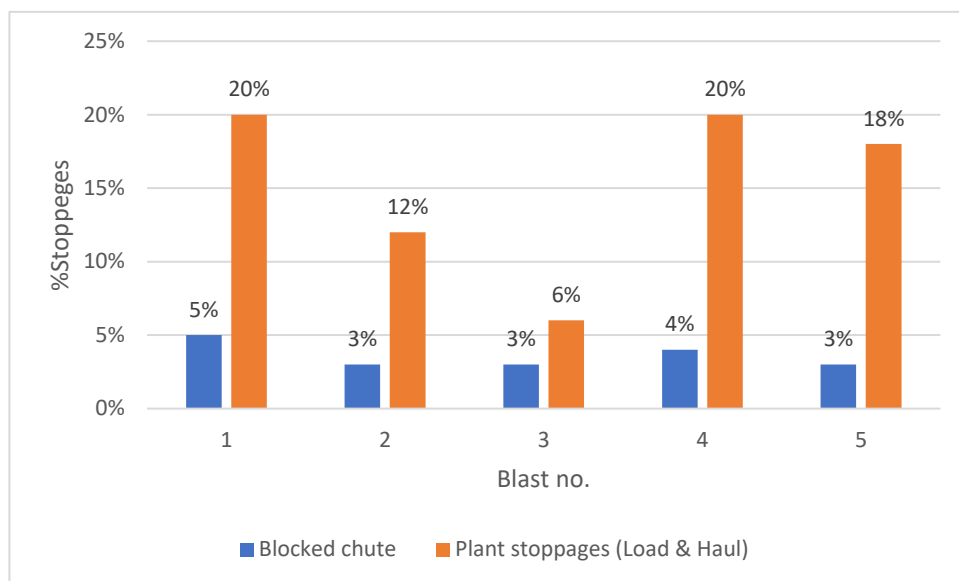


BLAST 5



BLAST 6

F2: Production stoppages – Details



Appendix G

G1: Blast #1

Size (mm)	Blast 1		
	WipFrag (%)	KRM (%)	KCO (%)
1000	85.07	96.29	97.70
681	64.72	84.54	88.80
464	47.75	65.30	69.67
316	38.45	45.10	46.19
215	28.53	28.77	27.48
147	21.62	17.58	15.97
100	13.70	10.36	9.35
68	6.91	5.99	5.66
46	2.57	3.41	3.53

	<i>WipFrag (%)</i>	<i>Kuz-Ram (%)</i>
WipFrag (%)	1	
Kuz-Ram (%)	0.990403141	1

Kuz-Ram		
(ot-et)	(ot-et)	(ot-et)^2
-11.22	11.2	126.0
-19.82	19.8	392.7
-17.55	17.5	307.8
-6.65	6.6	44.2
-0.24	0.2	0.1
4.04	4.0	16.3
3.34	3.3	11.2
0.92	0.9	0.8
-0.84	0.8	0.7

	<i>WipFrag</i>	<i>KCO</i>
WipFrag	1	
KCO	0.984624	1

KCO		
(ot-et)	(ot-et)	(ot-et)^2
-12.63	12.63	159.45
-24.08	24.08	579.76
-21.92	21.92	480.61
-7.74	7.74	59.98
1.05	1.05	1.11
5.65	5.65	31.96
4.35	4.35	18.91
1.25	1.25	1.56
-0.96	0.96	0.93

31	0.74	1.92	2.28	-1.18	1.2	1.4	-1.54	1.54	2.37
21	0.16	1.08	1.53	-0.92	0.9	0.8	-1.37	1.37	1.87
14	0.03	0.60	1.04	-0.57	0.6	0.3	-1.01	1.01	1.02
10	0.01	0.36	0.77	-0.35	0.4	0.1	-0.76	0.76	0.58
1	0.00	0.01	0.15	-0.01	0.0	0.0	-0.15	0.15	0.02
SUM				-51.03	67.63373808	902	-59.86	84	1340
n				14		n			
MAE				4.830981292		MAE			
MSE				64.46044821		MSE			
RMSE				8.028726438		RMSE			
R-Squared				0.990403141		R-Squared			

G2: Blast #2

				WipFrag (%) Kuz-Ram (%)			WipFrag KCO		
				WipFrag (%)	1		WipFrag	1	
				Kuz-Ram (%)	0.983552526	1	KCO	0.992308	1
Size (mm)	Blast 2			Modified Kuz-Ram			KCO		
	WipFrag (%)	Kuz- Ram (%)	KCO (%)	(ot-et)	(ot-et)	(ot-et)^2	(ot-et)	(ot-et)	(ot-et)^2

1000	94.16	99.19	97.18	-5.03	5.0	25.3	-3.02	3.0	9.1	
681	88.32	93.55	86.91	-5.23	5.2	27.4	1.41	1.4	2.0	
464	76.26	79.04	66.33	-2.78	2.8	7.7	9.93	9.9	98.7	
316	48.86	58.93	42.85	-10.07	10.1	101.5	6.01	6.0	36.1	
215	20.44	39.72	25.16	-19.28	19.3	371.8	-4.72	4.7	22.2	
147	5.45	25.17	14.58	-19.72	19.7	389.1	-9.13	9.1	83.4	
100	1.17	15.20	8.57	-14.03	14.0	197.0	-7.40	7.4	54.8	
68	0.25	8.95	5.22	-8.70	8.7	75.6	-4.97	5.0	24.7	
46	0.08	5.15	3.28	-5.07	5.1	25.7	-3.20	3.2	10.3	
31	0.02	2.92	2.13	-2.90	2.9	8.4	-2.11	2.1	4.5	
21	0.01	1.66	1.44	-1.65	1.7	2.7	-1.43	1.4	2.1	
14	0.00	0.92	0.99	-0.92	0.9	0.8	-0.99	1.0	1.0	
10	0.00	0.56	0.74	-0.56	0.6	0.3	-0.74	0.7	0.5	
1	0.00	0.02	0.14	-0.02	0.0	0.0	-0.14	0.1	0.0	
SUM				-95.97	96.0	1233.3	SUM	-20.52	55.2	349.4
n				14			n	14		
MAE				6.855			MAE	3.944		
MSE				88.091			MSE	24.956		
RMSE				9.386			RMSE	4.996		
R-Squared				0.984			R-Squared	0.992		

G3: Blast #3

Size (mm)	Blast 3		
	WipFra g (%)	Kuz- Ram (%)	KCO (%)
1000	100.00	99.23	98.72
681	82.03	94.47	93.27
464	67.45	82.18	79.59
316	55.86	64.18	58.72
215	41.03	45.68	38.10
147	23.41	30.60	23.28
100	10.06	19.51	13.97
68	3.47	12.10	8.52
46	1.04	7.32	5.32
31	0.25	4.37	3.42
21	0.04	2.60	2.28
14	0.01	1.51	1.54
10	0.00	0.96	1.14
1	0.00	0.04	0.21

	WipFrag (%)	Kuz-Ram (%)
WipFrag (%)	1	
Kuz-Ram (%)	0.99278061	1

Modified Kuz-Ram

(ot-et)	(ot-et)	(ot-et)^2
0.77	0.771	0.595
-12.44	12.444	154.850
-14.73	14.728	216.917
-8.32	8.320	69.218
-4.65	4.653	21.647
-7.19	7.187	51.648
-9.45	9.453	89.365
-8.63	8.628	74.448
-6.28	6.284	39.494
-4.12	4.116	16.940
-2.56	2.564	6.572
-1.50	1.504	2.263
-0.96	0.964	0.929
-0.04	0.043	0.002

SUM	-80.12	81.659	744.888
-----	--------	--------	---------

n	14
---	----

MAE	5.8328
-----	--------

	WipFrag	KCO
WipFrag	1	
g	0.99371	
KCO	4	1

KCO

(ot-et)	(ot-et)	(ot-et)^2
1.28	1.277	1.631
-11.24	11.243	126.408
-12.14	12.138	147.339
-2.86	2.863	8.197
2.93	2.932	8.594
0.13	0.126	0.016
-3.91	3.908	15.274
-5.05	5.054	25.539
-4.28	4.283	18.344
-3.17	3.170	10.050
-2.24	2.240	5.019
-1.53	1.531	2.343
-1.14	1.136	1.291
-0.21	0.207	0.043

SUM	-43.44	52.109	370.088
-----	--------	--------	---------

n	14
---	----

MAE	3.7221
-----	--------

MSE 53.2063
RMSE 7.2943

R-Squared 0.9928

MSE 26.4348
RMSE 5.1415
R-Squared 0.9937

G4: Blast #4

Size (mm)	Blast 4		
	WipFrag (%)	Kuz-Ram (%)	KCO (%)
1000	100.00	98.70	98.47
681	97.83	91.36	91.72
464	80.97	74.89	75.17
316	61.81	54.12	51.93
215	39.43	35.52	31.45
147	14.75	22.04	18.21
100	4.19	13.08	10.51
68	1.14	7.58	6.24
46	0.35	4.31	3.82

WipFrag (%)		Kuz-Ram (%)	
WipFrag (%)	1		
Kuz-Ram (%)	0.994898784	1	

Modified Kuz-Ram		
------------------	--	--

(ot-et)	(ot-et)	(ot-et)^2
1.30	1.301	1.694
6.47	6.473	41.906
6.08	6.084	37.020
7.69	7.686	59.069
3.91	3.909	15.283
-7.29	7.287	53.100
-8.89	8.888	78.990
-6.44	6.443	41.516
-3.96	3.958	15.663

WipFrag		KCO	
WipFrag	1		
KCO	0.995241	1	

KCO		
-----	--	--

(ot-et)	(ot-et)	(ot-et)^2
1.53	1.535	2.355
6.11	6.111	37.344
5.80	5.797	33.606
9.88	9.882	97.649
7.98	7.985	63.758
-3.46	3.461	11.977
-6.32	6.322	39.962
-5.10	5.103	26.037
-3.47	3.471	12.046

31	0.13	2.41	2.42		-2.28	2.285	5.221	-2.29	2.287	5.229	
21	0.04	1.36	1.59		-1.32	1.318	1.738	-1.55	1.551	2.406	
14	0.01	0.74	1.06		-0.73	0.734	0.539	-1.05	1.053	1.109	
10	0.00	0.45	0.78		-0.45	0.451	0.204	-0.78	0.778	0.605	
1	0.00	0.01	0.14		-0.01	0.015	0.000	-0.14	0.136	0.019	
				SUM	-5.93	56.833	351.942	SUM	7.15	55.470	334.102
				n	14			n	14		
				MAE	4.0595			MAE	3.9622		
				MSE	25.1387			MSE	23.8644		
				RMSE	5.0139			RMSE	4.8851		
								R-			
				R-Squared	0.9949			Squared	0.9952		

G5: Blast #5

	<i>WipFrag (%)</i>	<i>Kuz-Ram (%)</i>
WipFrag (%)	1	
Kuz-Ram (%)	0.998308474	1

	<i>WipFrag</i>	<i>KCO</i>
WipFrag	1	
KCO	0.995128	1

Size (mm)	Blast 5		
	WipFrag (%)	Kuz-Ram (%)	KCO (%)

Kuz-Ram		
(ot-et)	(ot-et)	(ot-et)^2

KCO		
(ot-et)	(ot-et)	(ot-et)^2

1000	100.00	99.75	99.23		0.25	0.248	0.061	0.77	0.770	0.593
681	100.00	96.68	95.32		3.32	3.317	11.002	4.68	4.677	21.878
464	88.99	85.56	83.93		3.43	3.431	11.774	5.06	5.064	25.643
316	67.48	66.67	63.89		0.81	0.814	0.663	3.59	3.592	12.906
215	50.43	46.36	41.85		4.07	4.073	16.592	8.58	8.580	73.612
147	36.08	29.93	25.20		6.15	6.152	37.850	10.88	10.877	118.314
100	22.17	18.26	14.69		3.91	3.914	15.322	7.48	7.482	55.986
68	11.39	10.79	8.66		0.60	0.599	0.359	2.73	2.726	7.432
46	4.44	6.22	5.23		-1.78	1.777	3.157	-0.79	0.787	0.619
31	1.48	3.52	3.25		-2.04	2.044	4.179	-1.77	1.769	3.129
21	0.41	2.00	2.10		-1.59	1.591	2.531	-1.69	1.691	2.859
14	0.09	1.11	1.38		-1.02	1.016	1.032	-1.29	1.288	1.660
10	0.03	0.67	0.99		-0.64	0.645	0.416	-0.96	0.964	0.928
1	0.00	0.02	0.16		-0.02	0.023	0.001	-0.16	0.160	0.026
SUM					15.45	29.645	104.939	SUM	37.11	50.427
n				14	n		14			
MAE				2.1175	MAE		3.6019			

MSE 7.4957
RMSE 2.7378
R-Squared 0.9983

MSE 23.2560
RMSE 4.8224
R-Squared 0.9951

G6: Blast #6

Size (mm)	Blast 6		
	WipFrag (%)	Kuz-Ram (%)	KCO (%)
1000	100.00	99.99	99.57
681	97.18	99.21	96.80
464	88.90	91.84	87.13
316	72.70	72.64	67.32
215	43.88	48.79	43.38
147	18.96	29.42	24.95
100	6.66	16.46	13.71
68	2.11	8.86	7.62
46	0.61	4.63	4.35
31	0.05	2.38	2.57
21	0.24	1.23	1.58
14	0.01	0.61	0.99

	WipFrag (%)	Kuz-Ram (%)
WipFrag (%)	1	
Kuz-Ram (%)	0.996259335	1

Kuz-Ram

(ot-et)	(ot-et)	(ot-et)^2
0.01	0.0086	0.0001
-2.03	2.0316	4.1275
-2.94	2.9441	8.6680
0.06	0.0582	0.0034
-4.91	4.9070	24.0782
-10.46	10.4582	109.3744
-9.80	9.7981	96.0019
-6.75	6.7478	45.5323
-4.02	4.0206	16.1655
-2.33	2.3293	5.4254
-0.99	0.9864	0.9729
-0.60	0.6033	0.3639

	WipFrag	KCO
WipFrag	1	
KCO	0.997662	1

KCO

(ot-et)	(ot-et)	(ot-et)^2
0.43	0.433	0.187
0.38	0.377	0.142
1.77	1.767	3.122
5.38	5.382	28.971
0.50	0.504	0.254
-5.99	5.993	35.913
-7.05	7.050	49.701
-5.51	5.510	30.361
-3.74	3.736	13.957
-2.52	2.515	6.326
-1.34	1.344	1.805
-0.98	0.984	0.968

10	0.00	0.34	0.69		-0.34	0.3447	0.1188	-0.69	0.693	0.480	
1	0.00	0.01	0.09		-0.01	0.0066	0.0000	-0.09	0.093	0.009	
				SuM	-45.11	45.2443	310.8324	SuM	-19.45	36.380	172.196
				n	14			n	14		
				MAE	3.2317			MAE	2.59856		
				MSE	22.2023			MSE	12.29972		
				RMSE	4.7119			RMSE	3.50710		
				R-Squared	0.9963			R-Squared	0.99766		